Spatial Atomic Layer Deposition of Alumina-based Thin Film Encapsulation for High Performance Perovskite Solar Cells

by

Hatameh Asgarimoghaddam

A thesis
presented to the University of Waterloo
in fulfillment of the
thesis requirement for the degree of
Doctor of Philosophy
in
Mechanical and Mechatronics Engineering (Nanotechnology)

Waterloo, Ontario, Canada, 2023

Author's Declaration

This thesis consists of material all of which I authored or co-authored: see Statement of Contributions included in the thesis. This is a true copy of the thesis, including any required final revisions, as accepted by my examiners.

I understand that my thesis may be made electronically available to the public.

Statement of Contributions

Hatameh Asgarimoghaddam was the sole author for all Chapters, which were written under the supervision of Dr. Kevin Musselman. Chapter 1-3 were not written for publication. But, I authored the manuscripts for chapter 4-7which are currently being prepared for submission to journals. I conceptualized the project, fabricated perovskite solar cells, deposited and optimized the thin film encapsulation layers, tested the devices performance and run the stability tests. Exceptions to sole authorship of material are as follows:

- Qiaoyun Chen designed and optimized perovskite solar cells fabrication process.
- Fan Ye assisted in obtaining the scanning electron micrographs of the deposited thin films.
- Saikiran Khamgaonkar fabricated and characterised PS-modified perovskite solar cells under Dr. Vivek Maheshwari's supervision.
- Dr. Kevin Mussleman supervised the design, fabrication and testing of the device and also provided editorial support and supervision.

A list of publications that I have contribute to throughout my PhD studies, but were not included in my thesis, are presented here:

- Guo, Tao, Jiawei Ge, Yixuan Jiao, Youchao Teng, Bai Sun, Wen Huang, Hatameh Asgarimoghaddam et al. "Intelligent matter endows reconfigurable temperature and humidity sensations for in-sensor computing." Materials Horizons 10, no. 3 (2023): 1030-1041.

- Mistry, Kissan, Viet Huong Nguyen, Mohamed Arabi, Khaled H. Ibrahim, Hatameh Asgarimoghaddam, Mustafa Yavuz, David Muñoz-Rojas, Eihab Abdel-Rahman, and Kevin P. Musselman. "Highly sensitive self-actuated zinc oxide resonant microcantilever humidity sensor." Nano Letters 22, no. 8 (2022): 3196-3203.

- Maas, André, Kissan Mistry, Stephan Sleziona, Abdullah H. Alshehri, Hatameh Asgarimoghaddam, Kevin Musselman, and Marika Schleberger. "Growth of p-doped 2D-MoS_2 on metal oxides from spatial atomic layer deposition." arXiv preprint arXiv:2202.06598 (2022).

- Delumeau, Louis-Vincent, Hatameh Asgarimoghaddam, Tamiru Alkie, Alexander James Bryan Jones, Samantha Lum, Kissan Mistry, Marc G. Aucoin, Stephanie DeWitte-Orr, and Kevin P. Musselman. "Effectiveness of antiviral metal and metal oxide thin-film coatings against human coronavirus 229E." APL materials 9, no. 11 (2021): 111114.

- Alshehri, Abdullah H., Jhi Yong Loke, Viet Huong Nguyen, Alexander Jones, Hatameh Asgarimoghaddam, Louis-Vincent Delumeau, Ahmed Shahin et al. "Nanoscale film thickness gradients printed in open air by spatially varying chemical vapor deposition." Advanced Functional Materials 31, no. 31 (2021): 2103271.

Abstract

Organic–inorganic hybrid perovskite solar cells (PSCs) have attracted great attention due to their high-power conversion efficiency (PCE) and low manufacturing cost. However, the long-term stability of these devices under real operational conditions remains a challenge due to the degradation of the perovskite in the presence of moisture and oxygen. In this thesis, various alumina-based thin-film encapsulation layers are deposited by atmospheric-pressure spatial atomic layer deposition (AP-SALD) to investigate their deposition rate, microstructure, and barrier properties. Moreover, the thin-film composition is optimized to maximize the PSC long-term stability in harsh environmental conditions.

Nitrogen-doped alumina (N-AlO_x) thin films are grown using an AP-SALD system at 130°C. Ammonium hydroxide (NH_4OH) is used as an oxygen precursor to incorporate nitrogen concentrations ranging from 0.08 to 0.68 atomic %. These small concentrations of nitrogen are found to have a significant impact on the structural properties of the films and their barrier performance. The N-AlO_x thin films have slightly higher growth rates, less unwanted hydroxyl and carbon content, and are smoother and more compact than undoped AlO_x. Optical calcium tests show that 60-nm-thick N-AlO_x films have lower water-vapor transmission rates (WVTR, ~10^{-5} g/m^2/day) than undoped AlO_x films and the transmission was minimized for 0.28% nitrogen. The increased compactness of the N-AlO_x films is expected to minimize nanoscale percolation pathways, whereas at higher concentrations, the nitrogen may facilitate water permeation through these pathways. The rapid nature of AP-SALD facilitates deposition of 60 nm AlO_x and N-AlO_x thin film encapsulation layers on n-type and p-type perovskite solar cells with no damage to the temperature-sensitive perovskite and organic layers. Stability tests under standard ISOS-D-1 and ISOS-D-3 conditions show significant stability enhancement for the encapsulated devices, with the 0.28% nitrogen again providing the best protection.

Zinc-doped alumina (Zn-AlO_x) thin films are then deposited by AP-SALD using a co-injection method, in which the amount of Zn can be controlled by varying the flow rate of diethylzinc (DEZ).

The Zn concentration affects the refractive index, thin-film growth rate and roughness. The optimal Zn/Al ratio is found to be 0.21, which produces films with good barrier properties and the lowest WVTR, due to decreasing the number of hydroxyl groups. However, increasing the Zn/Al ratio beyond this range decreases the effectiveness of the encapsulation layer due to an increase in the WVTR, which is attributed to the possible formation of a separate polycrystalline ZnO phase within the alumina film.

Then the effect of different oxygen precursors on the barrier properties of uniform AlO_x thin films is investigated. The films deposited using H_2O show the highest growth rate, while those deposited using H_2O_2 and O_3 show higher refractive indexes and smoother surfaces. The most effective encapsulation is provided by AlO_x deposited using O_3, due to a lower WVTR value, but H_2O_2 was also effective and moreover it is more cost-effective and has better compatibility with the perovskite layer than O_3.

Finally, an approach is presented to improve both the intrinsic and extrinsic stability of perovskite solar cells (PSCs) by fabricating polystyrene-modified perovskite thin films with an additive-engineering approach and depositing ZnO/AlO_x nanolaminate thin-film encapsulation layers by AP-SALD. WVTR tests reveal that the nanolaminate structure exhibits superior moisture-permeation-barrier characteristics ($\sim 10^{-5}$ g/m^2/day) and the polystyrene-modified PSCs shows better stability than plain PSCs. Combining the improvement in internal stability with the external encapsulation layer could result in outstanding long-term stability, even at harsh environmental conditions.

Acknowledgements

I would like to express my profound gratitude to my supervisor Dr. Kevin Musselman, granting me the opportunity to pursue my PhD studies at a university of high standing such as the University of Waterloo. His unwavering support, guidance, and encouragement throughout my PhD journey have been invaluable. His mentorship combined with his valuable insights, constructive feedback, and continuous motivation were instrumental in shaping my research and enhancing its quality and develop new perspectives. He not only helped me complete my PhD but also instilled in me a lifelong passion for research and a commitment to academic excellence.

I am also deeply grateful to the members of my thesis committee, Prof. Vivek Maheshwari, Prof. Mustafa Yavuz, Prof. John Wen, and Prof. Lukas Schmidt-Mende for their insightful comments, critical feedback, and suggestions, which helped me refine my research.

I would like to thank, my colleagues and friends for their invaluable contribution, inspiration, and encouragement. Their constructive criticism, and lively discussions made the research process more stimulating and enjoyable. Furthermore, I am thankful for the collaboration with Prof. Maheshwari and all the participants who generously gave their time and expertise to contribute to my research.

Finally, I extend my heartfelt thanks to my family who provided me with emotional support and encouragement during my academic journey. Also, a special thanks to my Husband, Siavash. His unconditional love and belief in my abilities and commitment to my success were a constant source of strength and inspiration.

Thank you all for being a part of my academic journey and for making this thesis possible.

Dedication

To my husband: Siavash

To my mother: Mansoureh

To my father: Mojtaba

To my brother: Mehran

Table of Contents

Author's Declaration ii
Statement of Contributions iii
Abstract iv
Acknowledgements vi
Dedication vii
List of Figures xi
List of Tables xvi
List of Abbreviations xvii

Chapter 1 Introduction 1
1.1 Introduction to perovskite solar cells and their instability challenges 1
1.2 Overview of the thesis 4

Chapter 2 Theory and Literature Review 6
2.1 Perovskite solar cells (PSCs) 6
2.1.1 Structure of perovskite solar cells 7
2.1.2 Working principle of perovskite solar cells 11
2.2 Instability of perovskite solar cells 12
2.2.1 Moisture and oxygen 13
2.2.2 UV light 15
2.2.3 Temperature 16
2.2.4 Stability of other layers 17
2.3 Attempts to improve stability of perovskite solar cells 19
2.3.1 Improve internal stability 19
2.3.2 Encapsulation 21
2.4 Atmospheric pressure spatial atomic layer deposition (AP-SALD) 26
2.4.1 The principles of ALD and SALD 26
2.4.2 Application of SALD for photovoltaic devices 33
2.4.3 Alumina and complex oxides thin film deposition using SALD 35

Chapter 3 Experimental and Thin Film Characterization Methods 39

3.1 AP-SALD of AlO_x thin films 39
3.2 Perovskite solar cell fabrication 42
3.2.1 n-i-p perovskite solar cells 43
3.2.2 p-i-n perovskite solar cells 44
3.3 Water vapor transmission rate (WVTR) measurements 44
3.3.1 Ca test sample preparation and WVTR calculation 46
3.4 Perovskite solar cell characterization 49
3.5 Material and thin film characterization 50

Chapter 4 Nitrogen-doped Alumina TFE layers 52
4.1 Introduction 52
4.2 Experimental 53
4.3 Results and discussions 53
4.3.1 Thin film characterization 53
4.3.2 Water vapor transmission rate measurements 61
4.3.3 PSCs characterization and stability tests 67

Chapter 5 Zn-doped Alumina TFE Layers 73
5.1 Introduction 73
5.2 Experimental 74
5.3 Results and discussions 75
5.3.1 Thin film characterization 75
5.3.2 Water vapor transmission rate measurements 85
5.3.3 Perovskite solar cells characterization and stability test 88

Chapter 6 The Effect of Different Oxidants on Alumina TFE layers 91
6.1 Introduction 91
6.2 Experimental 92
6.3 Results and discussions 93
6.3.1 Thin film characterization 93
6.3.2 Water vapor transmission rate measurements 100
Perovskite solar cells characterization and stability test 103

Chapter 7 Nanolaminate ZnO/AlO_x TFE layers 106
7.1 Introduction 106
7.2 Experimental 107
7.2.1 AP-SALD of ZnO/AlO_x nanolaminate 107
7.2.2 PS-modified perovskite solar cells fabrication 108
7.3 Results and discussions 109
7.3.1 Thin film characterization 109
7.3.2 Water vapor transmission rate measurements 111
7.3.3 Perovskite solar cells characterization and stability test 115

Chapter 8 Conclusion 118

References 124

Appendix A- Supplementary material for chapter 3; WVTR and PSCs' J-V curve 140
Appendix B- Supplementary materials for chapter 4; N-AlO_x TFE 142
Appendix C- Supplementary materials for chapter 5; Zn-AlO_x TFE 144
Appendix D- Supplementry materials for chapter 7; PS-modified PSCs' charachterizations 145

List of Figures

Figure 2-1. Cubic crystal structure of an ABX_3 perovskite with common substituents listed for the A, B, and X positions. Reproduced with permission from [29]. 7

Figure 2-2. Energy band diagram of typical a) n–i–p and b) p–i–n structured PSCs. Different structural configurations of PSCs c) n–i–p mesoscopic, d) n–i–p planar, and e) p–i–n planar PSCs. Reproduced with permission from [35]. 9

Figure 2-3. a) Schematic representation of the energy band levels of $TiO_2/CH_3NH_3PbI_3$/Spiro-OMeTAD showing the conduction and valence bands of a typical perovskite solar cell. b) The scheme of the main process in PSCs. Reproduced with permission from [5]. 11

Figure 2-4. Decomposition path way of $CH_3NH_3PbI_3$, in the presence of a water molecule. Reproduced with permission from [47]. 14

Figure 2-5. Schematic diagram illustrating the proposed mechanism leading to the formation of AgI in PSCs with Ag electrodes. Reproduced with permission from [56]. 18

Figure 2-6. A schematic diagram of a perovskite solar cells with an encapsulation layer. Reproduced with permission from [9]. 23

Figure 2-7. Schematic diagram of one cycle of atomic layer deposition (ALD) of aluminum oxide using trimethylaluminum ($Al(CH_3)_3$) and water, separated by inert gas purging steps. Reproduced with permission from [85]. 27

Figure 2-8. Schematic representation of the ALD process with the variation in time, position of the substrate (black line), and precursors (colored blocks) in a) conventional ALD and b) spatial ALD, Reproduced with permission from [19]. 30

Figure 2-9. a,b) Principle of a close-proximity SALD approach. c) Scheme of the deposition reactor head designed by Kodak. Reproduced with permission from [18]. 32

Figure 2-10. Proposed reaction coordinate diagram for H_2O, H_2O_2, and O_3 on the $Al–CH_3$* surface site. Reproduced with permission from [106]. 37

Figure 3-1. AP-SALD reactor head in use by the Functional Nanomaterials group at the University of Waterloo[117]. 39

Figure 3-2. a) Schematic of the precursor bubbler and carrier line in AP-SALD system. Reproduced with permission from [117]. b) a schematic of the reactor head used in our AP-SALD system. Aluminum precursor (red), inert nitrogen (green), and oxidant and nitrogen (blue) gas streams are shown. Reproduced with permission from [26]. 40

Figure 3-3. Schematic of a) n-i-p and b) p-i-n perovskite-solar-cell structures protected with thin film encapsulation. 43

Figure 3-4. Schematic of a) 3D-printed shadow mask used to deposit Ca in desired surface area on glass substrate, and b) optical Ca test set up. 48

Figure 4-1. O1s XPS spectra of a) AlO_x and b) 0.28N-AlO_x films. c) The fraction of the O1s XPS signal attributable to Al-O and O-H components for AlO_x and N-AlO_x films. Al2p XPS spectra of d) AlO_x and e) 0.28N-AlO_x films. f) The fraction of the Al2p signal attributable to Al-O, Al-OH, and Al-N in AlO_x and N-AlO_x films. g) N1s and h) C1s XPS spectra of AlO_x and N-AlO_x films..... 56

Figure 4-2. Uniform, pinhole-free AP-SALD films deposited on Si wafers using 120 substrate oscillations. Photographic images of a) AlO_x and b) 0.28N-AlO_x. SEM images of c) AlO_x and d) 0.28N-AlO_x. Ellipsometry thickness distribution maps (in nm) of e) AlO_x and f) 0.28N-AlO_x in 20×20 cm^2 area. 58

Figure 4-3. a) Film thickness as a function of the number of AP-SALD oscillations for different nitrogen-doping levels on silicon substrates. b) GPCs, c) refractive indices, and d) surface roughness for different nitrogen-doping levels. (Refractive indices and surface roughness were measured for 60 nm thick films deposited using AP-SALD on silicon substrates.) 60

Figure 4-4. Real pictures and high contrast black-and-white images of 1.8cm×1.8cm Ca films encapsulated with a) AlO_x, b) 0.08N-AlO_x, c) 0.28N-AlO_x, d) 0.57N-AlO_x, and e) 0.68N-AlO_x barrier films with a thickness of 60 nm after storage in ISOS-D-1(25°C-55% RH) conditions for increasing time intervals. 64

Figure 4-5. Schematic of a) pinholes and micron scale defects on AlO_x thin-film encapsulation, b) Ca corrosion and the percolation paths formed progressively with time resulting from H_2O permeating along chains of chemical defect clusters like OH-defects, c) surface diffusion of water through pore walls. 66

Figure 4-6. a) X-ray diffraction (XRD) patterns of perovskite layer, b) J–V characteristics of n-i-p structure and p-i-n structure PSCs before and after deposition of 60 nm 0.28N-AlO_x TFE. 68

Figure 4-7. Normalized PCE versus time for a) n-i-p and b) p-i-n PSCs encapsulated with different thin film encapsulation kept at ISOS-D-3 (65°C-85%RH). The PCE values were normalized to their initial PCE value. The T_{80} values of the p-i-n and n-i-p PSCs with different thin film encapsulation in c) ISOS-D-1 and d) ISOS-D-3 conditions. 70

Figure 5-1. Scheme of the simultaneously injected metal precursor in AP-SALD system. 75

Figure 5-2. O1s XPS spectra of a) Al_2O_3 and b) 0.21Zn-AlO_x films. c) The fraction of the O1s XPS signal attributable to Al-O, Al-OH and Zn-O components for Al_2O_3 and Zn-AlO_x films. d) Al2p, e) Zn2p2/3 and Zn2p½ spectra of Al_2O_3 and Zn-AlO_x films. f) Grazing incidence XR) patterns of Al_2O_3, 0.21Zn-AlO_x and 0.29Zn-AlO_x films deposited on silicon substrate using 200 oscillations. 77

Figure 5-3. SEM, AFM height sensor and peak force error images of a) Al_2O_3, b) 7Zn-AlO_x, c) 10Zn-AlO_x, d) 21Zn-AlO_x, and e) 29Zn-AlO_x deposited with AP-SALD using 85 oscillations on Si substrates. 81

Figure 5-4. a) Surface roughness, b) Film thickness as a function of the number of AP-SALD oscillations, c) Thickness measured after 200 oscillations with ellipsometry and rule of mixture, and d) Refractive index for different Zn/Al on silicon substrates. (Refractive indices and surface roughness were measured for 60 nm thick films deposited using AP-SALD on silicon substrates.) 83

Figure 5-5. High-contrast black-and-white images of 1.8cm×1.8cm Ca films encapsulated with a) Al_2O_3 and b) 0.21Zn-AlO_x TFE with a thickness of 60 nm after storage in ISOS-D-3 (65°C-85% RH) conditions for increasing time intervals. 87

Figure 5-6. a) WVTR values for the 60-nm-thick TFE layers deposited with AP-SALD at ISOS-D-3 (65°C-85% RH). b) J–V characteristics of p-i-n PSCs before and after deposition of 60 nm 21Zn-AlO_x TFE layer via AP-SALD. c) Normalized PCE versus time and d) the T_{80} values of p-i-n PSCs encapsulated with different thin film encapsulation layers kept at ISOS-D-3 (65°C-85%RH). The PCE values were normalized to their initial PCE value. 89

Figure 6-1. O1s XPS spectra of a) H_2O-AlO_x, b) H_2O_2-AlO_x, and c) O_3-AlO_x thin films. The fraction of the O1s XPS signal attributable to Al-O and O-H components is reported inside the plots. d) Al2p and e) C1s XPS spectra of AlO_x thin films. 96

Figure 6-2. SEM images of a) H_2O-AlO_x, b) H_2O_2-AlO_x, and c) O_3-AlO_x, AFM images of d) H_2O-AlO_x, e) H_2O_2-AlO_x, and f) O_3-AlO_x deposited with AP-SALD using 85 oscillations on Si substrate. 97

Figure 6-3. a) Film thickness as a function of the number of AP-SALD oscillations for different oxygen precursors on silicon substrates. Corresponding growth per cycles are listed inside the plot. b) refractive indices, and c) surface roughness for different oxygen precursors. (Refractive indices and surface roughness were measured for 60 nm thick films deposited using AP-SALD on silicon substrates.) 100

Figure 6-4. High-contrast black-and-white images of 1.8cm×1.8cm Ca films encapsulated with a) H_2O-AlO_x, b) H_2O_2-AlO_x and c) O_3-AlO_x TFE with a thickness of 60 nm after storage in ISIS-D-3 (65°C-85% RH) conditions for increasing time intervals. 101

Figure 6-5. J–V characteristics of p-i-n structure PSCs before and after deposition of 60 nm a) H_2O-AlO_x, b) H_2O_2-AlO_x and c) O_3-AlO_x TFE. d) Normalized PCE versus time and e) T_{80} values of p-i-n PSCs encapsulated with different thin film encapsulation kept at ISOS-D-3 (65°C-85%RH). 104

Figure 7-1. Scheme of a) the distribution of flows into the 21 channels of the reactor head for NL deposition, and b) fabricated ZnO/AlO_x nanolaminates with associated names. 108

Figure 7-2. a) Surface roughness, and b) refractive indices of 60-nm single-layer AlO_x and ZnO, as well as different NL configurations deposited on silicon substrates using an AP-SALD system. 110

Figure 7-3. High-contrast black-and-white images of 1.8cm×1.8cm Ca films encapsulated with a) SL-AlO_x(1×60nm), b) SL-ZnO(1×60nm), c) NL-Z/A (2×30nm), d) NL-A/Z(3×20nm) and e) NL-

A/Z(5×12nm) TFE after storage in ISOS-D-3 (65°C-85% RH) conditions for increasing time intervals. 112

Figure 7-4. Water permeation mechanism via channels formed by defects in a a) single-layer, and b) nanolaminate structure. 114

Figure 7-5. Normalized PCE versus time for a) plain PSCs, b) PS-modified PSCs and c) T_{80} values of the plain and PS-modified PSCs encapsulated with different ZnO/AlO_x NL TFE layers kept at ISOS-D-3 (65°C-85%RH) conditions..... 116

Figure A-1. The oxidized surface area as a function of time for a Ca film with TFE stored at ISOS-D-1 condition. The slope of the plot corresponds to the oxidization rate of the Ca ($\Delta A/\Delta t$) needed to calculate WVTR value. A sample WVTR calculation is also provided. 140

Figure A-2. J–V characteristics of n-i-p structure and p-i-n structure perovskite solar cells. 140

Figure B-1. O1s XPS spectra of a) 0.08N-AlO_x, b) 0.57N-AlO_x, and c) 0.68N-AlO_x thin films. Al2p XPS spectra of d) 0.08N-AlO_x, e) 0.57N-AlO_x, and f) 0.68N-AlO_x thin films. 142

Figure B-2. Photographic images of a) 0.08N-AlO_x, b)0.57N-AlO_x, and c) 0.68N-AlO_x. SEM images of d) 0.08N-AlO_x, e) 0.57N-AlO_x, and f) 0.68N-AlO_x films deposited using 120 oscillations..... 142

Figure B-3. Normalized PCE versus time for a) p-i-n structure and b) n-i-p structure perovskite solar cells encapsulated with different thin film encapsulation layers kept at ISOS-D-1 (25°C-55%RH). The PCE values were normalized to their initial PCE value. 143

Figure C-1. O1s XPS spectra of a) 0.07Zn-AlO_x, b) 0.10Zn-AlO_x, and c) 0.29Zn-AlO_x thin films. . 144

Figure D-1. a) J–V characteristics of plain and PS-modified perovskite solar cells, b) XRD pattern of PS-$MAPbI_3$ and plain $MAPbI_3$ devices, SEM images of c) plain $MAPbI_3$ and d) PS-$MAPbI_3$. 146

List of Tables

Table 2.1. Specifications and requirements for encapsulating materials for the protection of perovskite solar cells from oxygen and moisture[65]. 22

Table 2.2. Summary of representative PSCs encapsulated with different materials and methods and their stabilities at different test conditions. 25

Table 2.3. Advantages and disadvantages of ALD, Reproduced with permission from [87]. 28

Table 2.4.Selected reports on the deposition of ZnO by AP-SALD. 34

Table 2.5. Selected reports on other binary metal-oxide films deposited by AP-SALD. 35

Table 2.6. Selected reports on the deposition of Al_2O_3 by AP-SALD. 35

Table 4.1.Deposition conditions and compositions of AlO_x and N-AlO_x thin films, as determined by XPS. 54

Table 4.2. WVTR values for the 60-nm-thick TFE deposited with AP-SALD at ISOS-D-1 (25°C-55% RH) and ISOS-D-3 (65°C-85% RH). 64

Table 5.1. compositions of Al_2O_3 and Zn-AlO_x thin films, as determined by x-ray photoelectron spectroscopy. 76

Table 6.1. Deposition conditions, compositions, and overall reaction energy of AP-SCVD Al_2O_3 thin films deposited using different oxidants, as determined by x-ray photoelectron spectroscopy. 94

Table 6.2. Contribution of surface hydroxyl groups and nitrogen energy well in decreasing WVTR. 103

Table 7.1. a) WVTR values and b) time to complete oxidation of the Ca layer for the 60-nm-thick single-layer and nanolaminate TFE deposited using the AP-SALD system and stored at ISOS-D-3 (65°C-85% RH). 113

Table A-1. PCEs of p-i-n and n-i-p perovskite solar cells measured under the global AM1.5 spectrum (1000 W/m^2) in air. 141

List of Abbreviations

a-Si	Amorphous Silicon
AFM	Atomic Force Microscopy
ALD	Atomic Layer Deposition
AP-CVD	Atmospheric-pressure Chemical vapor Deposition
AP-SALD	Atmospheric-Pressure Spatial Atomic Layer Deposition
AP-SCVD	Atmospheric-pressure Spatial Chemical vapor Deposition
CdTe	Cadmium Telluride
CIGS	Copper Indium Gallium Selenite
Co-TFSI	tris(2-(1H-pyrazol-1-yl)-4-tert butylpyridine)cobalt(III) tri[bis(trifluoromethane)sulfonimide]
CVD	Chemical Vapour Deposition
DEZ	Diethyl Zinc
DEZ	Diethylzinc
DMF	Dimethylformamide
DMSO	Dimethyl sulfoxide
DSSC	Dye-sensitized solar cell
EDS	Energy-Dispersive X-ray Spectroscopy
ETL	Electron-Transporting Layer
FA	Formamidinium
$FAPbI_3$	Formamidinium lead-iodide
FF	Fill Factor
FTO	Fluorine doped Tin Oxide
GIXRD	Grazing Incidence X-ray Diffraction
GPC	Growth Per Cycle
HTL	Hole-Transporting Layer
ISOS	International Summit on Organic Photovoltaic Stability
ITO	Indium doped Tin Oxide
J-V	Current density -Voltage
J_{ph}	Photo-generated current density
J_{SC}	Short circuit current

Li-TFSI	Bis(Trifluoromethane)sulfonimide lithium salt
MA	Methyl Ammonium
N-AlO_x	Nitrogen-doped Alumina
NL	Nanolaminate
OTR	Oxygen Transmission Rate
PCE	Power Conversion Efficiency
PECVD	Plasma Enhanced Chemical Vapor Deposition
PL	Photoluminescence
PS	Polystyrene
PSC	Perovskite solar cell
PV	Photovoltaic devices
PVB	Poly vinyl butyral
PVD	Physical Vapour Deposition
RH	Relative humidity
RMS	Root-mean square
SEM	Scanning Electron Microscopy
SL	Single layer
TCM	Transparent Conductive Materials
TCO	Transparent Conducting Substrate
TFE	Thin-Film Encapsulation
TFEL	Thin-Film Electroluminescent
TMA	Trimethyl Aluminium
TRPL	Time-Resolved Photoluminescence
UV	Ultraviolet
VBE	Valence Band Energy
V_{OC}	Open circuit voltage
WVTR	Water Vapour Transmission Rate
WVTR	Water vapor transmission rate
XPS	X-ray Photoelectron Spectroscopy
XRD	X-Ray Diffraction
Zn-AlO_x	Zinc-doped Alumina

Chapter 1
Introduction

1.1 Introduction to perovskite solar cells and their instability challenges

Organic–inorganic hybrid perovskite solar cells (PSCs) have attracted great attention in the field due to their high power conversion efficiency (PCE) and low manufacturing cost[1], which resulted in achieving a certified PCE of 25.7% in 2022[2]. Although PSCs have already achieved comparable performance to Si-based solar cells, the long-term stability of these devices under real operational conditions remains a challenge[3][4]. Both the external environment and intrinsic factors are known to contribute to PSC degradation[5], such that a combination of intrinsic stabilization and protection from the environment will be necessary to produce stable PSCs[6]. Among all the external factors affecting the durability of PSCs, moisture is the most challenging one to mitigate and plays an important role in the degradation process[7]. Water can act as a catalyst for the decomposition reaction of perovskite material which irreversibly depresses PSCs' figures of merit[8]. It was established that the most promising technique to enhance the stability of a PSC is full encapsulation of the device, which will be necessary for commercialization [9]. The encapsulation can act as a barrier, restricting the diffusion of moisture and protecting the perovskite active layer from deterioration[10]. It can also prevent the diffusion of perovskite decomposition products, which significantly inhibits the overall decomposition of the perovskite and endows the device with excellent stability[8].

Thin-film encapsulation (TFE) is one of the most promising candidates for the encapsulation of PSCs. Single-layer thin films are attractive because of the simplicity of the manufacturing process compared to multilayer encapsulation methods that require multiple processing steps[11]. Thin films can be applied as dense, pinhole-free barriers against moisture and oxygen yet remain lightweight and thin enough to not adversely affect the mechanical flexibility of the solar stack. Therefore, they can be

compatible with roll-to-roll processing[12]. Furthermore, thin films can be deposited directly onto the PSC, as in TFE, or can be used in conjunction with glass-to-glass and polymer encapsulation[6].

To fabricate the TFE, different kinds of deposition processes have been adopted including plasma-enhanced chemical vapor deposition, sputtering, and atomic layer deposition (ALD)[13]. Unfortunately, such methods require a high energy input or temperature, which might severely degrade the perovskite material[12]. The challenge lies in the fact that the barrier properties of inorganic TFE layers are greatly influenced by the deposition temperature[14]. For example, decreasing the ALD process temperature reduced the barrier performance of an AlO_x TFE, since the films had lower densities and a large amount of carbon-related impurities and hydroxyl groups[15]. Hence there is commonly a trade-off between achieving good TFE barrier properties and damaging the perovskite material. Moreover, these vacuum deposition processes are expensive and have limited throughput[13]. Therefore, it is crucial to develop scalable TFE methods that can maximize the barrier performance while minimizing damage to the perovskite during the encapsulation process[16].

In this respect, atmospheric-pressure spatial atomic layer deposition (AP-SALD) is very promising. AP-SALD is an emerging method for rapid, open-air deposition of thin films[17][18]. In contrast to conventional ALD, spatial ALD processes separate the precursors in space rather than in time. In AP-SALD, precursors flow towards the substrate in different physical locations with the substrate moving back and forth. Films are grown by alternatively exposing the substrate to the precursors, which are separated by inert gas regions[19]. AP-SALD can be up to two orders of magnitude faster than conventional ALD and its open-air nature makes it cheaper and easier to scale up[20]. These characteristics make AP-SALD very attractive for the deposition of TFE layers at a temperature that is high enough to provide good barrier properties and at a speed that is fast enough to avoid perovskite damage. Initial demonstrations of AP-SALD on top of metal-halide perovskite materials have included the deposition of a ZnO charge-injection layer on $CH_3NH_3PbBr_3$ in a perovskite

LED [21] and TiO_2 and SnO_2 electron-transport layers on the perovskite of a PSC[22][23]. However, little work has been done to produce TFE layers for PSCs using AP-SALD.

Aluminum oxide (Al_2O_3) is an attractive moisture barrier owing to its combination of adhesion, mechanical strength, chemical inertness, and ultralow water-vapor transmission rates (WVTR) on the order of 10^{-4} to 10^{-6} g per day per m^2 [11]. It has been previously established that an ultrathin ALD Al_2O_3 film deposited between perovskite and spiro-OMeTAD layers can isolate the perovskite layer from moisture, thus enhancing the stability of PSCs[24]. However, conventional ALD has not been useful for preparing effective Al_2O_3 encapsulation layers for PSCs due to the conflicting requirements of a low substrate temperature (<150°C) to prevent thermal damage to the perovskite and a higher temperature to provide a sufficient amount of thermal energy for the surface reactions to complete[15]. For example, when depositing Al_2O_3 by ALD, it has been shown that decreasing the process temperature impedes the reaction between the trimethyl aluminum (TMA) and water (H_2O), generating unreacted residues that create defects in the films, making them more permeable to water vapor[25]. Recent work from our group attempted to overcome these conflicting requirements by using an AP-SALD system to rapidly deposit Al_2O_3 thin films on partial PSC stacks[26]. However, Al_2O_3 TFE layers deposited by AP-SALD have yet to be characterized in detail and incorporated into PSC device studies. Furthermore, the composition of AP-SALD Al_2O_3 TFE layers and the introduction of more complex materials like multicomponent oxides, doped oxides, and laminate structures has yet to be studied and optimized. Despite the great potential of these materials, there is a need for further optimization and characterization to fully understand their potential and to overcome challenges in their deposition with AP-SALD.

1.2 Overview of the thesis

This manuscript will outline my work on the deposition and optimization of complex materials, such as multicomponent oxides, as high-performance thin-film-encapsulation layers in organic-inorganic perovskite solar cells using our group's novel AP-SALD system. The goal here is to incorporate dense and uniform metal-oxide encapsulation layers into a perovskite solar cell to improve device stability and reliability under harsh environmental conditions, which is the main obstacle for PSCs to be commercially viable. The quick growth rates, as well as the low deposition temperature of AP-SALD avoid degradation of the perovskite absorber layer during the SALD process, even when a thermally sensitive material like Spiro-OMeTAD was used as a hole transport layer (HTL).

Three different categories of alumina-based thin-film-encapsulation layers are explored, including doping alumina with an anion (nitrogen) and cation (zinc), replacing water with more reactive oxidants such as hydrogen peroxide and ozone, and depositing alumina/zinc oxide nanolaminate structures.

Chapter 2 provides a review of previous work on perovskite solar cells, as well as the AP-SALD technique used in this thesis. Chapter 3 outlines the experimental techniques used to deposit AP-SALD thin films and fabricate perovskite solar cells. Furthermore, it provides details on the water-vapor- transmission-rate measurements and PSC-stability-test conditions.

One of the objectives of this thesis is the characterization and optimization of metal oxynitrides, because improvements in a number of film properties have been gained by replacing aluminium oxide with aluminium oxynitride. Chapter 4 focuses on the deposition of nitrogen-doped AlO_x (N-AlO_x) films using AP-SALD. The N-AlO_x films are characterized then utilized as encapsulation layers for both p-i-n and n-i-p perovskite solar cells. The N-AlO_x composition is adjusted to enhance the stability of the

perovskite solar cells under standardized testing conditions. AP-SALD N-AlO_x thin films provide a new encapsulation route to extend the lifetime of PSCs under harsh environmental conditions.

Another objective is to investigate the effect of cation doping on the barrier properties on alumina-based thin film encapsulation. In this regard, in Chapter 5, zinc-doped alumina is deposited by AP-SALD. The Zn content of the deposited films is optimized by adjusting the deposition parameters to minimize the WVTR value and maximize the long-term stability of PSCs by improving the gas diffusion barrier properties of the TFE. The Zn-AlO_x thin films show an outstanding barrier property at an accelerated testing condition of 65°C and 85% relative humidity, because introducing Zn into the amorphous Al_2O_3 thin films increases the film density.

In Chapter 6, the deposition rate, microstructure and barrier properties of Al_2O_3 thin films deposited by AP-SALD using H_2O, hydrogen peroxide(H_2O_2) and Ozone(O_3) as oxidants are investigated. The AP-SALD process conditions using highly reactive oxidants are optimized to prevent degradation of the perovskite layer and maximize the PSC stability by providing good quality TFE.

Chapter 7 focuses on developing a better moisture-barrier film using nanolaminate films comprised of alternating layers of Al_2O_3 and zinc oxide (ZnO) deposited by AP-SALD. The effects of the number of stacks and layer thicknesses are explored to achieve PSCs with long-term stability, which is attributed to decoupling of defects between the Al_2O_3 and ZnO single layers that improves gas-diffusion barrier properties.

Finally, Chapter 9 discusses the key conclusions for this work and directions for future research.

Chapter 2
Theory and Literature Review

2.1 Perovskite solar cells (PSCs)

Perovskite is a mineral that came into existence when a German mineralogist, Gustav Rose, discovered calcium titanate ($CaTiO_3$) in 1839; it is named after a Russian mineralogist, Lev Perovskite. Since then, the term "perovskite" has referred to all compounds with the same crystal structure as calcium titanate with a general formula of ABX_3. The A, B, and X in the perovskite crystal structure are typically represented as a larger rare earth metal cation, a smaller metal cation, and anions (O^{2-}, Cl^-, Br^-, I^-, or S^{2-}), respectively, arranged in octahedral symmetry. In the late 1990s, it was shown that the replacement of an inorganic A cation in a basic cubic perovskite structure by a suitable organic cation provides a material with promising optical properties such as absorption over a wide spectrum, a direct bandgap, charge carrier diffusion lengths in the micrometer range, and defect tolerance[27]. Therefore, the class of hybrid organic–inorganic metal halide perovskite semiconductors takes the common ABX_3 perovskite structure, where A is methyl ammonium (MA) or formamidinium (FA); B is Pb or Sn; and X is Cl, Br, or I (see Figure A)[28][29]. The most commonly used organic–inorganic perovskite for semiconductor device applications is $CH_3NH_3PbI_3$ ($MAPbI_3$). However, the recent trend is to replace $MAPbI_3$ with formamidinium lead-iodide ($FAPbI_3$) and other potential absorbers mainly due to stability concerns which are explained later. Furthermore, selection of the A-site cation (e.g., MA, FA) directly influences the lattice constants and it was found that the bandgap increases with increasing lattice parameter. Therefore, selection of all "A", "B" and "X" is critical to the semiconductor and optoelectronic properties (band gap, absorption cross section, charge carrier motilities etc.) of the perovskite structure, which eventually affects the performance and stability of the PSCs[30].

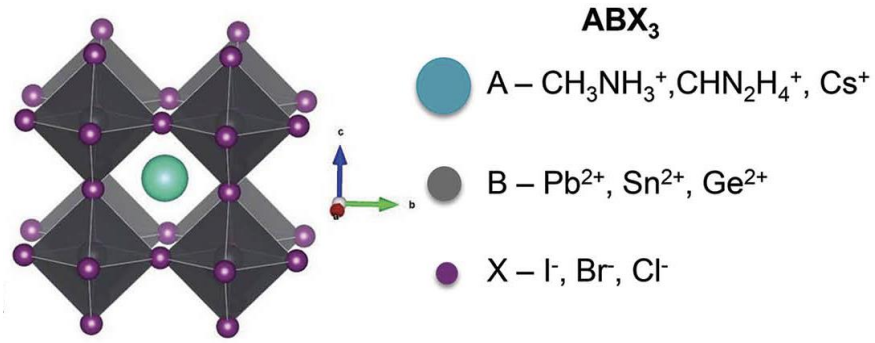

Figure A. Cubic crystal structure of an ABX_3 perovskite with common substituents listed for the A, B, and X positions. Reproduced with permission from [29].

The first reports on solar cells based on perovskite materials are from 2009. Since then, the organic-inorganic halide perovskite solar cells have attracted a great deal of attention due to an incredible device efficiency improvement from 3.8% to more than 25.7%[31]. In addition to these high PCEs reported, their low-cost and convenient fabrication techniques are possible advantages over silicon-based devices that require complicated and costly high-vacuum deposition methods. The PSC, for the first time in the history of PV, has been universally promoted as an economical technology alternative to silicon photovoltaic devices, which still occupy the most dominant position in the current PV market[32].

2.1.1 Structure of perovskite solar cells

The architecture of perovskite solar cells was derived from the dye sensitized solar cell (DSSC) technology. The traditional architecture of DSSCs consisted of a porous TiO_2 scaffold, sensitized by a dye and infiltrated by a liquid electrolyte. Both $CH_3NH_3PbBr_3$ and $CH_3NH_3PbI_3$ were investigated as an alternative to replace the dye material, with moderate success[33]. One key problem with this technology is the inherent instability of devices containing a liquid. Two key breakthroughs fundamentally changed the approach to this type of solar cell, leading to significantly increased PCE

and an unprecedented amount of research attention. The first of these breakthroughs was to replace the TiO_2 scaffold, used to transport electrons, with an insulator(Al_2O_3)[34]. This demonstrated, for the first time, that the perovskite material could effectively transport electrons without the underlying TiO_2 layer. This insight prompted the next advancement; the demonstration of a planar geometry solar cell with a perovskite thin film as the absorber layer[33]. The high efficiency achieved with this device structure demonstrates the ambipolar charge transport of the perovskite material, in that it can transport both positive and negative charge simultaneously.

PSCs consist of an active perovskite layer that is sandwiched between an electron-transporting layer (ETL) and hole-transporting layer (HTL). If the light goes through the ETL, and a transparent conducting layer exists in front of the ETL, then it is known as a n–i–p structure. The opposite one is p–i–n, as shown in Figure Ba,b. The n–i–p structure usually involves depositing the perovskite material onto transparent substrates covered with a compact titanium dioxide (TiO_2), zinc oxide (ZnO) or tin (IV) oxide (SnO_2) layer and an optional mesoporous TiO_2 layer [34]. The p–i–n structure involves depositing the perovskite material onto transparent substrates which are covered with an HTL, such as poly(3,4-ethylene dioxythiophene):polystyrene sulfonic acid (PEDOT:PSS) and poly (bis (4-phenyl) (2,4,6-trimethylphenylamine) (PTAA). Although PSCs have been manufactured using various structural configurations, primarily there are three types of structures as shown in Figure Bc,d,e[35]:

- Regular configuration based on the mesoporous scaffold of TiO_2 nanoparticles.
- The simple planar structure.
- The inverted planar structure.

PSCs with the regular configuration based on a mesoporous TiO_2 layer originated from typical DSSCs. This structure usually consists of a highly crystalline organic-inorganic halide perovskite absorber, a mesoporous electron transport layer (ETL) and a hole transport layer (HTL), sandwiched

between a transparent conducting substrate (TCO) and a metal contact. A thin compact blocking layer of TiO_2 on the TCO is traditionally applied to avoid shunting losses[35].

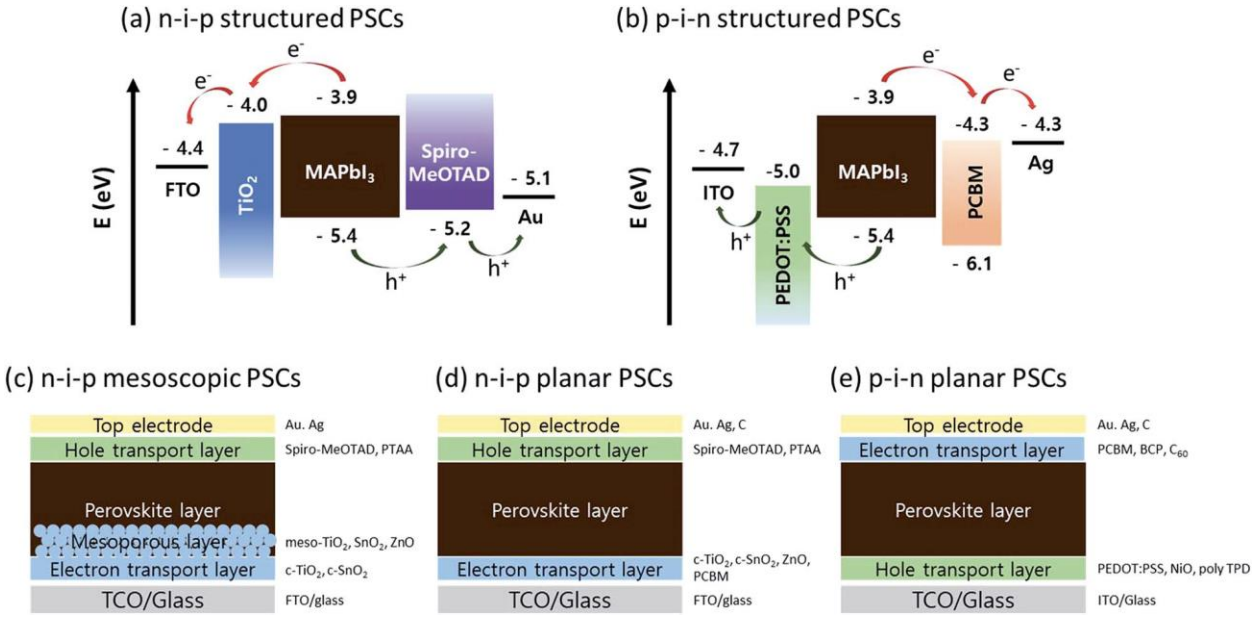

Figure B. Energy band diagram of typical a) n–i–p and b) p–i–n structured PSCs. Different structural configurations of PSCs c) n–i–p mesoscopic, d) n–i–p planar, and e) p–i–n planar PSCs. Reproduced with permission from [35].

In the planar configuration (Figure Bd), a solid perovskite absorber film is surrounded by non-porous electron- and hole-selective contacts. In the third configuration (Figure Be), the device structure is inverted by depositing a hole-selective contact directly onto the TCO substrate and an electron-selective contact on top of the perovskite absorber. These planar-type cells are possible because of the excellent ambipolar diffusion of carriers in perovskite materials[35]. The planar configurations can offer the advantages of simplified device structures and convenient fabrication procedures. In the n–i–p planar structure, modification of the interface between the perovskite and the ETL considerably affects the charge transport and recombination properties and hence the hysteresis of the current density-voltage (J–V) curve, which is the difference of the *J-V* curve during the sweeping in two

directions (from short-circuit towards open-circuit and vice versa)[36]. On the other hand, the p–i–n planar type usually shows negligible hysteresis. However, this type has been made with phenyl-C61-butyric acid methyl ester ($PC_{61}BM$), N-(3,4 methylenedioxybenzoyl)piperidine (BCP) or C60 (buckminsterfullerene) as the ETL and NiO_x or PEDOT:PSS as the HTL, and the stability of the PSCs is relatively low compared to those of the other types, because of the instability of organic materials[37].

The ETL, which extracts photogenerated electrons from perovskite layers and transports them to the cathode, plays an important role in the photovoltaic performance of PSCs. A suitable ETL for PSCs should fulfill some requirements such as good energy alignment between the perovskite materials and the electrode, high electron mobility and good stability in air[38].

An ideal HTL should fulfill some general requirements such as a compatible energy level with the valence band energy (VBE) of the perovskite, sufficient hole mobility as well as excellent thermal and photochemical stability. Spiro-OMeTAD is the most common HTL, however, other HTLs have been developed to achieve high efficiencies (e.g., Triazine-Th-OMeTPA, OMeTPA-FA, TPA-MeOPh, PTAA, TBPC, etc). The HTL mainly affects the open circuit voltage (V_{oc}) of the cells by increasing the recombination resistance, although the addition of a HTL slightly increases the series resistance of the cell[39].

Gold, silver, and carbonaceous materials have been used as the contact material at the cathode. Indium-doped tin oxide (ITO) and fluorine-doped tin oxide (FTO) have been used as the anode contact due to their low electrical resistance, high optical transmittance, and high photoconductivity[40]. However, the ITO-based substrates have low thermal stability, which explains the high efficiencies produced on FTO. Since a high sintering temperature (i.e., around 450 °C) is required for the TiO_2 mesoporous film, the processing of regular PSCs is limited to glass or metal substrates. However, the

other two configurations can be prepared at lower temperature (i.e., less than 150 °C), which enables them to be processed on plastic or polymer substrates[41].

2.1.2 Working principle of perovskite solar cells

The working principle of the PSC is still under investigation. The operating mechanisms of DSSCs help in understanding the charge transport in perovskite solar cells. Perovskite materials act as light sensitizers and ambipolar electron and hole transport materials. A simplified working principle of a typical PSC is presented in Figure C. When light falls on a PSC, the perovskite absorbs the light, thus creating electron-hole pairs. This process involves[42]:

i) Creation of electron-hole pairs upon absorption of light by the perovskite

ii) Charge separations at the junctions of electron and hole transport layers (ETL, HTLs)

iii) Injection of holes and electrons into the respective transport layers, such as Spiro-OMeTAD and TiO_2

iv) Extraction of those charge carriers to the external circuit by contacts.

As shown in Figure C, the energy levels in $CH_3NH_3PbI_3$ are well positioned for electron injection into TiO_2 and hole transfer to spiro-MeOTAD, respectively[5].

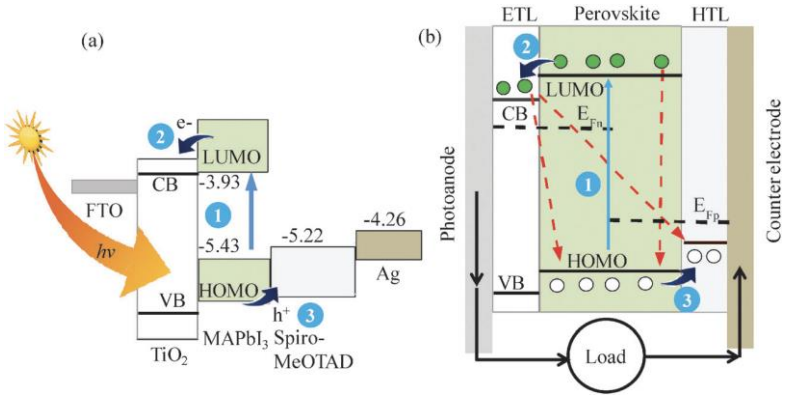

Figure C. a) Schematic representation of the energy band levels of TiO_2/$CH_3NH_3PbI_3$/Spiro-OMeTAD showing the conduction and valence bands of a typical perovskite solar cell. b) The scheme of the main process in PSCs. Reproduced with permission from [5].

Understanding the origins of the electronic and optical properties of the PSC materials is essential to explain the mechanisms of the devices in detail. Depending on the composition of the materials, their properties significantly affect the performance of the PSCs. For instance, diffusion lengths of the free charge carriers play a key role in the device performance. It has been reported that the conventional perovskite absorber $CH_3NH_3PbI_3$ has a lower diffusion length for electrons as compared to that for holes, which limits the active layer thickness to only a few hundreds of nm. Therefore, a mesoporous structure is usually employed when utilizing this absorber. However, composite halide-based perovskites, e.g. $CH_3NH_3PbI_{(3-x)}Cl_{(x)}$, improved the electron diffusion length, which allows planar structures to be employed [43].

2.2 Instability of perovskite solar cells

Although PSCs have already achieved comparable performance against the Si-based PVs, the most challenging issue in perovskite solar cells is the long-term stability. At present, high-efficiency PSCs do not generally retain their efficiencies and degrade in a span of time between a few minutes and a couple of days, whereas the cells which demonstrate better stability lack high efficiency. To improve the stability of PSCs, a systematic understanding of the degradation mechanisms and their effect on the device performance is essential. The degradation of perovskite devices can be divided into two mechanisms: intrinsic instabilities of the perovskite absorber and extrinsic factors which degrade the device as a whole. Research conducted over the past couple of years indicates that the most significant external reason for the degradation and subsequent instability of these cells is decomposition of the perovskite after exposure to moisture and oxygen[44]. For perovskite solar cells to achieve the required stability, future research must focus on improving the intrinsic stability of the perovskite absorber layer, carefully designing the device geometry, and finding durable encapsulant materials,

which seal the device from environmental gases[45]. In the following sections, degradation mechanisms in perovskite solar cells are discussed in detail.

2.2.1 Moisture and oxygen

The degradation of PSCs in the presence of moisture and oxygen is a challenging issue. Oxygen above a certain limit can result in oxidation of the organic components in the PSCs. It was shown that oxygen in a dark atmosphere does not harm the stability of the PSCs[46]. However, in the presence of light, the process of photo-oxidation is almost unavoidable in most of the semiconducting materials. In a complete device, the rate of photo-oxidation depends on the relative rates of the oxidation and electron transfer. If the oxidation rate is faster than the electron transfer rate, there is a higher chance of photo-oxidation. In a comparative study of photo-oxidation for different PSCs architectures, planar structures showed the most promising results due to faster electron transfer rates[7].

Among different factors, the effect of moisture on the perovskite layer is of great interest because of its role in the degradation of perovskite solar cell performance. The moisture instability originates from the hygroscopic nature of amine salt. In addition, the highly hydrophilic properties of the perovskite lead to it readily absorbing water from the environment and inducing the formation of hydrate products. The most commonly used HTL, spiro-OMeTAD, is also unstable in the presence of water. There have been different mechanisms reported in the literature for water-induced degradation in PSCs. By comparing X-Ray Diffraction (XRD) patterns before and after exposure to moisture, most of the research suggests that water acts as a catalyst for the irreversible degradation of the perovskite structure. For $CH_3NH_3PbI_3$, for example, the detailed degradation steps in the presence of moisture can be illustrated by the following series of reactions[1]:

$$CH_3NH_3PbI_3 \overset{\mathbf{H_2O}}{\Longleftrightarrow} CH_3NH_3I(aq) + PbI_2 \qquad \text{Equation 2-1}$$

$CH_3NH_3I(aq) \Leftrightarrow CH_3NH_2(aq) + HI\ (aq)$ Equation 2-2

$4HI\ (aq) + O_2 \Leftrightarrow 2I_2(s) + 2H_2O$ Equation 2-3

$2HI\ (aq) \overset{h\nu}{\Leftrightarrow} H_2\uparrow + I_2(s)$ Equation 2-4

The combination of moisture and heat resulted in even faster degradation due to rapid formation of PbI_2 and loss of the organic component from the crystalline structure. Furthermore, the whole degradation process could be accelerated by the oxidation of HI in the presence of O_2 (Equation 2-3), or the decomposition of HI under UV radiation (Equation 2-4), leading to the conversion of the perovskite entirely to PbI_2[37]. The likely process of $CH_3NH_3PbI_3$ decomposition is displayed schematically in Figure D[47].

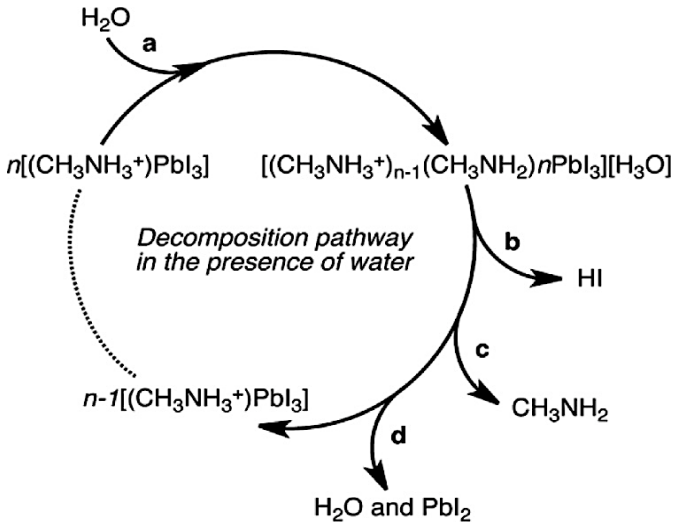

Figure D. Decomposition path way of $CH_3NH_3PbI_3$, in the presence of a water molecule. Reproduced with permission from [47].

This indicates that HI and MA are soluble in water. The irreversible degradation of the perovskite layer is a problem for the lifetime of photovoltaic cells; however, the problem is compounded by the nature of the by-products. As displayed in Figure D, the main by-product of this reaction is PbI_2, which is insoluble in water and causes a change in the film color from dark brown to

a pale yellow after exposure to humidity [1]. As it was mentioned before, an alternative to $MAPbI_3$ perovskite is formamidinium lead triiodide ($HC(NH_2)_2PbI_3$ or $FAPbI_3$) which possesses a narrower band gap and superior phase stability at elevated temperatures compared to $MAPbI_3$. The photo- and moisture stability of $FAPbI_3$ were found to be substantially improved by incorporating cesium into the perovskite structure. The instability of $FAPbI_3$ against humidity results from either conversion of the black phase to yellow phase or accelerated dissociation of the formamidinium cation to ammonia and sym-triazine[48]. Cs-doped $FAPbI_3$ is expected to be more stable because incorporation of Cs stabilizes the black $FAPbI_3$ and the Cs cation does not undergo such a dissociation. In addition, the enhanced photo- and humidity stability of Cs-doped $FAPbI_3$ has been correlated with the decreased lattice parameter, which results in a more tightly surrounded FA cation [49].

2.2.2 UV light

Beside stability issues associated with moisture, another important factor influencing the stability of perovskite solar cells is UV light exposure. The degradation of perovskites by UV light is believed to originate at the TiO_2 layer. A proposed mechanism to explain the degradation process under light exposure is[50]:

$2\mathbf{I}^- \leftrightarrow I_2 + 2\mathbf{e}^-$ (At the interface between TiO_2 and $MAPbI_3$) Equation 2-5

$3CH_3N\mathbf{H_3^+} \leftrightarrow 3CH_3NH_2\ (\uparrow) + 3\mathbf{H}^+$ Equation 2-6

$\mathbf{I}^- + I_2 + 3\mathbf{H}^+ + 2\mathbf{e}^- \leftrightarrow 3HI\ (\uparrow)$ Equation 2-7

First, the TiO_2 extracts the electron from I^- and then breaks the perovskite structure amounting to the formation of I_2 (Equation 2-5). In the presence of water, the acid dissociation constant (pKa) for the hydrolysis reaction of the methylammonium ion (Equation 2-5) is 10.8, implying that the equilibrium of Equation 2-6 should shift to the left. However, the incessant elimination of H^+ in

Equation 2-7 and evaporation of CH_3NH_2 drives Equation 2-6 forward. Finally, the extracted electrons between TiO_2 and methylammonium lead iodide could return to reduce I_2 through Equation 2-7, and the HI produced evaporates quickly because of its low boiling point[51]. It was suggested that the degradation of the perovskite film is slower when a UV filter is used in order to eliminate the UV component from the simulated sunlight illumination [12]. Since PSCs have to pass the more important aging tests under high temperature or high relative humidity (RH) in order to pass the stability standards of thin-film PV, the UV problem is currently not a high priority.

2.2.3 Temperature

Exposure to elevated temperatures also causes degradation of the perovskite layer. Understanding this point is crucial, as the perovskite layer requires an annealing step and, solar modules will be subjected to elevated temperature during operation. Removing the presence of water and air allowed for isolation of the effect of temperature on the film degradation. The literature suggests Equation 2-8 for the temperature-induced decomposition[50]:

$$CH_3NH_3PbI_3 \rightarrow PbI_2 + CH_3NH_2\uparrow + HI\uparrow \qquad \text{Equation 2-8}$$

The resultant CH_3NH_2 could stay within the network of the perovskite, and then disturb the photovoltaic processes. In addition, due to its poor optical behavior and light absorption ability, as well as its higher bandgap, PbI_2 causes device deterioration. Furthermore, the mechanism of dimensional expansion in the perovskite structure at low and high temperatures, as well as the device architecture degradation is not yet clear[52]. For this reason, to avoid decomposition due to high temperature, the use of thermally resistant materials is the most suitable option. Replacing the methylammonium (MA+) ion with other cations such as formamidinium (FA+) has led to significantly improved stability compared to $MAPbI_3$. In contrast to $MAPbI_3$, $FAPbI_3$ was confirmed to be free from phase transitions at temperature between 25 and 150 °C[38].

Adding small amounts of inorganic cesium (Cs) in a ‘‘triple cation’’ (Cs/MA/FA) configuration resulted in a stable perovskite film under elevated thermal conditions [53]. Since, Cs has an ionic radius smaller than that of the MA or FA cations, the inclusion of Cs in the perovskite lattice stabilizes the desirable α-phase by reducing the perovskite's tolerance factor, permitting a stable α-phase to exist at elevated temperatures [54].

2.2.4 Stability of other layers

Apart from the instability of the perovskite layer itself, the stability of other components, such as the transport layers and electrodes, needs to be considered.

Spiro-MeOTAD is the most commonly used material in PSCs for hole transporting purposes. It generally needs the addition of 4-tertbutylpyridine (TBP) to reduce charge recombination, and bis(trifl uoromethane)sulfonimide lithium salt (Li-TFSI) to increase hole mobility. However, Li-TFSI salt is extremely hygroscopic and deliquescent. Water molecules may easily penetrate into the PSC device without encapsulation via the HTL, leading to the decomposition of the perovskite. In addition, acetonitrile, which is the conventional solvent for Li-TFSI, can also corrode the perovskite[55]. It was established that small-sized pinholes commonly exist in Spiro-OMeTAD layers. These pinholes not only can create pathways for moisture to diffuse through the thin film, but also can allow elements in the perovskite (e.g., iodine) to migrate to the top surface. Both cause degradation of the solar cell[5]. Efforts have been made to replace the reactive dopant with inert additives to improve the charge transport characteristics of the undoped hole-transport material. [39]. At the same time, hydrophobic polymers including tetrathiafulvalene derivative (TTF-1) are credited with a three times higher stability compared to devices with spiro-OMeTAD[45].

Gold, silver and aluminum are the most commonly used counter electrode materials for high-efficiency perovskite solar cells. Recently, it has been found that reactions between iodine-based

decomposition products, such as HI from perovskite materials, and traditional metal electrode materials, such as Ag, can lead to the formation of silver iodide (AgI). The formation of AgI escalates the perovskite decomposition when the material is exposed to an ambient environment. Figure E shows a schematic diagram depicting the five proposed steps which lead to the formation of AgI. These processes include[56]:

i) Diffusion of water through the Spiro-OMeTAD HTL via pinholes.

ii) Moisture-induced decomposition of the $CH_3NH_3PbI_3$. Iodine containing volatile species, e.g., MAI or HI, are formed during the decomposition.

iii) These iodine-containing compounds migrate through the Spiro-OMeTAD to the Ag electrode.

iv) Surface diffusion of iodine containing compounds.

v) The formation of AgI, which causes the electrode to change from a reflective metal to a yellowish colour.

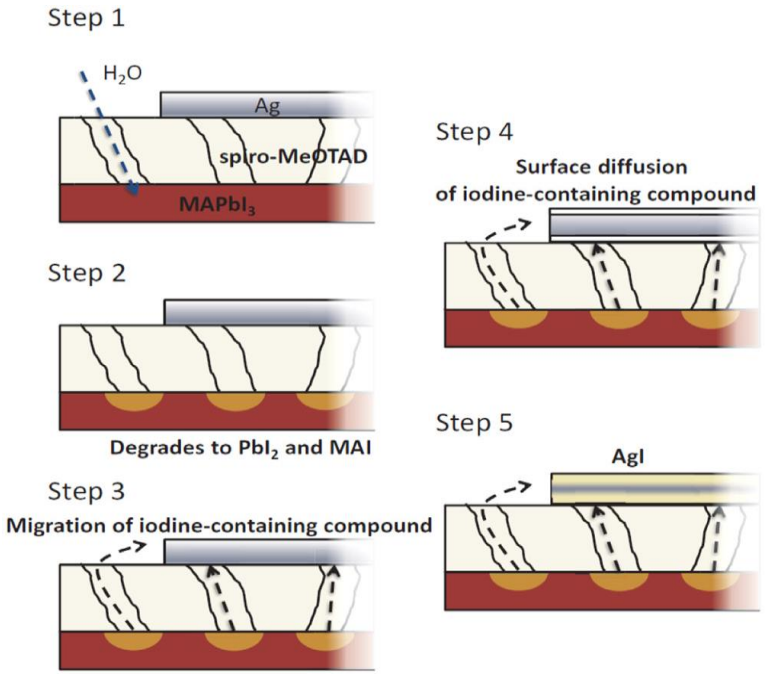

Figure E. Schematic diagram illustrating the proposed mechanism leading to the formation of AgI in PSCs with Ag electrodes. Reproduced with permission from [56].

Regarding the top conductive electrode, a carbon-based electrode can be an ideal choice to help solve the instability issue induced by moisture because of its hydrophobic property. Meanwhile, the cost of carbon is significantly lower than that of commonly used gold or silver electrodes. In addition, its favorable compatibility with printing methods avoids the usage of vacuum evaporation. However, perovskite solar cells with carbon electrodes usually suffer from the problem of energy level mismatch at the perovskite/carbon interface, so a polymer interlayer (e.g., poly-ethylene oxide (PEO)) is widely used to adjust interface properties, especially the energy-level alignment[57].

2.3 Attempts to improve stability of perovskite solar cells

The above discussion leaves no doubt that the perovskite used in PSCs must be protected from moisture. There are numerous efforts to improve the stability of perovskite solar cells, such as the employment of a thin blocking layer between the perovskite and the hole transporting material, moisture-blocking hole transporters, and hydrophobic carbon electrodes. These approaches can be split into two major strategies; firstly, developing extrinsic stability through the use of proper encapsulation to prevent degradation caused by moisture and oxygen, and secondly, research to improve the intrinsic stability of perovskite materials as well as interfaces[38]. These strategies will be discussed in the following sections.

2.3.1 Improve internal stability

One of the main causes of perovskite instability is the hydroscopic nature of the organic cations, especially methylammonium. One way to improve perovskite solar cell stability is to replace the organic “A-cation” in the ABX_3 structure. It should be kept in mind that the size of the “A-cation” can have a noticeable effect on lattice structure. Different cation sizes can shift the phase of the perovskite crystal into an undesirable state for photovoltaic activity. Formamidinium has been used as an

alternative to MA since it is a similar size. Although formamidinium lead iodide ($FAPbI_3$) exists in a non-perovskite hexagonal phase at room temperature, the addition of a small amount of Cs into FA-based perovskites assists the crystallisation of the "black perovskite" phase (α-phase). Additionally, the narrower bandgap of FAI-based perovskites causes an increase in J_{SC}, since it can generate photocurrent over a larger spectral region. Researchers suggested that, unlike MAI, FAI perovskite films were stable when exposed to temperatures up to150°C in air. This stability was related to the crystal structure, as FAI does not undergo a phase transition in the temperature range from 25 to 150 °C[58].

Researchers have employed chemical engineering to alter the stability of the commonly used $CH_3NH_3PbI_3$. Many additives have been trialled to increase the stability of perovskite solar cells, such as alkylphosphonic acid u-ammonium chlorides (ABPA)[59], butylphosphonic acid 4-ammonium chloride (4-ABPACl) and tetra-ethyl ammonium (TEA)[60]. These additives can form cross-links between adjacent perovskite grains, which leads to the formation of a smoother capping layer, with improved infiltration into the underlying TiO_2. It was shown that the inclusion of this cross-linking additive significantly hinders the moisture induced decomposition of the perovskite layer by reducing moisture vulnerabilities at grain boundaries in the perovskite layer[61]. The integration of a cross-linked polystyrene (PS) network within perovskite films is one of the other effective methods to make a highly stable perovskite layer. The use of the organic moiety (PS) in combination with an inorganic crystalline material ($MAPbI_3$) leads to suppression of the ion migration, dark currents, and trap density which is attributed to the insulating nature of the PS network. Furthermore, the direct interaction between PS and PbI_2 could lead to better crystallization kinetics, and thus a larger grain size for the perovskite layer, which results in better performance of PSCs[62].

Another change that can improve perovskite solar cell stability is using 2D perovskite films, which are much more stable in the presence of moisture, compared to the commonly used 3D analogues[63].

2.3.2 Encapsulation

Protecting the perovskite materials from external degradation catalysts, such as ambient moisture and UV light will be vital for long-term stability of the PSCs. The most promising technique to enhance the stability of a perovskite solar cell is full encapsulation of the device, which plays a role in the commercialization of perovskite solar cells. Devices without encapsulation commonly exhibit severe degradation under ambient conditions and continuous illumination after several hours while encapsulated devices exhibited longer lifetimes.

2.3.2.1 Encapsulation materials

The encapsulation materials should be low cost, dimensionally stable, easy to deposit, and at the same time they should have a relatively high dielectric constant, light transmission, and resistance to ultraviolet (UV) degradation and thermal oxidation. The water vapour transmission rate (WVTR) and oxygen transmission rate (OTR) are the steady state rates at which oxygen gas and water vapour can penetrate through a film, and hence are important properties of an encapsulation layer. The light transmission through the encapsulation materials is also important to understand how it will affect the device performance. Requirements for encapsulation materials are listed in Table 2.1. To meet these encapsulation requirements, different approaches have been adopted such as single layer and multilayer encapsulation with organic and/or inorganic materials[64]. An alumina-based layer with a good combination of the required properties is one of the most commonly used materials to improve device stability under moisture exposure[65]. Thin films of silicon (Si) and silicon nitride (SiN_x) are also noted to be suitable for encapsulating solar cells[66][67]. This is primarily due to their excellent thermal and environmental stability, and a wide range of refractive indices. In addition, because of the hydrophobic properties of Si, it has low moisture pick-up in a damp-heat environment and in total water immersion [68].

In terms of organic encapsulation materials, ethylene vinyl acetate (EVA), a copolymer of ethylene and vinyl acetate, is one of the most widely used encapsulating materials, due to its high weather resistance and long-term reliability under long periods of exposure to different elements. Ethylene methyl acrylate (EMA) has a potential advantage over EVA because of its thermal stability and good mechanical behavior at low temperature. These qualities match with some of the requirements for the use of these materials for encapsulation purposes [69]. Poly vinyl butyral (PVB) can also be used as an encapsulation layer; it is already widely applied in modern mass production of thin film solar cells[9].

Table 2.1. Specifications and requirements for encapsulating materials for the protection of perovskite solar cells from oxygen and moisture[65].

Characteristics	Specification of requirement
WVTR	10^{-3}-10^{-6} g.m^{-2}.day^{-1}
OTR	10^{-3}-10^{-5} cm^{3}. m^{-2}.day^{-1}.atm^{-1}
Glass transition temperature (T_g)	<-40 °C (during the winter in deserts)
Total light transmission	> 90% of incident light
Water absorption	<0.5 wt% (20°C-100%RH)
Tensile modulus	<20.7 mPa (>3000 Psi) at 25°C
UV absorption degradation	None (>350 nm)

2.3.2.2 Encapsulation techniques

Much work on the effectiveness of various encapsulation techniques has been performed in the field of photovoltaics to enhance the long-term stability of solar cells. One of the most effective sealing techniques, which exhibits very low permeation of water vapor and oxygen, is attaching a cover glass lid to the device using a slow-permeation epoxy-type sealant. However, glass encapsulation cannot be applied on flexible devices[69]. Some research showed that spinning a layer of amorphous Teflon on top of the device could also improve the performance lifetime of a device, but photo-induced changes in the polymer morphology and subsequent trap formation should be considered[70]. Thin-film

encapsulation (TFE) can be considered as one of the alternative candidate techniques for the encapsulation of PSCs as shown in Figure F. Single-layer thin films are attractive because of the simplicity of the manufacturing process compared to multilayer thin film encapsulation methods that require multiple processing steps[9].

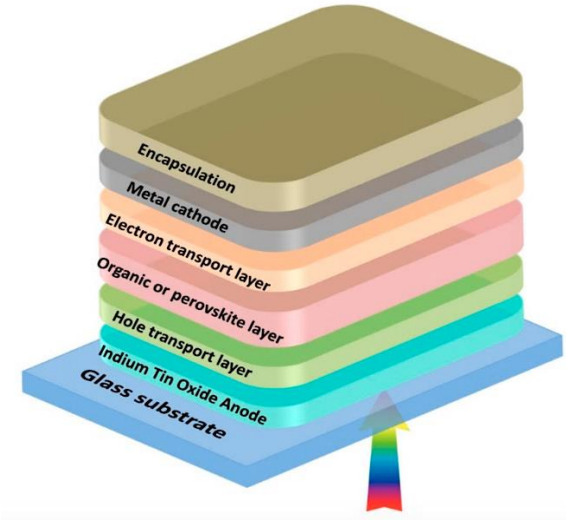

Figure F. A schematic diagram of a perovskite solar cells with an encapsulation layer. Reproduced with permission from [9]**.**

There are several challenges in the utilization and development of thin-film encapsulation because of the potential damage to the PSC during the deposition processes. To fabricate the TFE, different kinds of deposition processes have been adopted including plasma-enhanced chemical vapor deposition (PECVD), sputtering, and atomic layer deposition (ALD)[13]. Such methods require a high energy input or temperatures higher than at least 90℃, which might severely degrade the PSC performance. The challenge lies in the fact that the inorganic layer deposition is greatly influenced by the deposition temperature and the energy input in the inorganic-layer deposition determines the barrier properties of the TFE. For example, decreasing the process temperature in ALD reduced the WVTR of a TFE, since the ALD film had a lower density with a large amount of carbon-related impurities and

hydroxyl groups [15]. A summary of previous reports on TFEs is shown in Table 2.2, highlighting the perovskite device structure, encapsulation materials and the stability performance.

It is crucial to develop new methods to maximize the barrier performance of the TFE while minimizing any PSC damage during the deposition of the encapsulation layer[71]. In this regard, spatial atomic layer deposition is a promising alternative to PECVD and conventional ALD, as SALD is capable of rapidly depositing gas barrier layers with outstanding film quality on various substrates[72]. Encapsulation layers deposited by SALD have the potential to allow perovskite devices to perform under environmental conditions and become a viable source of energy for the future. This method will be discussed in the following section.

Table 2.2. Summary of representative PSCs encapsulated with different materials and methods and their stabilities at different test conditions.

PSC structure	Encapsulation material and method	WVTR ($g.m^{-2}.d^{-1}$)	Long term stability	References
Glass/FTO/TiO_2/$(FAPbI_3)_{0.85}(MAPbBr_3)_{0.15}$/spiro-MeOTAD /Au	ALD-Al_2O_3	1.8×10^{-2} (at 45 ˚C-100%RH)	25% reduction in PCE after 2250 h at 25 ˚C -50% RH in dark	[73]
FTO/c-TiO_2/mp-TiO_2/$MAPbI_3$/PTAA/Au	ALD-Al_2O_3	9.0×10^{-4}	97% of its initial PCE after 300 h at 50 °C, 50% RH	[12]
ITO/PEDOT:PSS/perovskite/$PC_{61}BM$/ZnO(CBL)/Ag	ALD-Al_2O_3	9.0×10^{-4}	Over 90% of its initial PCE after 10 days at 30 °C, 65% RH	[74]
Glass/ITO/NiO/$MAPbI_3$/$PC_{61}BM$/ALD-TiO_2/Ag	ALD-Al_2O_3	9.0×10^{-4}	93% of its initial PCE after 1000 h at 25 °C, 40–60% RH)	[75]
ITO/NiO/$MAPbI_3$/$PC_{61}BM$/ TiO_2/Ag	ALD-Al_2O_3	9.0×10^{-4}	97% of its initial PCE after 1000 h at ambient conditions	[76]
ITO/$CH_3NH_3PbI_3$/SnO_2/spiro-MeOTAD/Ag	PEALD-Al_2O_3 + EG	1.3×10^{-5}	96% of its initial PCE after 2000 h at ambient condition	[77]
glass/FTO/mp-TiO_2/bl-TiO_2/ $MAPbI_3$/PTAA/Au	iCVD-pV_3D_3/ALD-Al_2O_3 Multilayer	8.5×10^{-5}	97% PCE retained after 300 h shelf at 50 ˚C and 50% RH.	[20]
Glass/FTO/c-TiO_2/$MAPbI_3$/SpiroOMeTAD/MoO_3/Al	ALD-SiO_2 TFE + UV-curable epoxy glue sheet	10^{-4}	and 11% PCE loss after 432 h outdoor aging test (ISOS-O-1)	[78]
ITO/NiO/$Cs_{0.17}FA_{0.83}Pb(Br_{0.17}I_{0.83})_3$/$PC_{60}BM$/ITO/Ag	ALD-SnO_2/zinc tin oxide (ZTO)	-	Stable after 1000 h at 85 °C and 85% RH	[79]
FTO/TiO_2/$MAPbI_3$/ spiro-MeOTAD /Au	Spin coated-Al_2O_3	9.0×10^{-4}	95% of its initial PCE after 350 h at simulated full sunlight	[80]
ITO/TiO_2/C_{60}/Perovskite/PTAA/Au	Hexamethyldisiloxane (HMDSO)	-	Maintained 92% initial PCE after 3100 h storage at 85 °C and 25% RH	[81]
IZO-PET/TiO_2/ $MAPbI_3$/spiro-OMeTAD/Au	Commercial barrier film	1×10^{-3}	Maintained initial PCE after 500 h storage in ambient conditions	[82]

2.4 Atmospheric pressure spatial atomic layer deposition (AP-SALD)

2.4.1 The principles of ALD and SALD

A thin film can be defined as a layer of material with a thickness varying from approximately a nanometre to several micrometres. Thin films can be deposited using a variety of techniques, which are based on either chemical or physical processes. Thin film coating finds applications in many fields such as nanotechnology, the environment and energy (e.g., lithium batteries), fuel cells and photovoltaics as well as medical and biologic applications. Thin film deposition can be divided into three main categories: solid-, liquid-, and gas-based deposition methods, which include physical vapour deposition (PVD) and chemical vapour deposition (CVD).

ALD is an advanced CVD technique [83] based on the sequential exposure of a substrate to chemical precursors which directly react with the surface to form sub-monolayers of a film. This technology results in the precise deposition of films on the surface of a substrate at the atomic scale. ALD found its first application in thin-film electroluminescent (TFEL) flat panel displays. Recently, ALD has raised interest from new application areas, such as photovoltaics, semiconductor devices, organic electronics and many others due to the growth in technology and materials selection. Unlike CVD, in ALD the precursors are pulsed sequentially, they are not pumped simultaneously. The most noticeable distinction lies in the self-limiting characteristics for precursor adsorption in which the reaction is restricted to the sample surface in each half-cycle. This is achieved by introducing two or more precursor vapours and a purge gas alternately into a chamber at different times and in a sequence of pulses[84]. An ALD process with two precursors is usually used in depositing metal oxide films; one is the metal source and the other is the oxygen source (oxidant). The synthesis of Al_2O_3 thin films is a common example of an ALD process, where trimethyl aluminium (TMA) and water have been

used as precursors to create a thin film. The steps of a single deposition cycle are as follows, which are demonstrated in Figure G [85]:

1) The metal precursor (e.g., $Al(CH_3)_3$) is supplied in the reactor chamber to form a monolayer on the substrate based on this reaction:

$$AlOH + Al(CH_3)_3 \rightarrow Al\text{-}O\text{-}Al(CH_3)_2 + CH_4$$

2) The excess first precursor and the by-products are purged, usually by evacuation.
3) The second precursor (e.g., H_2O) is then injected and reacts with the chemisorbed layer forming a monolayer of the desired material (i.e., Al_2O_3) based on this reaction:

$$Al\text{-}O\text{-}Al(CH_3)_2 + H_2O \rightarrow Al\text{-}O\text{-}Al(OH)_2 + 2\ CH_4$$

4) The excess second precursor plus by-products (CH_4) are purged or evacuated.
5) The cycle is then repeated until a very precise thickness is achieved.

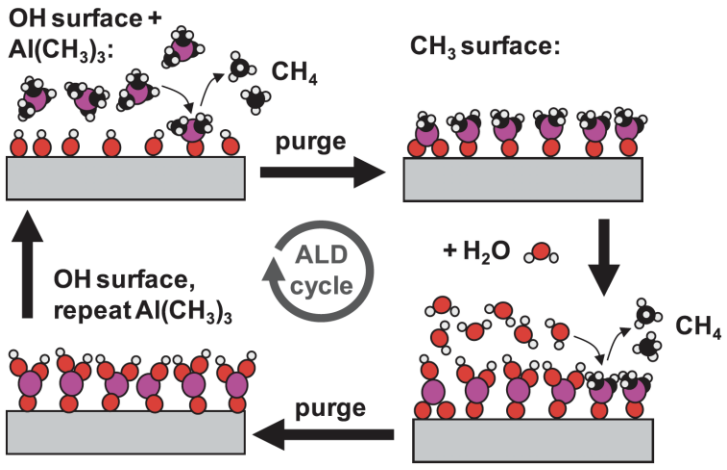

Figure G. Schematic diagram of one cycle of atomic layer deposition (ALD) of aluminum oxide using trimethylaluminum ($Al(CH_3)_3$) and water, separated by inert gas purging steps. Reproduced with permission from [85].

ALD is attractive because it can create high-quality films with uniformity and conformality on complex three-dimensional surfaces at low temperatures. However, industrial applications require high-throughput and low-cost production techniques to make them economically viable. Unfortunately,

these parameters are the main drawbacks of ALD. As mentioned in Table 2.3, ALD usually involves processing in a vacuum, which makes it complicated and expensive to scale up. A challenge in scaling up ALD for high-throughput commercial-scale production of thin films is that larger deposition chambers will be required, which will lengthen the evacuation, dose and purge times[86]. Additionally, ALD of large substrate areas on the order of square feet is also limited by the size of the deposition chamber. Moreover, it has a very slow deposition rate, which leads to high precursor gas usage and energy[87].

Table 2.3. Advantages and disadvantages of ALD, Reproduced with permission from [87].

Advantages	**Disadvantages**
• High-quality films 1. Control of the film thickness 2. Excellent repeatability 3. High film density 4. Amorphous or crystalline film 5. Ultra-thin films • Conformality 1. Excellent 3D conformality 2. Large area thickness uniformity 3. Atomically flat and smooth surface coating • Challenging Substrates 1. Gentle deposition process for sensitive substrates 2. Low temperature and stress 3. Excellent adhesion 4. Coats Teflon • Low-temperature processing • Stoichiometric control • Inherent film quality associated with self-limiting, self-assembled nature of the ALD mechanism • Multilayer	• The time required for the chemical reactions • The economic viability • Very high material-waste rate • Very high energy-waste rate • Nanoparticle emissions

Recently, several “new” approaches to ALD have been proposed to meet these challenges. Many of these approaches share a common feature: spatial separation of the half reactions. Spatial ALD (SALD) has been the most popular due to its conceptual simplicity and the high deposition rates that

can be achieved. The difference between conventional temporal ALD and spatial ALD lies in separating the precursors in space rather than in time (see Figure H). In SALD, the different precursors are supplied constantly to the substrate but in different physical locations (typically separated by inert gas regions), and it is the substrate (or injector that supplies the precursors) which moves from one location to another. Films are then grown by alternatively exposing the substrate from one precursor region to the other, by going across the inert gas regions (Figure Hb). There are (at least) two zones where a half reaction can take place in the presence of a substrate. The first metal precursor reacts with the surface forming a saturated monolayer, if the substrate is present in such a half-reaction zone for a sufficient period of time. Then, the substrate is moved to the second half reaction zone, where the second precursor reacts with the previous monolayer forming one ALD monolayer of material. Finally, the sample returns to the first precursor region, again going across the inert region where any by-products and excess precursor are purged. To achieve thicker films, this sequence is repeated for the desired number of cycles. Based on the application, the substrate position could be fixed and the gas supplies could be moved, or some combination of the two. Notably, the purge steps between the precursor injections in conventional ALD become obsolete. So, this approach allows much faster deposition rates, which are mainly limited by the precursor reaction kinetics, but this can be of the order of a few milliseconds when using planar substrates[19]. By adjusting the conditions to allow precursor mixing in the gas phase, CVD can also be performed in the same system[16]. AP-CVD conditions are attractive for device manufacturing, as it has been shown that higher deposition rates are obtained, while still producing smooth, pinhole-free, conformal films with thicknesses proportional to the number of cycles[88].

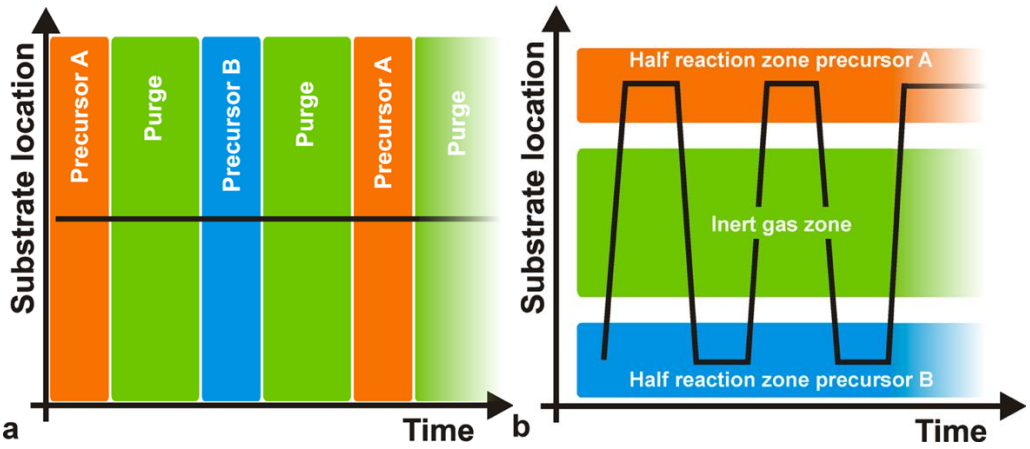

Figure H. Schematic representation of the ALD process with the variation in time, position of the substrate (black line), and precursors (colored blocks) in a) conventional ALD and b) spatial ALD, Reproduced with permission from [19].

A complete separation of the precursors with no intermixing is required as the main essence of ALD. In conventional ALD this is achieved through using the purge steps in between the precursor exposure steps. In spatial ALD, the half reactions are separated using a combination of physical barriers and shields of inert gas, where the gas shield width should be designed wide enough to prevent the inter diffusion and cross-reactions between the precursors. Therefore, precursors never reside in the same reactor volume. Consequently, deposition will only take place on the substrate and no parasitic deposition will occur on the reactor walls. This results in a significant reduction of precursor consumption depending on the specific design of the various spatial ALD concepts[89]. Summarizing, the three main characteristics of spatial ALD can be outlined as:

1) Physical separation of the half-reactions' zones
2) Movement of the substrate and/or gas injector head
3) Prevent precursor mixing with a barrier between the half-reaction zones

An alternative approach to ensure precursor separation is the use of a short distance between the precursor injector and the substrate (typically below 100 μm) as illustrated schematically in Figure

I, combined with suitable gas barriers and exhaust. In this configuration, referred to as “close proximity SALD”, the reactor has separate alternative channels exposing the different gas regions one by one to a substrate that moves underneath the reactor (see Figure Ia,b). There are shields of inert gas again between and around the reaction zones to separate the precursor flows. These gas shields can also act as gas bearing which facilitate frictionless movement between the reactor head and substrate. In addition, gas bearings can make the reactor completely independent of the environment due to sealing off the reaction zones properly. As a result, the system is able to operate under atmospheric pressure conditions. Moreover, since the precursor regions are very small, there is a possibility of having smaller and simpler designs which are compatible with roll-to-roll processing. Furthermore, it is potentially very easy to scale up, modify and customize. Therefore, this approach is very readily applicable both in laboratory and industry.

The distance between the reactor and substrate can be minimized to several tens of micrometers when a gas bearing is used to make sure that ALD takes place, and reactions are limited to the substrate surface[18]. However, by increasing the gap between the reactor head and the substrate, the different precursors can mix in the gas phase above the substrate giving an AP-CVD reaction mode. In the AP-CVD mode, faster deposition rates can be achieved since the growth per cycle is larger than the value for AP-SALD conditions (using the same precursors and deposition temperature), because the reaction is not limited to an adsorbed layer on the surface. Since the growth per cycle is still constant, the thickness of films deposited using AP-CVD conditions can be controlled precisely by simply adjusting the number of cycles used for deposition[16].The design used by Levy et al. which consists of a deposition reactor head in which the different gas flows are distributed along the parallel channels is illustrated in Figure Ic[18].

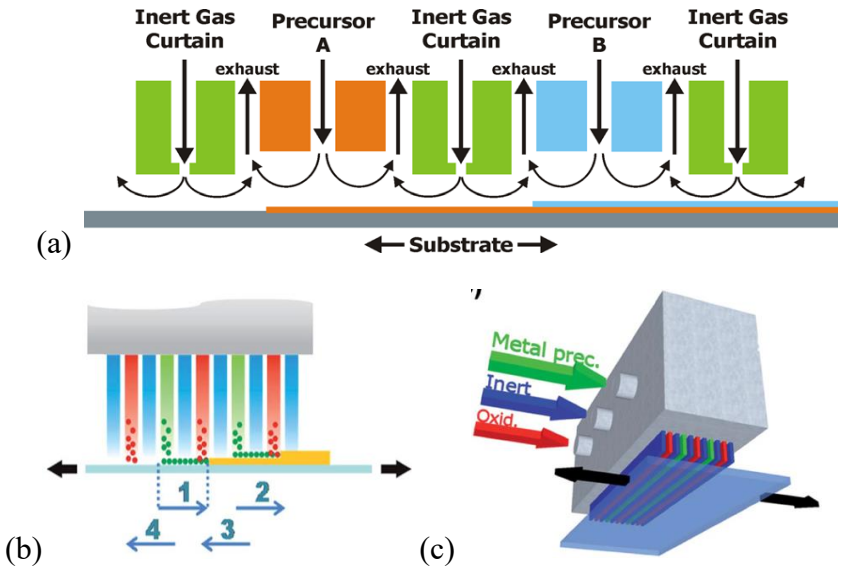

Figure I. a,b) Principle of a close-proximity SALD approach. c) Scheme of the deposition reactor head designed by Kodak. Reproduced with permission from [18].

The reports discussed above show the versatility of AP-SALD to deposit a variety of metal oxide thin films at relatively quick deposition rates and at low deposition temperatures without the need of a vacuum environment. The electronic, optical and physical properties of these films can be tuned by varying the deposition temperature, precursor partial pressure and introducing dopants.

While it is clear that there are many advantages to AP-SALD, it is important to note the current challenges and limitations with the technique. Thin films deposited by AP-SALD have primarily consisted of metal oxides. The "open-air" deposition means the films are prone to an increased incorporation of oxygen from the atmosphere[90]. This may have negative effects on the optical or electrical properties of the film. The deposition of non-oxide films by AP-SALD, such as silver, has been demonstrated[91] but introduces increased complexity such as the inclusion of a plasma-enhanced reactor. Unlocking the deposition of other non-oxide films by AP-SALD is an ongoing research effort. Additionally, atmospheric deposition with highly pyrophoric precursors such as TMA is challenging to reproduce[92]. This is because ambient oxygen and variable humidity can act as an additional oxygen

sources and unintentionally increase the growth of the film. Furthermore, the reactor head flow channels are prone to blockages as they are directly exposed to the atmosphere and allow for deposition to occur in the channel itself. At the lab scale, further reproducibility issues arise in manual setting of the distance between the reactor head and the substrate. An unintentional non-uniform spacing can lead to an over mixing of the precursors resulting in higher growth rates in certain areas of the deposition and a non-uniformity in film thickness. Lastly, precursors that have been successfully used for conventional vacuum-based ALD may not necessarily translate well for use with AP-SALD due to challenges in obtaining sufficient vapor phase of a precursor at atmospheric pressure. In these cases, additional techniques such as heating or nebulization are required which increase the complexity of the system[93].

2.4.2 Application of SALD for photovoltaic devices

New fields of application for spatial ALD range from active and passive components for thin-film transistors to active components as well as barrier passivation layers for next-generation solar cells[18]. These applications often require manufacturing techniques with feature sizes of the order of several nanometers, for which ALD already showed its suitability in the lab. However, they should be applied at low cost and at industrial throughputs. Spatial ALD is being investigated for barrier layers, solar cell passivation, and thin-film electronics due to the process-speed advantage. Therefore, several materials including intrinsic, doped and mixed metal oxides (e.g., Al_2O_3, ZnO, AZO, TiO_2, Cu_2O) have been deposited using SALD and were studied for display or photovoltaic applications[94]. Many groups used the SALD technique to deposit Al_2O_3 passivation layers for silicon solar cells, and good results have been achieved[19]. There were many efforts to deposit transparent conductive oxides which are a key component of optoelectronic devices, especially solar cells[17]. The SALD technique was used for the deposition of active layers for new generation solar cells. Table 2.4 summarizes selected reports on

the deposition of ZnO films by AP-SALD. Diethyl zinc (DEZ) and water were used as the Zn and oxygen precursors, respectively. Depending on its intended use, it is often advantageous to dope the ZnO to enhance its electrical conductivity and/or alter its optical bandgap.

Table 2.4.Selected reports on the deposition of ZnO by AP-SALD.

Precursors	Dopant	Growth Rate (A°/cycle)	T (°C)	Application	Ref.
DEZ + Water	N (NH_3)	1.7	200	Thin Film Transistor	[94]
DEZ + Water	-	1.8	70-250	-	[95]
DEZ + Water	Al (TMA)	1.2	200	-	[96]
DEZ + Water	Mg ($Mg(CpEt)_2$)	0.28	150	Solar Cells	[97]
DEZ + Water	S (H_2S)	0.7-1.5	100-200	Solar Cells	[97]

Besides Al_2O_3 and ZnO, other binary oxide films such as copper (I) oxide (Cu_2O), titanium dioxide (TiO_2) and tin oxide (SnO_2) have been deposited by AP-SALD. The metal precursors, reported growth rates and deposition temperatures used for these films are listed in Table 2.5. For example, it was shown that a 15-nm-thick amorphous TiO_2 layer can act as an efficient hole blocking layer in bulk heterojunction solar cells [34]. Therefore, researchers have taken advantage of the high throughput of SALD for the realization of many fundamental studies on photovoltaic device physics. Since SALD allows a much faster deposition of samples with different crystallinity and properties than ALD, it provides large batches in short times to study device physics and efficiency. For example, SALD has been used to deposit extremely thin Nb_2O_5 layers on top of deposited TiO_2 layers in hybrid and quantum dot-based cells which showed better performance with the Nb_2O_5 interlayer[98]. Finally, SALD has also been used to deposit transparent conductive materials such as TCO, for which photovoltaics are a main applications [88].

Table 2.5. Selected reports on other binary metal-oxide films deposited by AP-SALD.

Material	Precursors	Growth Rate (A°/cycle)	T (°C)	Application	Ref
Cu_2O	Cupraselect	0.06	150-225	Solar Cells	[94]
TiO_2	$TiCl_4$	1.5	100-350	Solar Cells	[34]
SnO_2	TDMASn	1.5	80	Solar Cells	[2]

During the last years, the study and implementation of high quality SALD films in new generation photovoltaic devices can be classified in the following categories[18]:

1) Studying the feasibility of the SALD technique for ultra-fast deposition of high-quality layers that can be used in devices.
2) The deposition of films with superior properties compared to other low temperature methods.
3) Fundamental studies of using doped oxide films in new-generation solar cells.
4) Surface nanoengineering with SALD thin films to enhance solar-cell efficiencies

2.4.3 Alumina and complex oxides thin film deposition using SALD

To date, Al_2O_3 is one of the most common and highly studied SALD films due to its technological importance. Al_2O_3 is an attractive candidate for use in the field of electronics due to its excellent properties for instance; high thermal stability, good chemical stability, dielectric properties and strong adhesion to various kinds of substrates[99]. Table 2.6 summarizes selected reports on the deposition of Al_2O_3 by AP-SALD.

Table 2.6. Selected reports on the deposition of Al_2O_3 by AP-SALD.

Precursors	Growth Rate (A°/cycle)	T (°C)	Application	Ref
TMA + Water	1.2	200	Thin Film Transistor	[100]
TMA + Water	1.2	200	Solar Cells	[86]
TMA + O_2 Plasma	1-2	70-200	Temperature sensitive substrates	[101]
DMAI + Water	0.9-1.3	100-300	-	[86]

In particular, Al_2O_3 has been considered as an attractive barrier material against moisture and oxygen. It has been previously established that ALD Al_2O_3 provides an adequate level of surface passivation for Si solar cells, therefore it can be used as an encapsulation layer in organic and perovskite solar cells theoretically[102]. However, the ALD process has not yet been successful to prepare effective Al_2O_3 barrier layers for PSCs. This is probably because the substrate temperature during the ALD process should be kept low (less than 150˚C) to prevent thermal damage to the perovskite materials during the prolonged ALD process. Low temperatures do not provide a sufficient amount of thermal energy for all the surface reactions to complete[15]. A recent study attempted to overcome these problems by adopting spatial ALD to rapidly deposit Al_2O_3 TFE at a temperature that is high enough to provide good barrier properties and at a speed that is fast enough to avoid perovskite damage[72].

Most often TMA is used as the metal source and water as the oxidant for the deposition of alumina in SALD. Nevertheless, some researchers reported an improvement in film quality when ozone was used as the oxygen source, instead of water. This was attributed to a higher film density and/or a lower content of impurities within the film. Furthermore, ozone-based processes allowed lower substrate temperatures due to the higher reactivity of ozone[103]. Therefore, the material properties and process conditions are strongly affected by the type of the oxidant used for deposition. Recently, hydrogen peroxide (H_2O_2) has also shown feasibility as an oxidant to deposit high-quality oxide thin films by ALD [104][105]. Since process conditions such as deposition temperature or amount of reactant exposure required for ALD are determined by the surface reactions of each reactant, detailed analysis of the surface chemical mechanisms of these oxidants is important[106]. The reaction coordinate diagrams for H_2O, H_2O_2 and O_3 on the Al–CH_3* surface sites, as proposed by [106], are shown in Figure J. The reactivity towards oxidation of surface Al-CH_3^* is determined by the overall reaction energy and activation energy for the rate-determining step when different oxidants react with

Al-CH_3 surface species. This can potentially impact the growth rate of films, and the currently observed reactivity can serve as an indicator for the feasibility of low-temperature ALD processes.

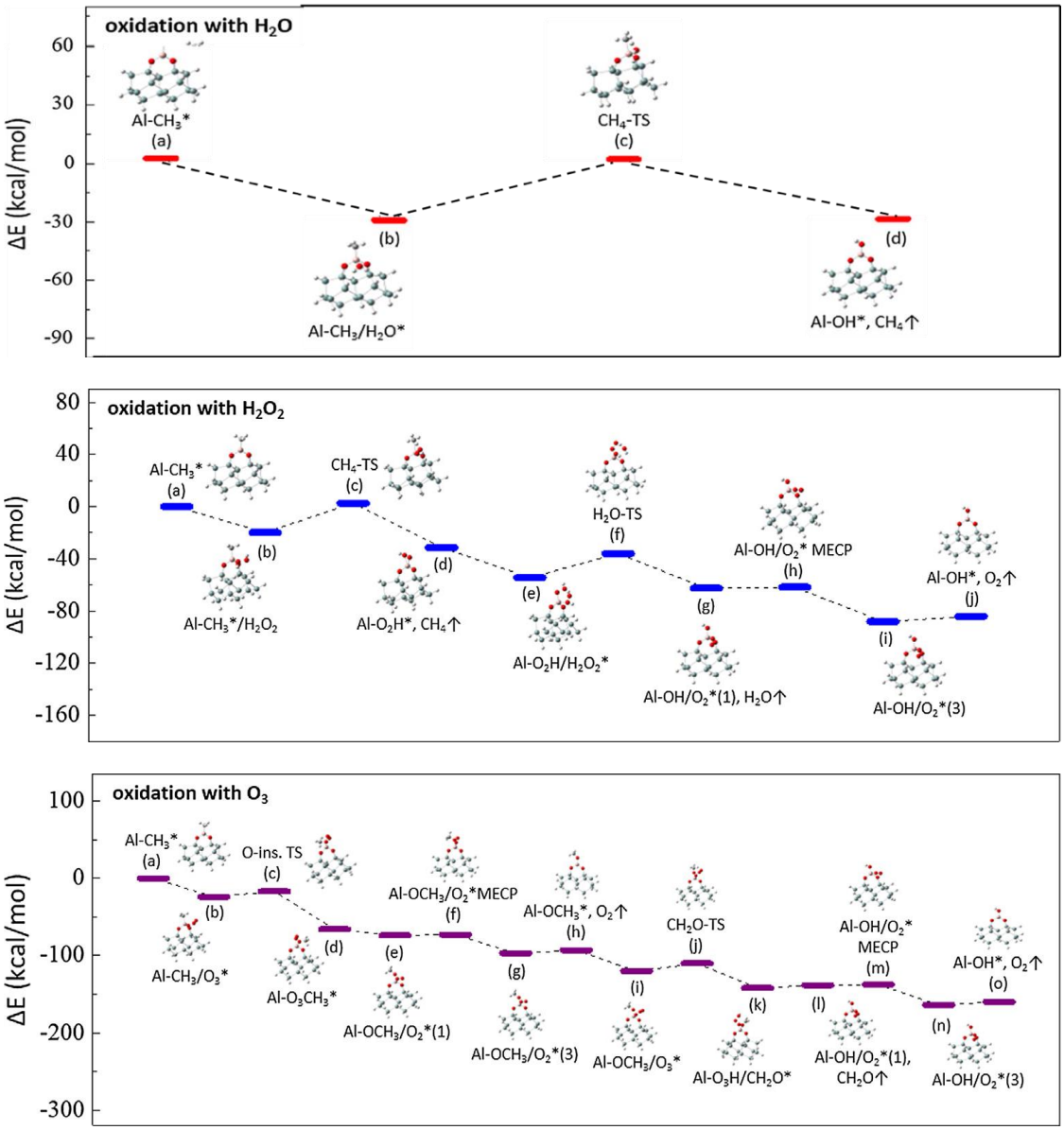

Figure J. Proposed reaction coordinate diagram for H_2O, H_2O_2, and O_3 on the Al–CH_3 surface site. Reproduced with permission from* [106].

For thin-film gas diffusion barriers based on Al_2O_3 grown by spatial ALD, an extremely low WVTR on the order of 10^{-5} g.m^{-2}.d^{-1} was reported[107]. Spatial ALD Al_2O_3 layers show saturation

behavior, typical for ALD-type growth, even at low deposition temperatures (<80 °C), resulting in thin films with low roughness and a relatively high physical density. In addition, it was shown that the speed of the moving substrate can be chosen as high as 60 mm/s in the spatial ALD process[108].

While SALD has traditionally been used to grow binary oxides, it also enables the deposition of more versatile chemistries, such as ternary and multicomponent oxides, nitrides and sulphides[109]. Multicomponent oxides are widely used in industrial applications because their physical properties, including surface roughness, refractive index, hardness, and conductivity, can be controlled over a wide range by varying the film stoichiometry[110]. Doped oxides are the most common family of the ALD-grown multicomponent materials. The basic purpose of doping is to tune the material properties (optical, electrical, and structural) to optimize the film for a specific application[14]. Perhaps, the most investigated applications for ALD of doped oxides can be found in optoelectronics. It is possible to tailor the properties of the material by depositing a mixture of binary oxides with a well-defined composition (e.g., Si:HfO_2[111], and Al:TiO_2[112]) or by forming a nanolaminate structure with alternating thin layers of constituent oxides (e.g., ZrO_2/Al_2O_3[113], and Al_2O_3/ZnO[114]). Nanolaminate structures provide precise control over the average film stoichiometry, although the concentrations of the different metal elements and the physical properties of the films might be inhomogeneous along the growth direction[115]. In recent years, success in the synthesis of complex oxides with ALD is a strong motivation to expand SALD for even a wider range of materials and to explore new functionalities and applications of complex oxides. Moreover, the industrial demands for highly conformal, pinhole-free and uniform thin films on large area and/or flexible substrate has driven the recent development of multicomponent oxides by SALD[116].

Chapter 3

Experimental and Thin Film Characterization Methods

3.1 AP-SALD of AlO_x thin films

Alumina-based thin films were deposited in open-air conditions using our custom-built, dual atmospheric-pressure spatial atomic layer deposition/chemical vapor deposition (AP-SALD/SCVD) system [88]. This system employs a close-proximity reactor-head configuration, as shown in Figure I[26], [95]. Figure K shows the reactor head used within the system, where the films are deposited. In this area, the heated stage with the selected substrate horizontally oscillates underneath the reactor head and the three micrometre adjustment knobs are used to adjust the reactor-substrate separation. Four different gas channels are installed in the AP-SALD reactor head for the metal precursors, oxygen precursor, nitrogen gas and exhaust.

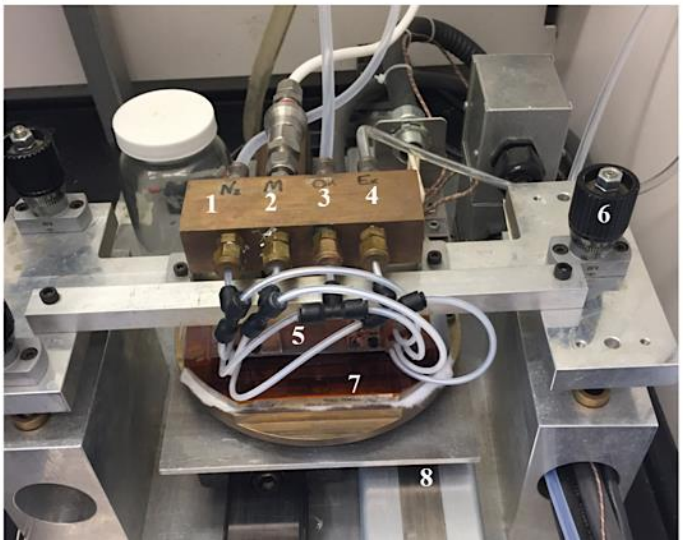

1. *Nitrogen curtain inlet*
2. *Metal precursor inlet with quick-disconnect*
3. *Oxygen precursor inlet*
4. *Exhaust outlet*
5. *Reactor head*
6. *Reactor height control micrometre*
7. *Heated stage*
8. *Linear actuator*

Figure K. AP-SALD reactor head in use by the Functional Nanomaterials group at the University of Waterloo[117].

To create flows of gaseous precursor chemicals, liquid precursors are "bubbled" with a controlled flow of inert nitrogen gas (Ultra High Purity 5.0 Nitrogen, from Praxair). The precursor gases are combined with an additional stream of inert gas at a higher flow rate that serves to push the precursor to the reactor as shown in Figure L. The reactor has parallel gas outlet channels along its bottom surface, as shown in Figure Ic. Outlet channels flowing inert gas separate the precursor flows and seal off the reaction zones, thus the system can operate independent of the environment under atmospheric pressure conditions. The entire system is installed in a conventional fume hood and the substrate stage can be heated to 400°C.

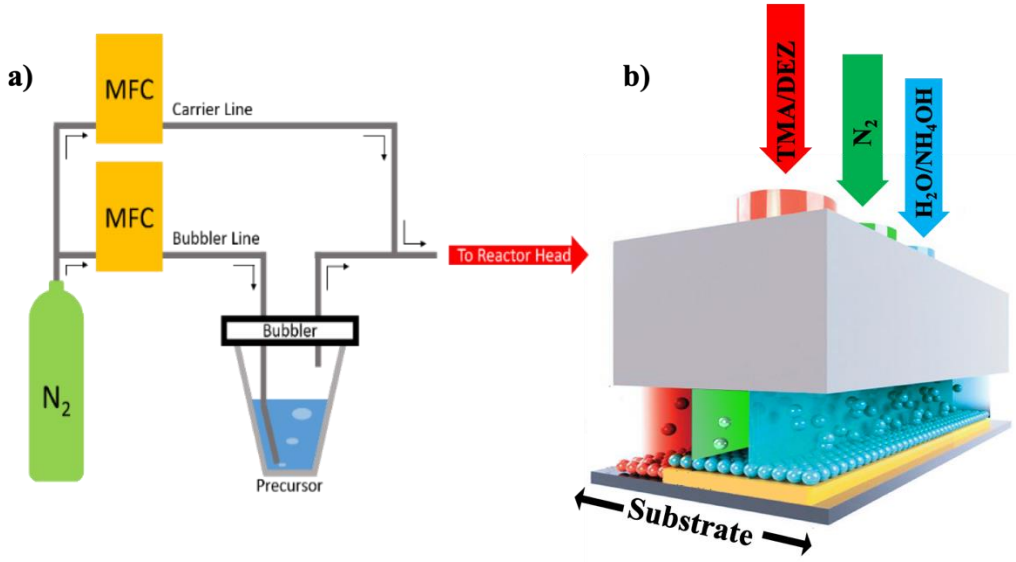

Figure L. a) Schematic of the precursor bubbler and carrier line in AP-SALD system. Reproduced with permission from [117]. b) a schematic of the reactor head used in our AP-SALD system. Aluminum precursor (red), inert nitrogen (green), and oxidant and nitrogen (blue) gas streams are shown. Reproduced with permission from [26].

Deposition by SALD is affected by process parameters such as the substrate oscillation speed, reactor-substrate separation distance, substrate temperature, the flow rate per channel on the reactor head and the precursor concentrations.

An important advantage of the close-proximity approach based on a reactor head is that it can be adjusted to switch between pure SALD mode and a more CVD-like mode. Atmospheric-pressure spatial chemical vapor deposition (AP-SCVD) can occur if the gas flow rates and reactor-substrate spacing are such that the metal and oxygen precursors are not perfectly isolated by the inert nitrogen gas channels. AP-SCVD conditions are attractive for device manufacturing, since higher deposition rates are obtained, while still producing smooth, pinhole-free, conformal films with thicknesses proportional to the number of cycles[88]. Therefore, the AP-SALD system operating in AP- SCVD mode has the unique benefit of producing ALD quality films in a fraction of the time. Fast deposition rates are advantageous for high-volume production of functional devices[90][118].

In this thesis, experimental conditions were selected such that the inert gas flow and exhaust strength are insufficient to prevent mixing of the reactant vapors in the gas phase during the oscillation of the substrate, directing the system to operate in AP-SCVD mode. AP-SCVD could also be achieved by using a large reactor-substrate spacing[90]. It was previously shown that AP-SCVD deposition was obtained using a reactor-substrate spacing of 50 μm and different flow rates for the metal and oxidant precursors[100]. In this work, an even larger reactor-substrate spacing of 100 μm was used to ensure some mixing of the precursors in the gas phase above the substrate, where the reactions are no longer surface self-limited.

For thin film encapsulation, the highest possible deposition temperature should be chosen in order to secure the highest barrier performance, while simultaneously keeping the temperature low enough that the PSCs remain free from damage. The $FA_{0.92}MA_{0.08}PbI_3$ perovskite layer used in this study is expected to be unstable above approximately 150°C [119]. However, most PSCs suffer from thermal stress at high temperatures due to the poor thermal stability of the organic small-molecule-based hole-transporting materials, including Spiro-OMeTAD and additives[52]. Spiro-OMeTAD has shown a low thermal stability above 85°C due to a large drop in the glass transition temperature (T_g),

which causes severe recrystallization[120]. In this study, different deposition temperatures were tested and a temperature of 130˚C was chosen, since even the n-i-p PSC with Spiro-OMeTAD exhibited no degradation during the AP-SCVD process at 130˚C. This is attributed to the much shorter AP-SCVD times (typically a few minutes), which allow a higher deposition temperature (e.g., 130°C) to be used to produce dense, conformal and uniform oxide films[19]. The heated stage was oscillated back and forth at the speed of 50 mm/s to expose the substrate to the alternating precursor flows.

Trimethylaluminum [$Al_2(CH_3)_6$, (TMA), 1.0M solution in heptane, from Fisher Scientific] and distilled water were usually used as aluminum and oxygen precursors, respectively. Ammonium hydroxide (NH_4OH) solution (28% ammonia (NH_3) in water) was used as an oxidant (instead of water) to deposit nitrogen-doped AlO_x thin films. Diethyl zinc [$Zn(C_2H_5)_2$, (DEZ), 96% from Fisher Scientific] was used to introduce Zn atoms into the alumina, either by adding a cycle of ZnO after several cycles of AlO_x based on the desired Zn doping level or by co-injecting TMA and DEZ into the deposition zone with different flow rates to obtain different doping levels. In order to study the effect of different oxidants on the thin-film properties, water was replaced with hydrogen peroxide (30% H_2O_2 in water) and ozone (O_3). The precursor bubbling rates and carrier flow rates used for the various studies are detailed in Chapter 4 to 7.

3.2 Perovskite solar cell fabrication

In order to examine the impact of the PSC configuration on their performance and stability, two different PSC structures were fabricated. The optimized device architectures are as follows:

1- n-i-p planar structure consisting of FTO/SnO_2/$FA_{0.92}MA_{0.08}PbI_3$/spiro-OMeTAD/Ag

2- p-i-n planar structure consisting of FTO/PTAA/$FA_{0.92}MA_{0.08}PbI_3$/$PC_{61}BM$/BCP/Ag, as illustrated in Figure M.

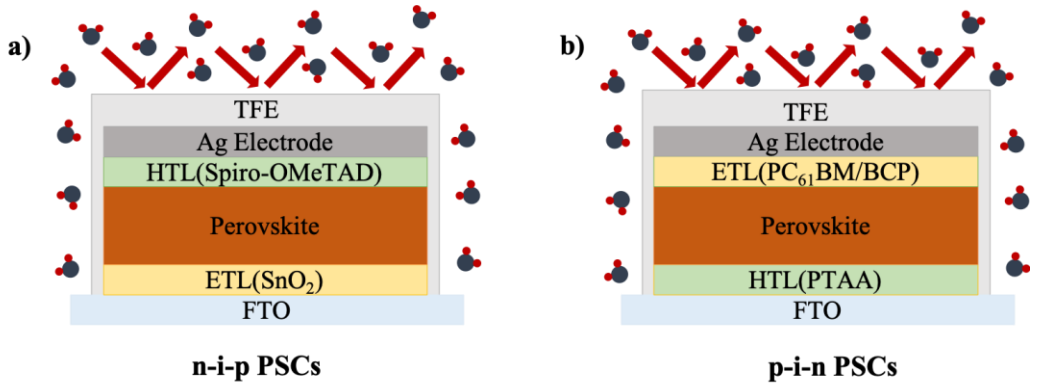

Figure M. Schematic of a) n-i-p and b) p-i-n perovskite-solar-cell structures protected with thin film encapsulation.

3.2.1 n-i-p perovskite solar cells

Devices were fabricated on fluorine-doped tin oxide (FTO) coated glass (1.6 cm × 1.6 cm, 14Ω/sq). Initially the FTO-coated glass was cleaned sequentially under ultrasonication in detergent, DI water, acetone, ethanol and isopropanol for 30 min for each solvent, and then dried on a hotplate at 150 °C for at least 2 h. Before usage, the cleaned FTO was treated with ultraviolet ozone for 30 min.

An electron transport layer of tin oxide nanoparticles (2.67% SnO_2, diluted with Milli-Q water) was deposited by spin-coating at 3000 rpm for 30 s and annealed in ambient air at 150 °C for 30 min. The samples were transferred while hot (T = 150 °C) to a nitrogen-filled glovebox (H_2O and O_2 levels ~1 ppm). The perovskite layer was fabricated by a two-step deposition method and each solution were filtered through 0.45 μm polytetrafluoroethylene syringe filters. First, 1.5 mol L^{-1} PbI_2 was dissolved in dimethylformamide (DMF)/dimethyl sulfoxide (DMSO) (9:1 by volume) and stirred at 70 °C for 10 h. The warm PbI_2 was spin-coated at 4000 rpm for 20 s, and then a drop of the mixed solution containing FAI: MAI: MACl (90 mg: 9 mg: 9 mg in 1 mL of IPA) was added to the spinning substrate for 30 s. The as-prepared samples were annealed at 150 °C for 8 min, and slowly cooled to room temperature.

To prepare the hole transport layer, 30 μL of 4-*tert*-butyl pyridine, 29μL of tris(2-(1H-pyrazol-1-yl)-4-tert butylpyridine)cobalt(III) tri[bis(trifluoromethane)sulfonimide] (Co-TFSI) (300 mg Co-TFSI in 1 mL acetonitrile), and 18 μL of bis(trifluoromethane) sulfonimide lithium salt (Li-TFSI) stock solution (520 mg Li-TFSI in 1 mL acetonitrile) were added to 1000μL of a 72.3 mM Spiro-OMeTAD solution in chlorobenzene, and the resulting solution was syringe filtered through a 0.45 μm polytetrafluoroethylene filter. After filtering, the hole transport layer was deposited on top of the perovskite layer at a spin rate of 3000 rpm for 30 s. The films were allowed to dry in an open Petri dish overnight in the glovebox. Finally, 100-nm-thick Ag top electrodes was deposited by thermal evaporation at a base pressure of 5×10^{-6} mbar.

3.2.2 p-i-n perovskite solar cells

The procedures of cleaning the FTO-coated glass and depositing the perovskite and Ag layers are similar to those of n-i-p device. After cleaning the FTO-coated glass, a layer of PTAA (2 mg/mL in toluene) was spin-coated onto the cleaned FTO substrates at 5000 rpm for 30 s and the substrates were annealed at 100 ºC for 10 min in the glove box. It was noted that to increase the coverage of the perovskite films on the PTAA, the PbI_2 solution was deposited by spin-casting. A layer of $PC_{61}BM$ (20 mg mL^{-1} in chlorobenzene) was spin-coated on the perovskite films at 1500 rpm for 30 s and annealed at 100 ºC for 7.5 min. Then a BCP layer (0.75 mg mL^{-1} in IPA) was prepared by spin-coating at 3000 rpm for 30s. 100 nm of Ag was deposited by thermal evaporation.

3.3 Water vapor transmission rate (WVTR) measurements

Water vapor transmission rates (WVTRs) are the steady-state rates at which water vapor can penetrate through a film. Ultralow WVTRs between 10^{-4} and 10^{-6} g/(m^2 day) are required for stable operation of thin-film photovoltaic devices[121]. No commercial instrumentation is available to measure ultralow WVTRs. The best currently available commercial capability is the MOCON

Aquatron Model 1 instrument that has a sensitivity down to WVTR 5×10^{-4} g/(m^2 day) (MOCON, Minneapolis, MN)[122]. The "calcium test" using the oxidation of Ca films is one approach that has been employed to measure ultralow WVTRs[123]. The Ca test can be used in several adaptations. The most widely utilized methods are based on either the electrical conductance or the oxidized area of the Ca film[124]. The water that is transported through the gas diffusion barrier oxidizes the Ca metal by the reaction: $Ca + 2H_2O \rightarrow Ca(OH)_2 + H_2$[125]. The electronic Ca test measures the decrease in conductivity that occurs due to Ca corrosion resulting from the diffusion of moisture and oxygen through the barrier film. Optical methods record images of the encapsulated Ca film at regular intervals to monitor the rate of corrosion of the initially highly reflective Ca to almost transparent Ca oxide. The images are then used to calculate the WVTR [126].

Although the Ca test has high sensitivity, there are numerous assumptions employed to extract WVTR values from Ca test experiments. One assumption is the linearity of the electrical conductance or oxidized area with Ca film oxidation. This assumption of linearity has not been independently confirmed and it has been questioned given recent evidence for the inhomogeneous oxidation of Ca films[127]. The non-linearity of Ca oxidation raises doubts about the accuracy of the WVTR determined by the Ca test though it has been proposed that reliable WVTRs can be obtained at short lag times[125]. Another assumption is the final oxidation state of the Ca film. Both $Ca(OH)_2$ and CaO are possible and could affect the WVTR value[128]. One additional problem is the presence of residual H_2O which could oxidize the Ca film without passing through the barrier layer[129].

In this study, we employed an optical Ca test to evaluate the gas diffusion barrier properties of deposited TFE layers based on the method introduced by Kumar et al[130] because the optical Ca test offers several advantages over electrical calcium tests, including the ability to conduct many parallel measurements at a high throughput, lower cost, and the flexibility to operate in various environmental

conditions. Also, since the TFE layers can be directly deposited on the Ca film, the photographic imaging can observe spatial information and locate defects in the encapsulation layers[131].

3.3.1 Ca test sample preparation and WVTR calculation

The Ca test requires that the Ca film be deposited and prepared for the gas diffusion barrier measurements under a controlled oxygen-free environment. To meet this requirement, a thermal evaporator located in a N_2 glove box was used.

To prepare the Ca films, 2.8cm×2.8cm glass slides were cleaned in an ultrasonic bath with deionized water, acetone, and isopropanol subsequently. The blown-dried substrates were transferred into the glovebox then they were dried using a hotplate at 150 °C for 1 h and cooled down in a petri dish inside the glovebox. Kapton tape was used to attach 3D-printed shadow masks to the glass slides, as shown in Figure Na. The masks covered a 5 mm strip on each side of the glass substrate and left a 1.8×1.8 cm^2 area in the middle section to be coated with a Ca layer. A 200 nm Ca film was deposited with a deposition rate of approximately 2 Å/s and the film thickness was monitored using a quartz crystal sensor. The Ca films were opaque with a mirrorlike appearance.

In order to minimize the exposure to air, the Ca samples were vacuum sealed inside the glovebox and transfer to the AP-SALD system, where the vacuum bag was opened immediately prior to TFE deposition. But, it is important to note that the atmospheric nature of the TFE deposition increases the chance of having residual water that may be trapped within the substrate or barrier layers, which was previously shown to influence the measured WVTR value in H_2O based techniques[126]. This implies that the WVTR measurements in this work may slightly overestimate the actual WVTR through the TFE layer. The Ca-coated samples were then placed on the AP-SALD stage and encapsulation layers were deposited directly on the Ca layer, as detailed in following chapters. A 60 nm thickness was chosen for the TFE layers because a previous study to measure the barrier

performance showed an improvement with barrier thickness up to 80 nm[132]. Although the ALD and CVD growth mechanism for AlO_x is well understood on most of surfaces, it is reported that metal-oxide deposition on metal surfaces is quite different due to a very slow nucleation process, resulting in a different growth rate[133]. In the case of the Ca surface, a detailed growth mechanism has not been reported yet, but the deposition of all AlO_x thin films on calcium was monitored using ellipsometry to ensure that 60-nm-thick TFE layers were deposited. After the desired barrier thickness was deposited, the AlO_x-coated Ca samples were removed from the AP-SALD system and transferred to a N_2 glove box to seal the edge using epoxy glue. A poor edge seal can allow moisture ingress through the edge seal and limit the test results and duration[123].

The samples were then placed into an ESPEC SH-222 benchtop environmental chamber that allows the user to control the temperature and humidity inside it. Measurements were taken at two conditions, 25°C-55% RH and 65°C-85% RH, to calculate the water vapor transmission rates through the gas barrier films[134]. A Nikon D7100 camera was used to monitor the samples visually, as shown schematically in Figure Nb. In order to take pictures, the samples were temporarily removed from the environmental chamber every 15 minutes to 1 h for the duration of the sample test.

IMAGEJ software was used to convert color images of the encapsulated Ca films to black and white images. The color images were first converted to gray-scale images. A gray-scale threshold value was then set to produce binary images of black and white pixels. The gray-scale threshold value was determined visually based on a comparison between the colored image and the black-and-white image. Based on this procedure, IMAGEJ was then able to provide an accurate measurement of the white areas that correspond to oxidized Ca film. In some instances, poor resolution and sample lighting led to inaccuracies in the converted photographic images. These errors could be minimized through careful

observation, manually removing the reflections from the measured oxidized area and excluding the degradation from the edges from the evaluation.

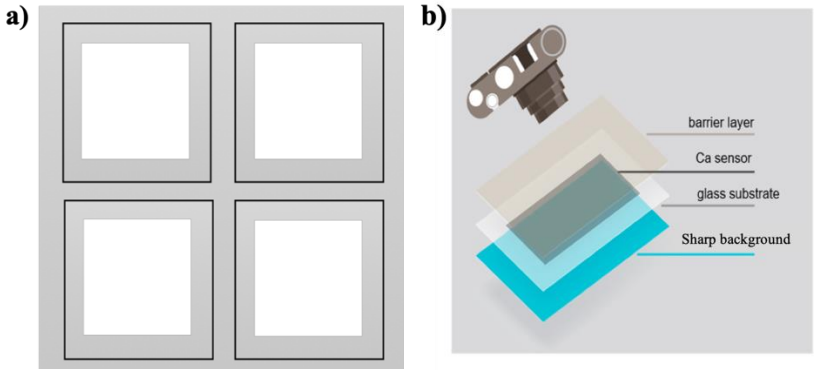

Figure N. Schematic of a) 3D-printed shadow mask used to deposit Ca in desired surface area on glass substrate, and b) optical Ca test set up.

The WVTR, or permeation rate, P, is determined from the photographic images using[126]*:*

$$P = n \frac{M(H_2O)}{M(Ca)} \delta . h . \frac{\Delta A}{\Delta t} \qquad \text{Equation 3-1}$$

In Equation 3-1, n is a stoichiometric coefficient which is 2 for water oxidation, $M(H_2O)$=18.015 g/mol is the molar mass of water and M(Ca)=40.078 g/mol is the molar mass of Ca. δ=1.54 g/cm^3 is the bulk density of Ca and h=200 nm is the height of the Ca metal film. The change in oxide area is represented by ΔA and the time interval, in days, between the photos used to measure Δt. Plotting the oxidized area (A) versus time results in a graph that shows the rate at which the Ca film is oxidized. The slope of this graph represents the rate of increase in the oxidized area, which is equal to ΔA /Δt. As an example, a ΔA/Δt graph and calculation steps for one TFE was provided in Figure (Appendix A).

3.4 Perovskite solar cell characterization

The current-density-voltage (J-V) curves of the perovskite solar cells were recorded with a Keithley 2400 source meter in air, under simulated AM 1.5G solar illumination from a Sciencetech UHE-NL-150 Class AAA Solar Simulator. The illumination intensity was set at 100 mW/cm^2 using a NIST-calibrated silicon reference solar cell, without correcting for spectral mismatch, and the voltage was swept from 1.1 V to −0.1 V with a sweep rate of 0.02 V/s. The active area of the cells was 0.1695 cm^2 without any shadow mask. Example J-V curves and performance parameters of both p-i-n and n-i-p PSCs are provided in Figure A-2 and Table (Appendix A).

Stability studies for PSCs are drawing increasing attention, but despite the already large number of publications, it is difficult to directly compare the available results due to a lack of consistency in experimental procedures and parameters reported. Therefore, it is a priority to develop unified procedures for testing and reporting PSC stability by the research community. International Summit on Organic Photovoltaic Stability (ISOS) protocols are a reasonable starting point[134]. A solar cell cannot pass or fail ISOS stability tests. Instead, ISOS protocols are intended primarily for lab-scale devices and aim to ensure the comparability of testing performed at different laboratories, enabling successful round-robin experiments, and to assist in improving the quality and relevance of published data[134].

I chose dark-storage studies (ISOS-D) because they estimate a cell's shelf life under ambient conditions when not exposed to light and provide information on the tolerance of the solar cells to aggressive atmospheric components naturally present in air like moisture, oxygen and elevated temperatures[134]. The ambient atmosphere plays a crucial role in determining the lifetime of perovskite absorbers because interaction with ambient species can promote perovskite decomposition, which quickly deteriorates device performance[1]. The impact of these factors is taken into consideration in the ISOS-D-1 test (25°C-55%RH)[134]. Another important stress factor is temperature.

Elevated temperatures are applied to study the thermal stability of solar cells and to accelerate the degradation induced by moisture[52]. The ISOS-D-3 damp heat test (65°C-85% RH) was conducted to consider the impact of humidity when devices are kept at high elevated temperatures[134].

For measuring the shelf life and to study the performance of the TFE layers developed in this work, the PSC performance was monitored over extended periods. n-i-p and p-i-n PSCs were coated with 60 nm of different TFE layers and then the encapsulated cells and control cells without an encapsulation layer were exposed to the accelerated test conditions ISOS-D-1 (dark, 25°C-55%RH) and ISOS-D-3 (dark, 65°C-85% RH) in the ESPEC SH-222 benchtop environmental chamber[134]. The PSCs were briefly removed from the environmental chamber at present times to measure the device performance, then placed back in. The PCEs were normalized with their initial values and plotted as a function of the storage time to represent the cell performance. The time required for the PCE to drop to 80% of the initial efficiency is commonly denoted T_{80} and often serves as a figure of merit for solar cell stability. It is, therefore, an optimal minimum test time, which was used in the study. Extrapolation of degradation data (or readily achieved T_{80} lifetimes) can be used to evaluate the cell lifetime energy yield.

3.5 Material and thin film characterization

Film thickness measurements: The Sopra GES5 ellipsometer with a wavelength range of 200–1800 nm was used to measure the thickness and the refractive indices of the thin films, which were modeled using the Cauchy formula.

Atomic force microscopy (AFM): A Dimension 3100 atomic force microscope (AFM) was used to measure the roughness of the thin films.

*Scanning electron microscopy (SEM): S*EM images were captured using a Zeiss Leo 1530 with an electron high tension (EHT) of 5 kV.

X-ray diffraction (XRD): XRD measurements of thin films that were deposited on silicon substrates were performed with an XPERT-PRO diffractometer with Cu Kα radiation (X-ray wavelength of 0.154 nm).

X-ray photoelectron spectroscopy (XPS): A VG Scientific ESCALAB 250 system was used to examine the surface of the films using Al Kα X-rays. The films were deposited on silicon substrates for XPS analysis.

.

Chapter 4

Nitrogen-doped Alumina TFE layers

4.1 Introduction

Metal oxynitrides are commonly used as a gas-barrier coating in the food packaging industry due to their excellent oxygen- and water-vapour-barrier performance[135]. Improvements in a number of film properties have been gained by replacing aluminium oxide with aluminium oxynitride[136], [137]. This is due to the fact that variable concentrations of aluminum, oxygen, and nitrogen lead to the development of a ternary AlO_xN_y system with tuneable properties. The film properties can be tailored between those of pure Al_2O_3 and aluminum nitride (AlN), depending on the application requirements[138]. It was reported that anion doping of Al_2O_3 can decrease the defect density and oxygen and moisture diffusion [139]. Nitrogen-doped alumina ($N\text{-}AlO_x$) has been successfully deposited using chemical vapor deposition, ALD, and plasma-enhanced ALD[140][141]; however, studies have shown that the gas-barrier properties of Al-based films depend on many factors, including the film thickness and type of deposition technique[135][137]. To the best of our knowledge, deposition of $N\text{-}AlO_x$ films using an AP-SALD system has not been demonstrated or studied. Therefore, in this work, $N\text{-}AlO_x$ films are deposited using an AP-SALD system and their deposition rate, microstructure and barrier properties are studied as a function of the film composition. The $N\text{-}AlO_x$ films are then employed as encapsulation layers on both p-i-n and n-i-p perovskite solar cells. The AP-SALD process conditions are optimized to prevent degradation of the perovskite layer and the $N\text{-}AlO_x$ composition is optimized to maximize the PSC stability, which is measured under ISOS testing conditions[134]. As a result, we successfully enhance the stability of the PSCs (T_{80}=855 h at 25˚C-55% RH) with a single TFE deposited rapidly in open-air.

4.2 Experimental

AlO_x and N-AlO_x thin films were deposited in open-air conditions using our custom-built, dual atmospheric-pressure spatial atomic layer deposition/chemical vapor deposition (AP-SALD/SCVD) system, which employs a close-proximity reactor-head configuration[26], [95]. Nitrogen was used as a carrier gas to deliver the precursor vapors from liquid sources to the reactor head, which has parallel gas outlet channels along its bottom surface. The TMA bubbler flow rate was set to 20 SCCM, with a nitrogen carrier flow rate of 105 SCCM. The water bubbler was set to 100 SCCM, with a nitrogen carrier flow rate of 150 SCCM. NH_4OH solution (28% ammonia NH_3 in water) was used as an oxidant to deposit nitrogen-doped AlO_x thin films. The flow through the NH_4OH bubbler was varied as 25, 50, 75 and 100 SCCM, and the corresponding carrier flow was adjusted to 225, 200, 175 and 150 SCCM respectively, so that the total flow into the reactor was kept constant at 250 SCCM. The inert nitrogen gas flow rate was set to 750 SCCM to act as an effective barrier to isolate the flows of the precursors from each other. The deposition conditions are summarized in Table 4.1. The substrate was placed on a heated substrate stage (set to 130 °C) and positioned underneath the reactor head with a small vertical separation distance of 100 μm. The heated stage was oscillated back and forth at the speed of 50 mm/s to expose the substrate to the alternating precursor flows to adsorb a molecular layer, after which the flow of inert gas removes any excess precursor.

4.3 Results and discussions

4.3.1 Thin film characterization

XPS was performed to clarify the chemical composition of 60-nm-thick AlO_x and N-AlO_x thin films deposited using 80 oscillations in 5 minutes (Table 4.1). The atomic percentage of nitrogen was found to vary between 0.08% and 0.68% for the doped films and names were assigned to the different

doping levels (e.g, 0.68N-AlO_x for the film with 0.68% nitrogen). The relatively low atomic percentages of nitrogen are expected because breaking of Al-O bonds by nitrogen atoms is not thermodynamically favored. Furthermore, the low-temperature and atmospheric processing conditions are expected to limit the incorporation of nitrogen, as compared to vacuum-based deposition techniques[142]. The O/Al ratio is seen to vary from 1.81 to 1.27 as the nitrogen-doping increases. The incorporation of nitrogen into the alumina lattice can alter the surface chemistry and result in a decrease in the surface-oxygen concentration, which is readily observed in XPS. Nitrogen can occupy oxygen vacancies or form new nitrogen-aluminum bonds, leading to the formation of Al-O-N bonds and the removal of oxygen atoms from the surface. Moreover, N doping was reported to suppress formation of oxygen-related defects, such as non-lattice oxygen and OH- groups, in AlO_x, which also reduces the surface-oxygen concentration [139]. The carbon content ranged from approximately 21% to 30% and is attributable to adventitious carbon on the film surface and residual carbon from the TMA precursor.

Table 4.1.Deposition conditions and compositions of AlO_x and N-AlO_x thin films, as determined by XPS.

Samples	AP-SALD deposition conditions			Film Composition				
	Water bubbling rate (ml min^{-1})	NH_4OH bubbling rate (ml min^{-1})	Oxidant Carrier gas flow rate (ml min^{-1})	N at%	Al at%	O at%	O/Al	C at%
AlO_x	100	0	150	-	24.89	45.17	1.81	29.93
0.08N-AlO_x	0	25	225	0.08	27.22	44.23	1.62	25.72
0.28N-AlO_x	0	50	200	0.28	32.17	41.83	1.30	25.71
0.57N-AlO_x	0	75	175	0.57	33.16	42.53	1.28	23.73
0.68N-AlO_x	0	100	150	0.68	34.26	43.55	1.27	21.50

The O1s and Al2p XPS spectra of the 60-nm-thick AlO_x and 0.28N-AlO_x are shown in Figure Oa,b and d,e. The O1s and Al2p XPS spectra of the other N-AlO_x films are provided in Figure of (Appendix B) and are similar to those of the 0.28N-AlO_x film. Deconvolution of the O1s peaks by Gaussian fitting in Figure Oa,b revealed peaks at 530.9 and 532.2 eV, which correspond to lattice oxygen (i.e., Al-O) and non-lattice and surface oxygen (e.g., O-H, hydroxyl groups), respectively[142].

The fraction of the O1s signal attributable to these two components was calculated for the AlO_x and N-AlO_x films based on the area under the corresponding XPS peaks and is shown in Figure Oc. The O-H signal can be attributed in part to the water precursor used, consistent with previous reports[136] [142]. It is known that thermal deposition at low temperatures using H_2O as the oxidant usually results in a large amount of O-H groups on the film surface, due to incomplete reaction of the precursors and the high desorption energy of water at low temperatures [143][144]. Notably, the Al-O fraction of the O1s peak is higher for all the N-AlO_x films than for the AlO_x film in Figure Oc and increases with the amount of nitrogen doping. Deconvolution of the Al2p spectra is shown in Figure Od,e. The main peak with a binding energy of 74.3 eV corresponds to the Al-O bond, consistent with the 530.9 eV peak in the O1s spectra (Figure Oa,b) [90]. Another peak with higher binding energy (75.5 eV) was observed which could be assigned to the Al-OH bond[145]. For the 0.28N-AlO_x in Figure Oe, a third peak with small intensity and lower binding energy (73.3 eV) was observed and assigned to the Al-N bond[136]. Figure Of shows the fraction of the Al2p signal attributable to the Al-O, Al-OH, and Al-N bonds as a function of nitrogen-doping level. An increase in the Al-N signal is observed with increasing doping concentration, as expected. The decrease in the amount of Al-OH with increased nitrogen doping in Figure Of is consistent with the decreasing O-H contribution observed for the O1s spectra in Figure Oc.

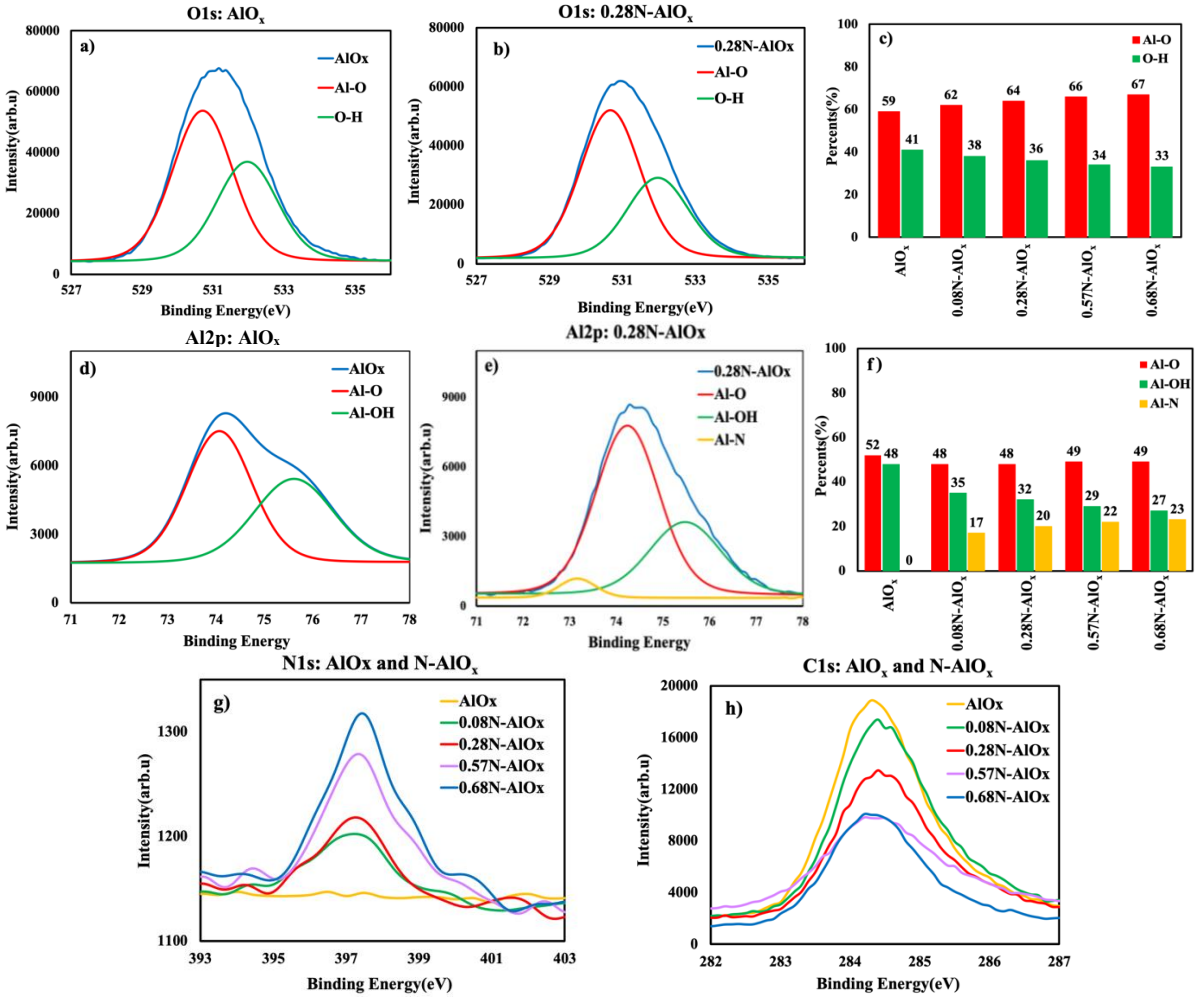

Figure O. O1s XPS spectra of a) AlO_x and b) 0.28N-AlO_x films. c) The fraction of the O1s XPS signal attributable to Al-O and O-H components for AlO_x and N-AlO_x films. Al2p XPS spectra of d) AlO_x and e) 0.28N-AlO_x films. f) The fraction of the Al2p signal attributable to Al-O, Al-OH, and Al-N in AlO_x and N-AlO_x films. g) N1s and h) C1s *XPS spectra of AlO_x and N-AlO_x films.*

The N1s spectra in Figure Og further confirm that nitrogen is incorporated into the N-AlO_x films. The peak located at 397.2 eV is attributed to Al-N bonds [139] and its intensity increased as the NH_4OH flow rate was increased from 25 SCCM (0.08N-AlO_x) to 100 SCCM (0.68N-AlO_x). Figure Oh shows the C1s spectra of the films. The intensity of the C1s peak decreases with nitrogen doping, consistent with the carbon content reported in Table 4.1.

Comparing the Gibbs free energy for the reaction of TMA with water and NH_4OH using thermodynamic data showed that the reaction of TMA with water is slightly more thermodynamically favorable [146][147]. However, it is important to note that other factors, such as reaction kinetics also play a significant role. In general, the reaction kinetics of TMA with water and NH_4OH follow a similar pathway, which includes adsorption of the precursor on the substrate, surface reaction, and desorption of by-products. However, the kinetics of this reaction can be affected by the precursor supply and availability of reactive sites on the substrate surface. The higher vapor pressure of NH_4OH than H_2O (30 times higher at 20 °C)[139] should result in a higher flux of reactive species. This is expected to facilitate the reaction and formation of lattice oxygen [148], consistent with the increasing Al-O signal observed with doping in Figure Oc. This larger flux of reactive NH_4OH species is also consistent with the increasing Al-N signal (Figure Of) and is expected to result in more effective removal of the methyl groups [142], consistent with the reduced C1s signal (Figure Oh).

Therefore, the XPS results showed that the N-doping suppresses the formation of oxygen-related defects, such as residual O-H hydroxyl groups, and reduced the carbon content, which is expected to improve the compactness of the films [139]. A high carbon concentration is undesirable in gas diffusion barrier films, as the carbon provides a penetration pathway [131]. Similarly, oxygen-related defects, including hydroxyl groups, can provide a permeation pathway in AlO_x [135][76]. Thus, the N-doping may be expected to improve the barrier properties of the encapsulation layer.

In order to study the uniformity, compactness and roughness of the thin films, ellipsometry, SEM and AFM were conducted on the AlO_x and N-AlO_x thin films. Figure Pa,b shows photographic images of AlO_x and 0.28N-AlO_x films deposited on a silicon substrate using 120 substrate oscillations. Both films are uniform and the same uniformity was observed for all doping levels (Figure in Appendix B). SEM images of the AlO_x and 0.28N-AlO_x films in Figure Pc,d confirmed the pinhole- and crack-free nature of the thin films, indicating a high uniformity well-suited for TFE. SEM images for all

doping levels are shown in Figure and show similarly high uniformity. Figure Pc shows some randomly distributed particles on the surface of the AlO_x thin film, which could result from gradual powder formation on the underside of the AP-SALD reactor head, indicating that some mixing of the precursors in the gas phase may have occurred, which is discussed further below. Ellipsometry thickness maps are presented in Figure P e,f for the AlO_x and 0.28N-AlO_x films. The variation of thickness is very low over areas of approximately 20 × 20 cm^2.

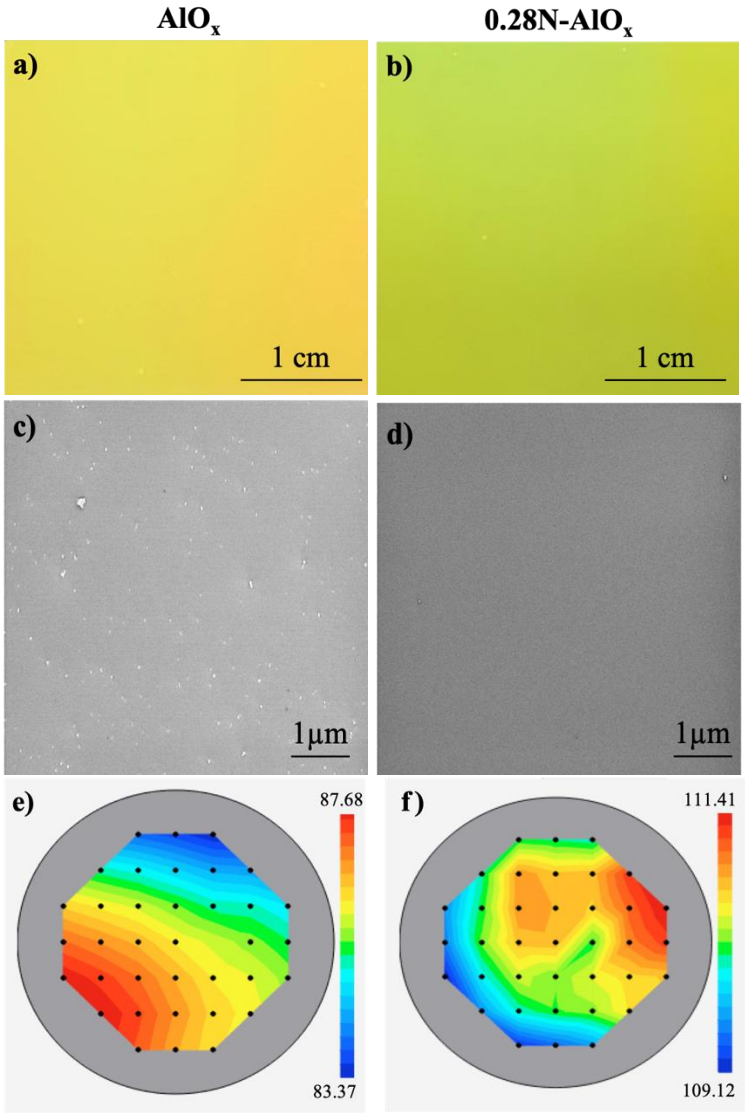

Figure P. Uniform, pinhole-free AP-SALD films deposited on Si wafers using 120 substrate oscillations. Photographic images of a) AlO_x and b) 0.28N-AlO_x. SEM images of c) AlO_x and d) 0.28N-AlO_x. Ellipsometry thickness distribution maps (in nm) of e) AlO_x and f) 0.28N-AlO_x in 20 × 20 cm^2 area.

By plotting the film thickness as a function of the number of AP-SALD oscillations (Figure Qa), the growth oscillations per cycle (GPC) was obtained for each doping level. One AP-SALD oscillation is equivalent to two conventional-ALD precursor-reactant cycles as the substrate oscillates back and forth under the reactor. Linear trends are observed for all doping levels, indicating a constant GPC. A growth of 0.66 nm/oscillation is determined for pristine AlO_x, which is equivalent to 0.33 nm/cycle. GPCs of 0.11-0.14 nm/cycle are typically reported in literature for alumina films grown by spatial ALD using similar process conditions[107][149]. The higher GPCs observed here suggest that atmospheric-pressure spatial chemical vapor deposition (AP-SCVD) likely occurred due to some precursor mixing in the gas phase, i.e., the gas flow rates and reactor-substrate spacing were such that the TMA and water/NH_4OH precursors were not perfectly isolated by the inert N_2 gas. AP-SCVD conditions are attractive for device manufacturing, since higher deposition rates are obtained, while still producing smooth, pinhole-free, conformal films with thicknesses proportional to the number of cycles[88]. It was previously shown that AP-SCVD deposition was obtained using a reactor-substrate spacing of 50 μm and different flow rates for the metal and oxidant precursors[100]. In this work, an even larger reactor-substrate spacing of 100 μm was used to ensure some mixing of the precursors in the gas phase above the substrate. The GPC of 0.33 nm/cycle for the undoped AlO_x films indicates that approximately 2 to 3 monolayers were deposited each cycle.

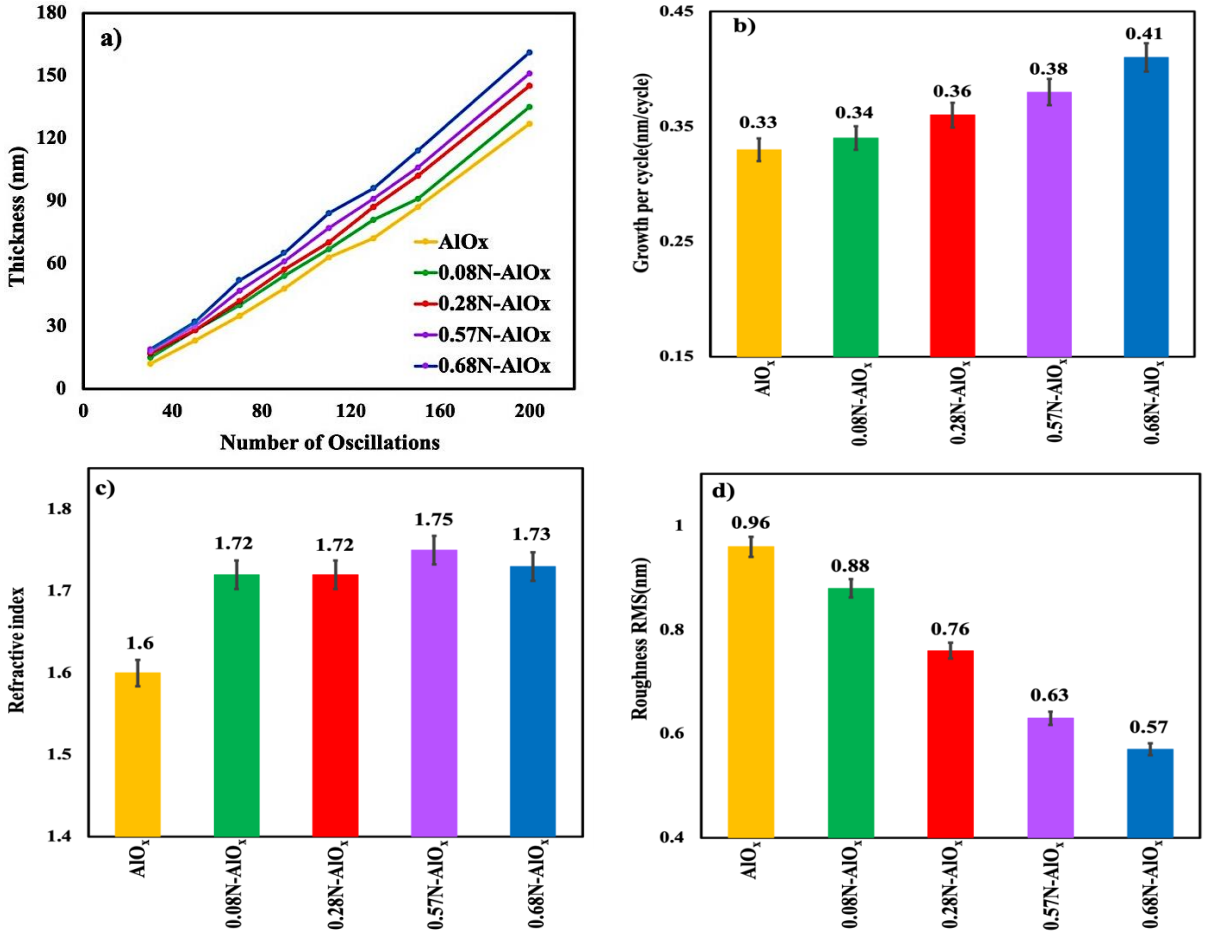

Figure Q. a) Film thickness as a function of the number of AP-SALD oscillations for different nitrogen-doping levels on silicon substrates. b) GPCs, c) refractive indices, and d) surface roughness for different nitrogen-doping levels. (Refractive indices and surface roughness were measured for 60 nm thick films deposited using AP-SALD on silicon substrates.)

The GPC was observed to increase with nitrogen doping, with values between approximately 0.34-0.41 nm/cycle for different N-AlO_x compositions, as shown in Figure Qb. This is consistent with the XPS results that indicated that the higher vapor pressure of NH_4OH facilitates a greater flux of reactive species and more complete surface reactions. Furthermore, the nitrogen ion (1.40 Å) is 0.08 Å larger than the oxygen ion (1.32 Å) such that N-AlO_x films are expected to be thicker than AlO_x films for otherwise identical growth conditions [150].

The refractive indices were measured by ellipsometry to be 1.60 for the AlO_x and 1.72–1.75 for the N-AlO_x, as shown in Figure Qc. These matched well with the 1.53–1.78 range reported previously for Al_2O_3 [90]. The N-AlOx thin films showed higher refractive indices than AlO_x, indicating an improved film compactness/density[151]. This is consistent with the lower O-H and carbon contents of the N-AlO_x films observed by XPS (Figure O).

Surface roughness is another critical coating characteristic that should be minimized for high-quality encapsulation layers[14]. The roughness of the films with different nitrogen-doping levels is shown in Figure Qd. The surface of all the N-AlO_x films are smooth with root-mean square (RMS) roughness between 0.57 nm and 0.88 nm, slightly smaller than that of the AlO_x thin (0.96 nm). A reduction in surface roughness has previously been reported for nitrogen-doped ALD films and is attributed here to the substitution of larger N^{3-} ions for O^{2-} during the deposition and/or reduction of oxygen related defects (such as surface and non-lattice oxygen)[152][153]. The compact, smooth nature of these films make them good candidates for gas-diffusion barriers [154].

4.3.2 Water vapor transmission rate measurements

AlO_x and N-AlO_x films with thicknesses of 60 nm (confirmed by ellipsometry) were deposited directly on top of thermally evaporated Ca films in approximately 4 minutes. The Ca films are initially metallic and opaque. Then, the encapsulated Ca films were exposed to ISOS-D-1 testing conditions[134] (25˚C-55%RH). Transmission of water through the encapsulation films results in oxidation of the Ca to calcium hydroxide, which makes the film transparent. The oxidation area of the Ca films was monitored by photographic imaging to determine the WVTR of the TFE using a method reported previously[130] as well as identifying the location of defects in the encapsulation layers.

Pictures of the Ca films encapsulated with the AlO_x and different N-AlO_x thin films are shown in Figure Ra-e after different testing durations. A red background was used to allow the oxidation and

hence the defects and weak spots in the encapsulation layer to be directly visualized. The image of the Ca film encapsulated with a 60 nm AlO_x TFE in Figure Ra showed the presence of a few circular spots on the Ca film after 3 h, which are identified as oxidized regions. After 7 h, these circular spots have grown and a few additional new small circular spots are noticeable. These images clearly indicate that these oxidized Ca regions are circular areas that grow radially in size with time. This behavior suggests the existence of some pinhole defects in the AlO_x coating, which are likely caused by particles on the initial Ca film[155]. Particles are expected to mask the underlying Ca film from AlO_x encapsulation and provide a permeation path for water [156], as shown schematically in Figure Sa. Also, the appearance of new oxidization area may be due to water traveling through hydroxyl defects in the AlO_x TFE[76]. In other words, these defects are caused by water corrosion of the AlO_x film[157]. Defects caused by water corrosion were described previously in a study of H_2O permeation in Al_2O_3 ALD films of different thicknesses grown at different temperatures[158]. The study proposed that water-vapor permeation does not rely on pinholes in ALD films, which we contend are pinhole free. Instead, it occurs by H_2O permeating along chains of chemical defect clusters like OH- defect as shown in Figure Sb[158]. We believe that these percolation paths do not exist initially at early time. These percolation paths are formed progressively with time resulting from H_2O corrosion of the AlO_x film[158]. The circular spots continue to grow and then merge together. After 42 h, the photographic image in Figure Ra showed the nearly complete oxidation of the Ca film. The reaction of water with Ca metal to form calcium hydroxide ($Ca(OH)_2$) results in a 27% increase in volume. Calcium hydroxide can also readily react with CO_2 to form calcium carbonate ($CaCO_3$). This reaction results in a further increase in volume to a total of 31% (aragonite) or 42% (calcite) above the original Ca volume[129]. This expansion may crack the TFE and degrade its barrier properties at later time. As shown in Figure R b-e, the N-AlO_x thin-film encapsulation layers showed a similar oxidation pattern but at later times, indicating that the permeation rate for water molecules through the N-AlO_x TFE was lower than for the AlO_x TFE. It was previously reported that the probability that a percolation pathway exists will increase as the OH- defect

concentration increases[76]. Our XPS results showed that by introducing N into N-AlO_x, the OH- defect concentration was decreased. Therefore, the N-AlO_x films enter the blooming phase slower than the AlO_x film, indicating lower WVTR values.

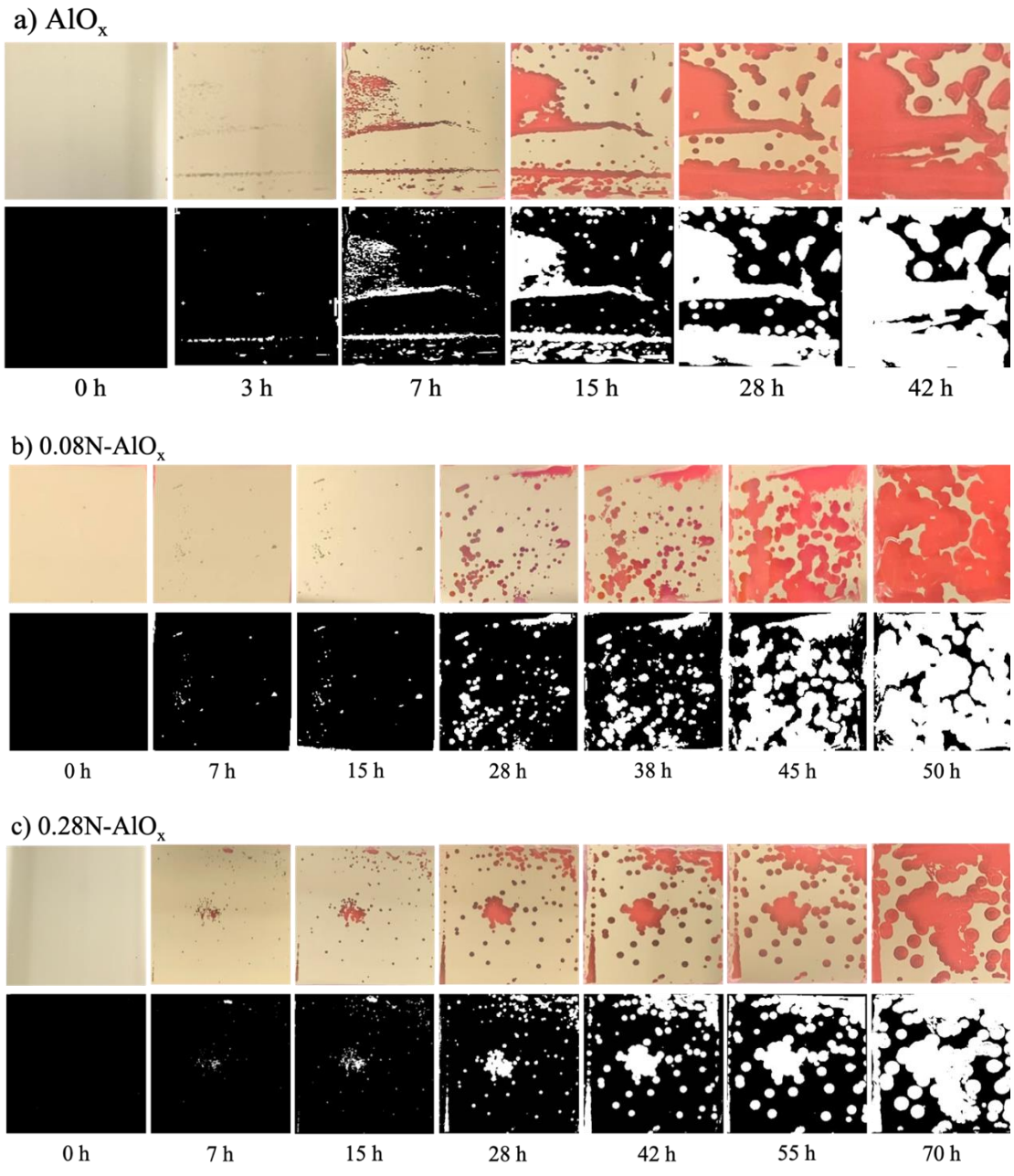

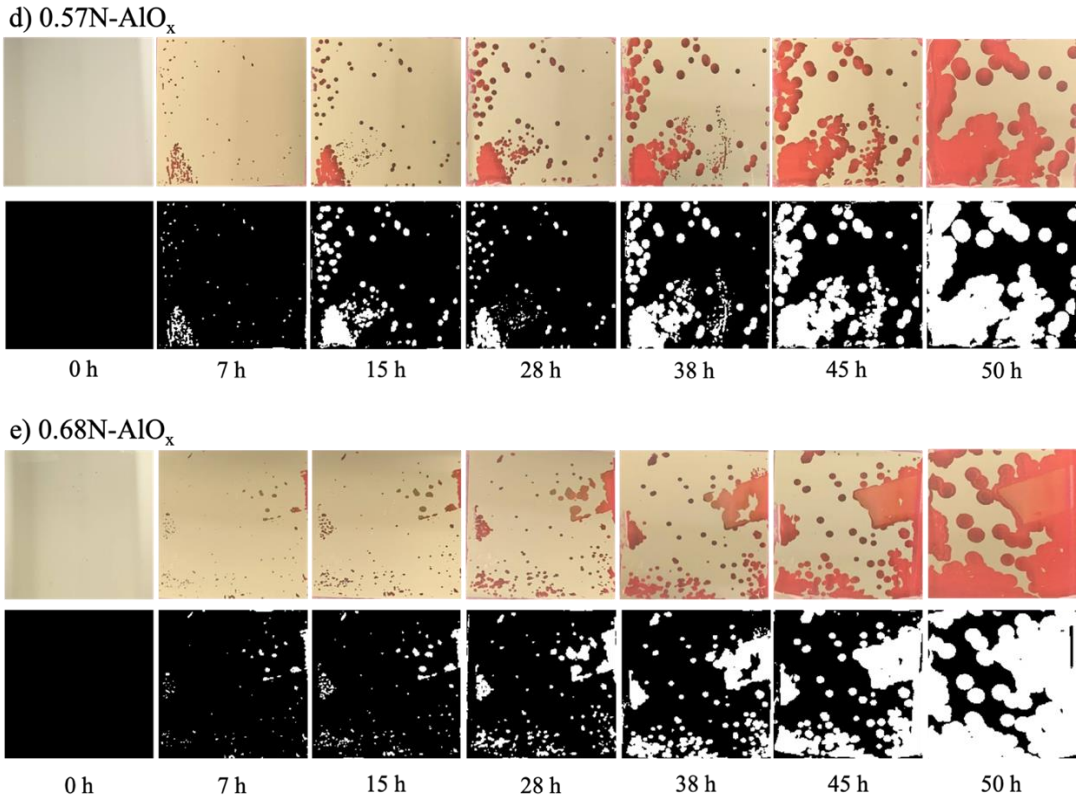

Figure R. Real pictures and high contrast black-and-white images of 1.8cm×1.8cm Ca films encapsulated with a) AlO_x, b) 0.08N-AlO_x, c) 0.28N-AlO_x, d) 0.57N-AlO_x, and e) 0.68N-AlO_x barrier films with a thickness of 60 nm after storage in ISOS-D-1(25˚C-55% RH) conditions for increasing time intervals.

The WVTR values were obtained by analyzing the oxidized area of the Ca films as explained in the experimental chapter. The images were first converted into black-and-white images (Figure R) where the white areas correspond to oxidized Ca. The WVTR values of the different TFE are summarized in Table 4.2

Table 4.2. WVTR values for the 60-nm-thick TFE deposited with AP-SALD at ISOS-D-1 (25˚C-55% RH) and ISOS-D-3 (65˚C-85% RH).

TFE	WVTR (g/m^2/day) ISOS-D-1(25˚C-55% RH)	WVTR (g/m^2/day) ISOS-D-3(65˚C-85% RH)
AlO_x	6.5×10^{-5}	7.8×10^{-4}
0.08N-AlO_x	2.7×10^{-5}	7.1×10^{-4}
0.28N-AlO_x	1.34×10^{-5}	5.7×10^{-4}
0.57N-AlO_x	3.8×10^{-5}	6.3×10^{-4}
0.68N-AlO_x	4.4×10^{-5}	5.9×10^{-4}

WVTR values on the order of 10^{-5} g/m^2/day and 10^{-4} g/m^2/day were measured at 25˚C-55% RH and 65˚C-85% RH, respectively. Attempts to compare the reported WVTR values is not easy because most of the Ca test studies have not been described in detail. In addition, many of the assumptions of the oxidation area methods have not been clearly defined or verified by these studies[126]. Furthermore, the wide range of temperatures and relative humidity used to measure the WVTR values make it impossible to compare WVTR values from Ca test results[134]. Nonetheless, the WVTR values in Table 4.2 indicate that all of the films are good barriers to water-vapor permeation. The N-AlO_x TFE consistently showed lower WVTR values compared to the undoped AlO_x. It is also seen in Table 4.2 that the WVTR values decrease by increasing the N concentration up to 0.28% but that adding more nitrogen (0.57% or 0.68%) increased the WVTR slightly. Water-vapor transmission depends on the nature of defects and pinholes, surface morphology, and chemical interactions between water molecules and surface species[159]. Water molecules arriving on the top surface take energetically favorable permeation pathways including micron-scale defects and smaller tortuous pathways as shown in Figure S. The absence of pinholes on the surface of the AlO_x and N-AlO_x, as revealed by SEM in Figure Pc,d, suggests that the water-vapor diffusion through the TFE was not controlled by micron-scale defects. Instead, the AlO_x and N-AlO_x films are expected to contain nanoscale tortuous pathways that are probably of central importance in controlling WVTR values. With this in mind, the lower WVTRs observed for the N-AlO_x films are consistent with the higher refractive indices that indicated these films are more compact than the AlO_x. The interaction of water molecules with surface species is also expected to contribute to the permeation mechanism, especially if the primary transport mechanism is through a percolation permeation pathway. Thus, in order to understand the effect of the nitrogen doping on the WVTR values, we need to consider the role of available interaction sites in N-AlO_x films. The XPS results (Figure Og) confirmed the incorporation of nitrogen atoms into the alumina lattice, either by replacing oxygen atoms, or by occupying interstitial sites. These nitrogen defects can act as energy wells, which can trap water molecules and delay their permeation through the thin film.

However, excess nitrogen may be expected to facilitate water permeation through a percolation pathway. A high concentration of trapping sites may lead to multilayer absorption of water, resulting in surface diffusion or capillary condensation between pore walls (Figure Sc), which increases water vapor permeation and WVTR values [159]. It was shown in other studies that immediately after deposition, the AlO_xN_y surface is more hydrophilic than AlO_x[159], further suggesting that nitrogen may facilitate vapor penetration in the N-AlO_x thin films. Once water molecules reach the tortuous pathways, they can interact strongly with the more hydrophilic pore walls (i.e., those with nitrogen defect sites), causing some water molecules to dissociate and oxygen to become trapped locally. The noninteracting hydrogen species would then need to re-form into water molecules to complete the permeation process. This may be facilitated by simultaneous permeation of oxygen gas [159]. Thus, while further study of the permeation mechanisms is warranted, the evidence presented here suggests that nitrogen doping of the TFE improves their barrier properties by increasing the compactness of the films (reducing the size and/or number of nanoscale permeation pathways) but that the nitrogen defects may facilitate permeation through these pathways as their concentration increases.

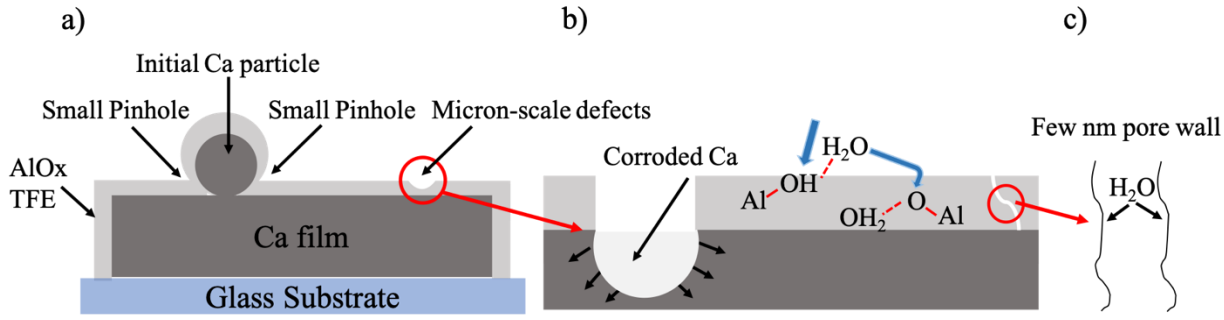

Figure S. Schematic of a) pinholes and micron scale defects on AlO_x thin-film encapsulation, b) Ca corrosion and the percolation paths formed progressively with time resulting from H_2O permeating along chains of chemical defect clusters like OH- defects, c) surface diffusion of water through pore walls.

4.3.3 PSCs characterization and stability tests

To assess whether deposition of the TFE causes any damage to the light-absorbing perovskite layer, a 60-nm 0.28N-AlO_x TFE was deposited directly on a 200 nm formamidinium methylammonium lead iodide ($FA_{0.92}MA_{0.08}PbI_3$) perovskite film using 80 AP-SALD oscillations in only 4 minutes. Ellipsometry was used to ensure the 60-nm thickness. Figure Ta shows the XRD patterns of the perovskite film before and after deposition of the 0.28N-AlO_x TFE. The pattern is unchanged, demonstrating that negligible change occurs to the perovskite during the rapid deposition of the TFE at 130 °C. Typical peaks at 14.10°, 23.47°, 28.42°, and 30.89° corresponding to the (110), (202), (220), and (222) planes of the tetragonal perovskite phase are present in both cases[119]. No impurity phases, neither pure PbI_2 nor FAI tetragonal phase are detected, indicating a high level of phase purity.

To examine whether the AP-SCVD process influences the PSC performance, 60-nm-thick 0.28N-AlO_x TFE were then deposited on PSCs using 80 AP-SALD oscillations in only 4 minutes. In order to identify any effect of the PSC configuration on the performance of the TFE, PSCs with 2 different structures were fabricated: a n-i-p structure consisting of FTO/SnO_2/$FA_{0.92}MA_{0.08}PbI_3$/spiro-OMeTAD/Ag, as well as a p-i-n structure consisting of FTO/PTAA/$FA_{0.92}MA_{0.08}PbI_3$/$PC_{61}BM$/BCP/Ag, as illustrated in Figure Ma,b.

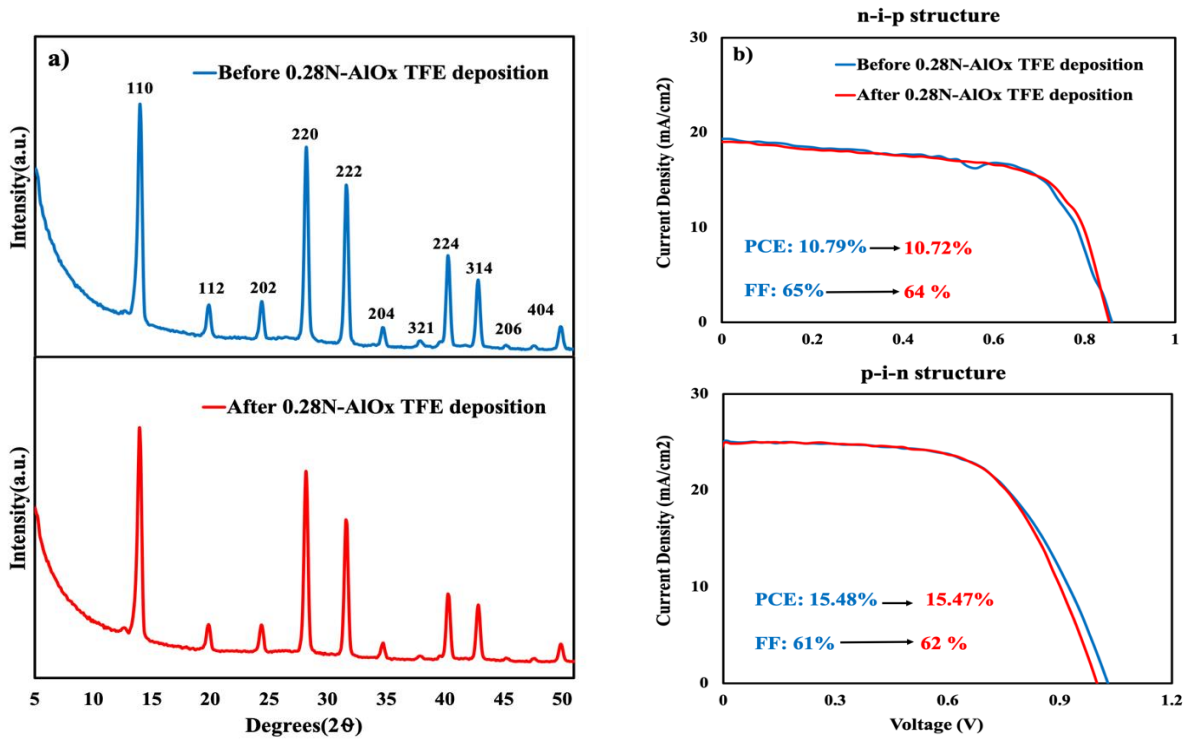

Figure T. a) X-ray diffraction (XRD) patterns of perovskite layer, b) J–V characteristics of n-i-p structure and p-i-n structure PSCs before and after deposition of 60 nm 0.28N-AlO_x TFE.

The current-density/voltage (J–V) curves measured under simulated solar illumination in air for the p-i-n and n-i-p solar cells before and after deposition of the 60-nm 0.28N-AlO_x TFE are shown in Figure Tb. The PCEs and fill factors (FF) of the PSCs are listed inside Figure Tb. The J-V curves are nearly identical, indicating that the deposition of the TFE had no obvious effect on the performance of the solar cells. Even the n-i-p PSC with Spiro-OMeTAD exhibited no degradation during the AP-SCVD process at 130˚C. The $FA_{0.92}MA_{0.08}PbI_3$ perovskite layer used in this study, is expected to be unstable above approximately 150˚C[119] and most PSCs suffer from thermal stress at high temperatures due to the poor thermal stability of the organic small-molecule-based hole-transporting materials, including Spiro-OMeTAD and additives[52]. Hence the slow deposition rate of conventional ALD has limited its use for the deposition of TFE on PSCs due to the need for prolonged heating at ALD reaction temperatures. In contrast, the much shorter AP-SCVD times used in this work allow

higher deposition temperatures (e.g., 130°C), which lead to dense, conformal and uniform oxide films[19].

To study the performance of the TFE developed in this work, n-i-p and p-i-n PSCs were coated with 60 nm of AlO_x or N-AlO_x with different nitrogen concentrations and the PSC performance was then monitored over extended periods under two different environmental test conditions; ISOS-D-1 (dark, 25˚C-55%RH) and ISOS-D-3 (dark, 65˚C-85% RH)[134]. Control cells without an encapsulation layer were also exposed to accelerated test conditions. At least two PSCs were tested in each condition to ensure data reproducibility. Figure Ua,b presents the normalized PCEs as a function of time for the two device architectures under ISOS-D-3 (65˚C-85% RH) conditions. Similar figures for the ISOS-D-1 conditions are included in the Appendix B(Figure), but the results are summarized in terms of T_{80} values in Figure Uc,d.

It can be seen in Figure Ua,b that the stability of the devices increased markedly by applying an encapsulation layer. For example, the n-i-p device without encapsulation in Figure Ua degraded to 80% of its original efficiency in 35 h (T_{80}= 35 h)[134], which is attributed due to the rapid permeation of moisture into the devices leading to accelerated decomposition of the perovskite layer and degradation of its interface with charge transport layers[69]. In contrast, all encapsulated n-i-p PSCs in Figure Ua displayed T_{80} values greater than 98 h. Similarly, the p-i-n PSCs in Figure Ub showed a T_{80}= 53 h without encapsulation and T_{80} values greater than 180 h with encapsulation. The AlO_x and N-AlO_x TFE act as a first barrier, slowing down the ingress of H_2O and oxygen from the ambient and the egress of volatile species from the device. This blocking of decomposed volatile components has been reported to causing saturation of the gaseous decomposed components inside the cells, which hinders the decomposition process[6].

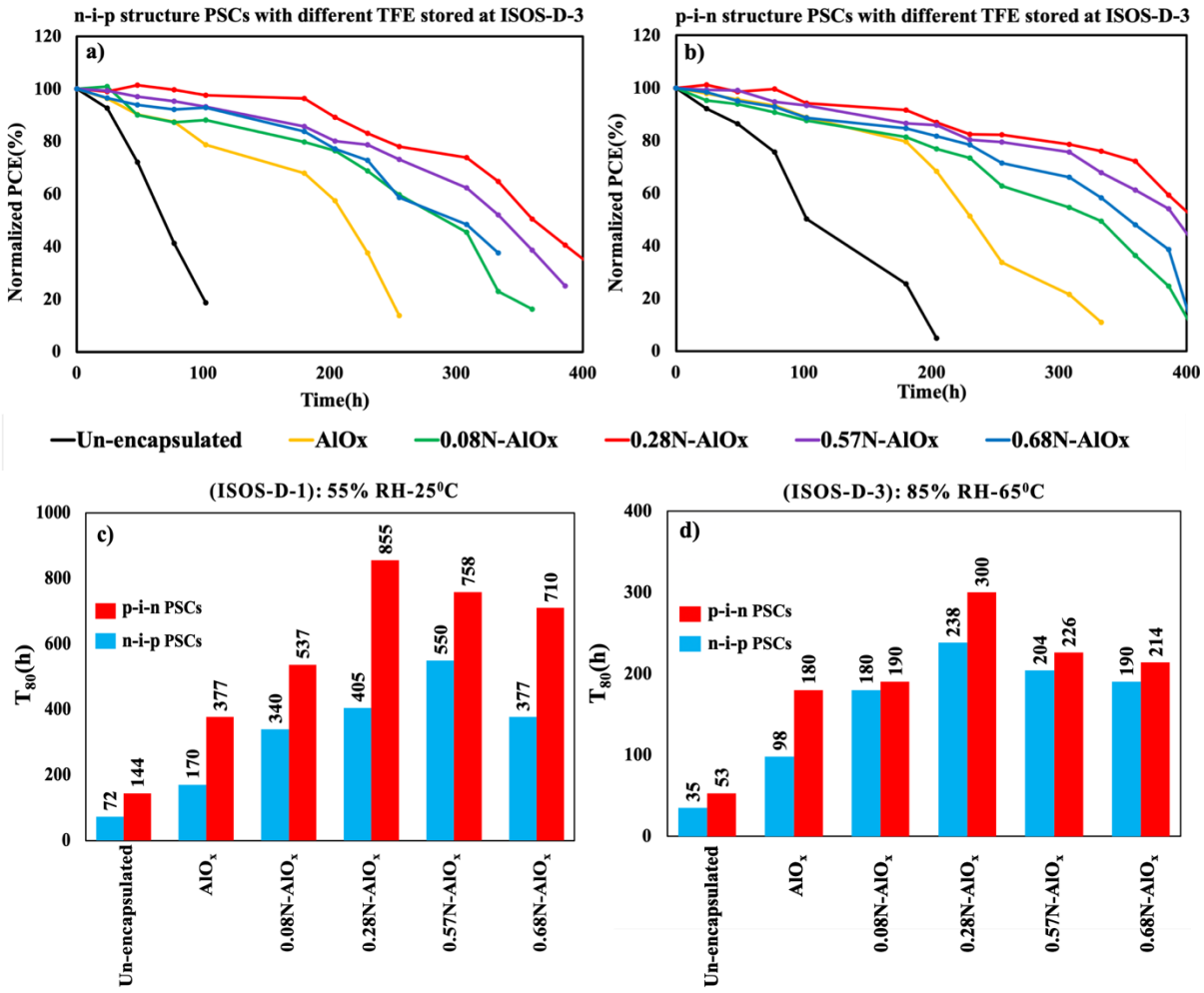

Figure U. Normalized PCE versus time for a) n-i-p and b) p-i-n PSCs encapsulated with different thin film encapsulation kept at ISOS-D-3 (65°C-85%RH). The PCE values were normalized to their initial PCE value. The T_{80} values of the p-i-n and n-i-p PSCs with different thin film encapsulation in c) ISOS-D-1 and d) ISOS-D-3 conditions.

Figure Uc and d show the T_{80} values of the p-i-n (red) and n-i-p (blue) PSCs with the various TFE for the ISOS-D-1 and ISOS-D-3 conditions, respectively. As expected, the T_{80} values are higher for the ISOS-D-1 conditions (25°C-55%RH) than the ISOS-D-3 conditions (65°C, 58%RH), as the diffusivity of water vapour through the encapsulation obeys Fick's law and hence is related to the humidity level and temperature. It is observed that the devices with N-AlO_x TFE showed better stability than those with AlO_x TFE, consistent with the lower WVTR values. The p-i-n PSCs with AlO_x TFE,

for example, showed T_{80} values of 377 hrs and 180 hrs in ISOS-D-1 and ISOS-D-3 condition, respectively, whereas the p-i-n PSC with the 0.28N-AlO_x TFE showed T_{80} values of 855 hrs (ISOS-D-1) and 300 hrs (ISOS-D-3). It is seen in Figure Uc,d that the optimal nitrogen concentration is around 0.28%, consistent with the lowest WVTR values reported in Table 4.2. The N-doping improves the film compactness and the nitrogen defects may trap water molecules and hinder their diffusion; however, higher nitrogen concentrations facilitate permeation, possibly due to multilayer adsorption of water driven by the high concentration of trapping sites[159]. Therefore, the key requirement to produce a better barrier layer is to increase the density and compactness of the coatings as much as possible and reduce the number of water diffusion pathways by optimizing the N concentration.

It is seen in Figure Uc,d that the p-i-n devices (red) are more stable than the n-i-p devices (blue), regardless of the encapsulation. The T_{80} value is almost 2 and 1.5 times longer for the un-encapsulated p-i-n PSCs stored in ISOS-D-1 and ISOS-D-3 conditions, respectively. The perovskite's rate of degradation is strongly linked to the humidity level as well as the type of layer placed on top of the perovskite. It was pointed out by several studies that the HTL (in n-i-p structure) and ETL (in p-i-n structure) are able to hinder moisture ingress toward the perovskite layers underneath [160]. In our study, doped-spiro-MeOTAD (HTL) and $PC_{16}BM$/PCB (ETL) covered the perovskite in the n-i-p and p-i-n structures, respectively. Stability issues in n-i-p PSCs are frequently linked to the poor stability of the spiro-MeOTAD, which may suffer from cracking during the fabrication process [161]. This would expose the perovskite and device degradation may be accelerated. It was also shown that exposure to moisture and applying thermal stress made pinholes in the spiro-OMeTAD layer, which could promote moisture ingress into the perovskite layer and lead to rapid degradation[55]. Here, the generally hydrophobic nature of the top electron transporting layer (PCBM) would seem to be beneficial for preventing moisture ingress, even under the accelerated conditions of ISOS-D-3 (65°C-85%RH), as shown in Figure Ud.

A summary of previous reports on TFEs can be found in Table 2.2, highlighting the perovskite device structure, encapsulation materials and the stability performance. Although it is difficult to directly compare available results due to the inconsistency in testing conditions used and parameters reported, it is seen that the WVTR values measured for the N-doped TFE (e.g., 1.34×10^{-5} g/m^2/day in ISOS-D-1 conditions for the 0.28N-AlO_x) are similar or less than previous reports and THE T_{80} values (e.g., 855 hr in ISOS-D-1 conditions for the 0.28N-AlO_x) are also very promising.

Chapter 5

Zn-doped Alumina TFE Layers

5.1 Introduction

Alumina has a relatively low WVTR, good adhesion and high mechanical strength, making it a superior TFE layer which is commonly used to enhance device stability under moisture exposure[65][162]. The disadvantage of Al_2O_3 is its corrosion in the presence of water[14]. Therefore, many efforts have been made to incorporate other materials to enhance the barrier performance of ALD Al_2O_3. Recently, multicomponent oxides have found an increasing number of industrial applications since varying the film stoichiometry allows the control of their physical properties, including refractive index, surface roughness, and conductivity over a wide range[109]. Doped oxides are also the most common family of ALD-grown multicomponent materials. The basic purpose of doping is to tune the material properties (optical, electrical, and structural) to optimize the film for a specific application[110]. Zn-doped Al_2O_3 thin films are an attractive TFE for PSCs with promising barrier properties, because ZnO is more corrosion resistant and has higher density than Al_2O_3[163]. Therefore, introducing Zn into amorphous Al_2O_3 thin films could increase film density and consequently enhance the gas diffusion barrier. The conventional way to prepare Zn-doped Al_2O_3 thin films by ALD is to use a super-cycle approach, where an extra cycle of ZnO is regularly added after several cycles of AlO_x based on the required Zn doping level[164]. Although the water permeability of the bilayer and multilayer films of Al_2O_3/ZnO made by ALD is much lower than that of either single-layer Al_2O_3 or ZnO[165], the dopant distribution and the properties of the ZnO/Al_2O_3 layered structure tend to be inhomogeneous in the direction of thickness [166]. Efforts have been made to improve the homogeneity, such as using the co-dosing ALD process, where TMA and diethylzinc (DEZ) were co-introduced into the deposition zone, and the input carrier flow rate ratio of the precursors was varied to

obtain different doping levels[116]. However, mixed Al_2O_3 and ZnO films with promising barrier properties have mostly been fabricated by ALD. Therefore, in order to fulfill the industrial need for uniform, pinhole-free, and highly conformal multicomponent thin films on large-area and flexible substrates, there is a strong motivation to expand the capabilities of spatial ALD to a wider range of materials and to explore new functionalities and applications of complex oxides[110]. To-date, all applications of spatial ALD to PSCs have been mostly limited to single-component oxide films, mainly for charge-transport layers[167][168][169].

In this work, the barrier properties of Zn-doped AlO_x thin films deposited using an AP-SALD system are investigated. For this purpose, TMA and DEZ metal precursors are concurrently introduced into the deposition region, and the Zn content of the deposited films is controlled by the flow rate of the DEZ bubbler. The Zn-AlO_x thin-film structure and deposition conditions were optimized to minimize the WVTR value and maximize the long-term stability of PSCs by improving the gas diffusion barrier properties of the TFE. The Zn-AlO_x thin films show an outstanding barrier property at an accelerated testing condition of 65˚C-85% RH (ISOS-D-3). We believe that this study can prompt further improvement in the PSC lifetime, which is pivotally important for commercialization of PSCs in the near future.

5.2 Experimental

Al_2O_3 and Zn-AlO_x layers were deposited in open-air conditions using our custom-built, dual AP-SALD/SCVD system, which employs a close-proximity reactor-head configuration [26][95]. The amount of zinc was controlled by varying the DEZ flow rate between 10 and 25 SCCM as shown in Table 5.1. The TMA bubbler flow rate was set to 25 SCCM. The flows from the DEZ and TMA bubblers were mixed and co-injected in the deposition zone through the same inlet after being diluted by nitrogen, as shown in Figure V, to produce a homogeneous distribution of dopant throughout the

Al_2O_3 film. The substrate was placed on a heated substrate stage (set to 130 °C) and positioned underneath the reactor head with a small vertical separation distance of 100 µm. The heated stage was oscillated back and forth at the speed of 50 mm/s to expose the substrate sequentially to the alternating precursor flows.

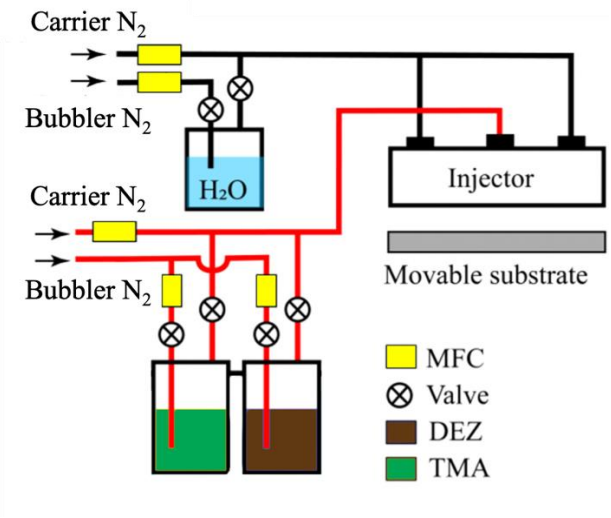

Figure V. Scheme of the simultaneously injected metal precursor in AP-SALD system.

5.3 Results and discussions

5.3.1 Thin film characterization

The composition of Al_2O_3 and Zn-AlO_x films deposited using 120 oscillations in 5 minutes (Table 5.1) was determined by studying O1s, Al2p, Zn2p3/2 and Zn2p1/2 electron binding energies using XPS. Zn, Al, O, and C atomic percentages as well as induced defects in the Al_2O_3 and Zn-AlO_x thin films were analyzed.

Table 5.1. compositions of Al_2O_3 and Zn-AlO_x thin films, as determined by x-ray photoelectron spectroscopy.

Samples	AP-SALD Conditions			Film Composition					
	DEZ precursor bubbling rate (SCCM)	TMA precursor bubbling rate (SCCM)	Metal carrier gas flow rate (SCCM)	Zn at%	Al at%	O at%	C at%	O/Al	Zn/Al
Al_2O_3	-	25	100	0	28.33	42.61	29.06	1.50	0
0.07Zn-AlO_x	10	25	90	1.95	27.67	42.09	28.29	1.52	0.07
0.10Zn-AlO_x	15	25	85	2.59	26.79	41.98	28.63	1.56	0.10
0.21Zn-AlO_x	20	25	80	5.38	25.19	41.71	27.72	1.65	0.21
0.29Zn-AlO_x	25	25	75	6.86	23.25	41.57	28.32	1.78	0.29

Increasing the DEZ flow rate from 10 to 25 SCCM increased the Zn atomic percentage from 1.95 to 6.86 %, while the Al atomic percentage decreased from 28.33 to 23.25 %. This is attributed to Zn atoms replacing Al atoms in the lattice sites of alumina. It is expected that a wider doping range can be obtained by using a larger range of DEZ flow rates.

The carbon content was found to be similar for all doping levels (29.06% to 28.3%) and is attributable to adventitious carbon on the film surface and residual carbon from the precursors.

The O/Al ratio was seen to vary from alumina's typical ratio of 1.5 to 1.78 as the zinc doping increased. This was expected as Al atoms were replaced by Zn atoms. Additionally, Zn doping may suppress the formation of oxygen-related defects in AlO_x, such as non-lattice oxygen and OH- groups, which may affect the O/Al ratio.

The Zn/Al ratio was found to vary between 0.07 and 0.29 for the doped films when the DEZ flow rate increased from 10 to 25 SCCM and names were assigned to the different doping levels (e.g,, 0.29Zn-AlO_x for the film with 0.29 Zn/Al). A sharp increase in the Zn/Al ratio from 0.10 to 0.21 was found when increasing the DEZ flow rate from 15 to 20 SCCM at a constant TMA flow of 25 SCCM. Because DEZ and TMA vapors are co-injected continuously in the same deposition region, the reaction

steps between surface hydroxyl groups and the two metal precursors can occur simultaneously, producing both $Zn(C_2H_5)$ and $Al(CH_3)_2$ surface species[115]. In addition to a competitive adsorption of TMA and DEZ at surface hydroxyl groups, TMA molecules can also etch the chemisorbed DEZ, possibly via a CH_3 ligand-exchange reaction. Etching of DEZ by TMA exposure has been observed previously during the deposition of Al_2O_3/ZnO nanolaminates by conventional ALD[170]. The Zn content in the Al_2O_3/ZnO nanolaminates was reported to be significantly below the expected values[170]. It has been proposed that etching of Zn by TMA occurs because of the larger formation enthalpy of Al_2O_3 (−845 kJ/mol Al atoms) compared to ZnO (−353 kJ/mol Zn atoms)[171]. Under these conditions, the $Zn(C_2H_5)$ surface species act partially as a sacrificial layer[110]. Hence at the lower DEZ flow rate of 15 SCCM, a significant portion of the DEZ may be etched, resulting in the Zn/Al ratio of 0.10, whereas much of the additional DEZ supplied at a flow rate of 20 SCCM may end up in the film, resulting in a jump in the Zn/Al ratio to 0.21.

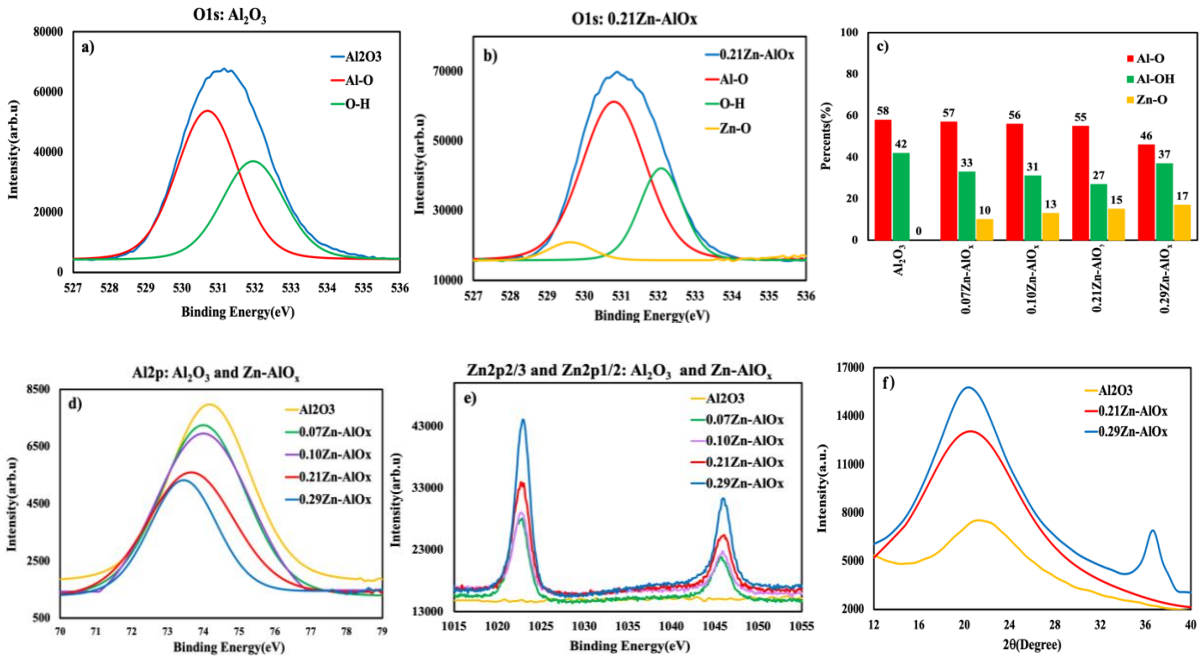

Figure W. O1s XPS spectra of a) Al_2O_3 and b) 0.21Zn-AlO_x films. c) The fraction of the O1s XPS signal attributable to Al-O, Al-OH and Zn-O components for Al_2O_3 and Zn-AlO_x films. d) Al2p, e) Zn2p2/3 and Zn2p½ spectra of Al_2O_3 and Zn-AlO_x films. f) Grazing incidence XR) patterns of Al_2O_3, 0.21Zn-AlO_x and 0.29Zn-AlO_x films deposited on silicon substrate using 200 oscillations.

By studying the O1s spectra, the variation of non-lattice oxygen can be monitored as a function of dopant concentration. The O1s spectra of the 60-nm-thick Al_2O_3 and 0.21Zn-AlO_x are shown in Figure Wa,b. The O1s spectra of the other Zn-AlO_x films are provided in Figure of Appendix C and are similar to those of the 0.21Zn-AlO_x film. Deconvolution of the O1s peak of a Al_2O_3 film by Gaussian fitting in Figure Wa revealed peaks at 530.9 and 532.2 eV, which correspond to lattice oxygen (i.e., Al-O) and non-lattice and surface oxygen (e.g., O-H, hydroxyl groups), respectively[142]. The non-lattice and surface oxygen may be attributed to the deposition at low temperatures using H_2O as the oxidant and incomplete reaction of the precursors consistent with previous reports[136], [142] [143][144]. Deconvolution of the O1s spectrum of a 0.21Zn-AlO_x film in Figure Wb revealed the same peaks at 530.9, and 532.2 eV, as well as a peak centered at 529.6 eV, which is associated with O^{2-} surrounded by Zn^{2+} in the full oxidation states (Zn-O lattice oxygen)[96].

The fraction of the O1s signal attributable to these three components was calculated for the Al_2O_3 and Zn-AlO_x films based on the area under the corresponding XPS peaks and is shown Figure Wc. Increasing the Zn/Al ratio up to 0.21 leads to a decrease of the O-H fraction, indicating a decrease in non-lattice oxygen. A subsequent increase in the Zn flow rate and Zn/Al ratio to 0.29 leads to an increase in the O-H contribution. At low Zn concentrations, Zn atoms may substitute for Al atoms in the alumina lattice and suppress the formation of hydroxyl groups on the surface of the deposited film, which was seen in case of Zn-doped TiO_2 previously[172][173]. However, as the Zn concentration increases beyond a certain point (in our case from 5.38 at% in the 0.21Zn-AlO_x sample to 6.86% in the 0.29Zn-AlO_x sample), the solubility limit of Zn in the alumina lattice may be exceeded, and excess Zn atoms may segregate to the surface of the deposited film, due to differences in surface energy between Zn and Al atoms[164]. Zn has a lower surface energy than Al, which means that it prefers to occupy the high energy sites such as the surface and interfaces of the deposited film[174]. The excess Zn atoms can interact with adsorbed water molecules to form Zn-OH species, leading to an increase in the number

of available hydroxyl groups on the surface of the deposited film[175]. Notably, this explanation is consistent with the reported solubility limit of Zn in alumina[164].

The decrease in surface hydroxyl groups on the Zn-AlO_x can have important consequences for its properties. Hydroxyl groups are known to promote adhesion, wetting, and reactivity with water molecules. Oxygen-related defects, including hydroxyl groups, can provide permeation pathways in Al_2O_3 and Zn-AlO_x films[135][76]. Therefore, a decrease in the concentration of surface hydroxyl groups can lead to changes in the refractive index and water vapor transmission rate (WVTR).

As can be seen in Figure Wd, the Al_2O_3 exhibits the characteristic Al2p peak of Al_2O_3 at around 74.2 eV[90]. By introducing Zn, the shape of the Al2p spectrum does not change significantly but the peak is shifted towards lower binding energy, indicating that this is an oxidized Al state with an oxygen-deficient matrix[176] [97]. It also confirms that when zinc is incorporated into the Al_2O_3 lattice, it can substitute for aluminum in the lattice structure or occupy interstitial sites, leading to a distortion of the local crystal structure and a decrease in the electronegativity of the neighboring Al atoms, causing a shift in the binding energy of the Al2p peak towards lower values[176][177]. By increasing the Zn concentration, however, the Al2p peak intensity decreases, consistent with the decreasing Al at% shown in Table 5.1.

The Zn2p spectra of the films are shown in Figure We, in which the Zn2p3/2 peak is between 1022.5 and 1023 eV and the Zn2p1/2 peak is at 1045.4 eV, which indicates that the Zn in the Zn-AlOx films exists in oxidized states[115]. An increase in the intensity of the Zn2p peaks is associated with Zn atoms substituting for Al in the alumina lattice and is consistent with the increasing Zn at% in Table 5.1. Furthermore, for the 0.29Zn-AlO_x sample, there is a slight shift in the Zn2p2/3 peak to a higher binding energy, which is attributed to the segregation of Zn to the surface of the thin film[178]. This

observation is consistent with the greater intensity of the O-H peak in the O1s spectrum associated with the 0.29Zn-AlO_x thin film (Figure Wc).

Figure Wf shows the XRD patterns of Zn-AlO_x with two different doping concentrations (0.21Zn-AlO_x and 0.29Zn-AlO_x) as well as undoped Al_2O_3. The absence of any sharp peaks in the XRD patterns confirmed the amorphous nature of the films. Only the broad peak centered at $2\theta \approx 21°$ from δ alumina is observed in all samples[179]. It can be seen that the incorporation of Zn into the Al_2O_3 lattice resulted in a higher intensity of the amorphous peak and a slight shift of the peak to a lower angle. This shift is attributed to Zn substitution on the Al sites, leading to an increase in the short-range atomic spacing because of the larger ionic radius of Zn^{2+} (0.72 Å) with respect to Al^{3+} (0.53 Å)[180], meaning that the Zn atoms are incorporated as a dopant[181]. The XRD pattern of 0.29Zn-AlO_x showed the presence of an extra broad peak centered at $2\theta \approx 36°$ associated with the wurtzite ZnO structure. This indicates that 0.29Zn-AlO_x is still amorphous in nature (both peaks are broad), but that in increasing the Zn concentration up to 0.29 Zn/Al%, instead of substituting Zn atoms for Al atoms, they form a separate ZnO phase within the alumina film. This results in a film with two distinct phases, Al_2O_3 and ZnO, which is consistent with the increased O-H signal observed at this doping level in Figure Wc [182].

SEM and AFM images of Al_2O_3 and Zn-AlO_x films deposited on a silicon substrate using 85 substrate oscillations are shown in Figure Xa-e, confirming the smooth, pinhole- and crack-free nature of the thin films, indicating a high quality well-suited for TFE. From Figure Xa some randomly distributed particles on the surface of the Al_2O_3 thin film can be observed, which could result from gradual powder formation on the underside of the AP-SALD reactor head. Figure Xe showed a number of small bumps or irregularities with higher height and roughness compared to the surrounding amorphous alumina matrix, which might be associated with ZnO crystallites, consistent with the XRD results. The average root-mean-square (RMS) roughness value was evaluated from 2 to 4 separate AFM

images of each film and is less than 1.7 nm, indicating a good uniformity and smoothness over the whole scanning area.

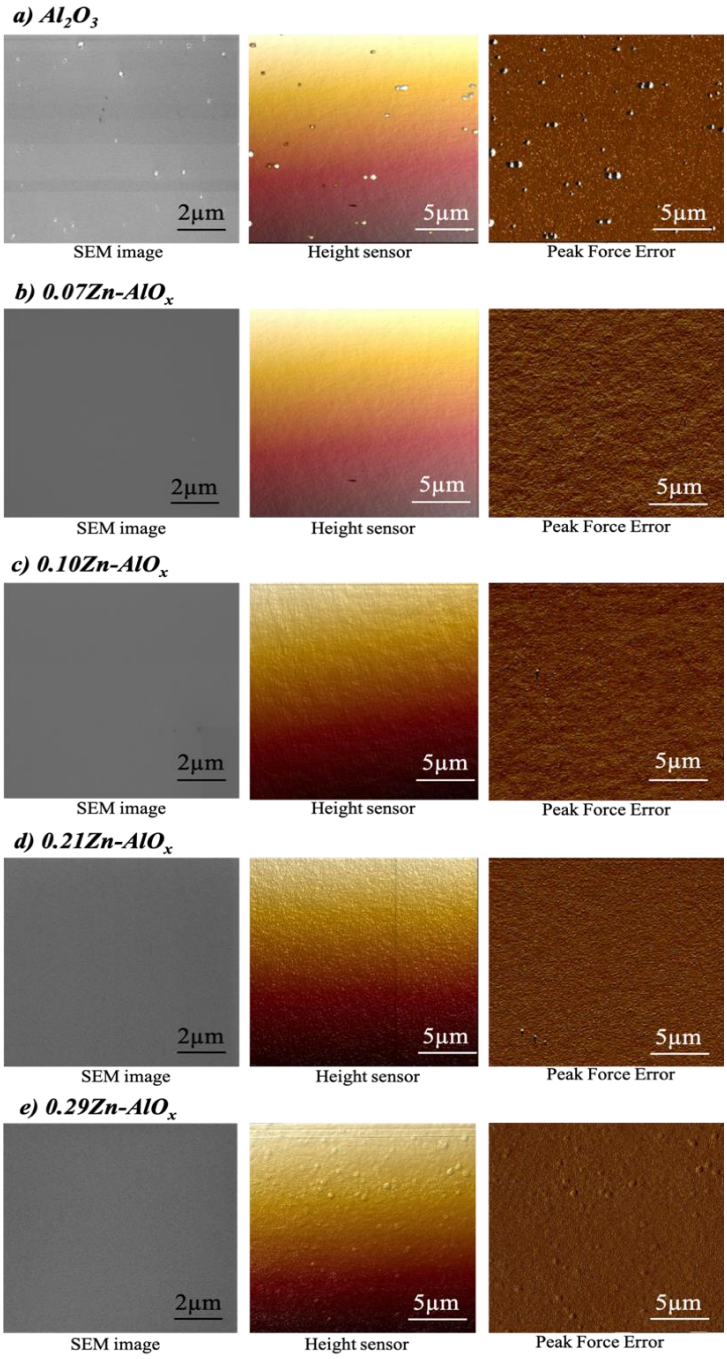

Figure X. SEM, AFM height sensor and peak force error images of a) Al_2O_3, b) 7Zn-AlO_x, c) 10Zn-AlO_x, d) 21Zn-AlO_x, and e) 29Zn-AlO_x deposited with AP-SALD using 85 oscillations on Si substrates.

The RMS values are plotted versus Zn/Al in Figure Ya. The pure Al_2O_3 film is the smoothest, with the lowest RMS value of 0.94 nm. The roughness increased gradually with zinc concentration; however, the surface roughness of all Zn-AlO_x thin films is close to that of the Al_2O_3, indicating that the films grown at these low DEZ flow rates are mainly composed of amorphous Al_2O_3, consistent with the XRD results shown in Figure Wf. The 0.29Zn-AlO_x film exhibits the highest RMS roughness value of 1.7 nm, which is likely due to the presence of small bumps and distinct features with higher roughness as shown in the AFM images. It is important to consider is that the two binary AP-SALD processes yield quite different material properties. ZnO AP-SALD results in films that are polycrystalline, while Al_2O_3 AP-SALD yields amorphous films[114]. Differences in the crystallinity between two materials combined into a ternary AP-SALD process can influence the development of the microstructure during the growth, such as the formation of ZnO islands or the preferential growth of ZnO nanoparticles on the surface[165], which can lead to an increase in surface roughness, as they may protrude above the smoother Al_2O_3 matrix[110].

Ellipsometry was employed to to study the film growth rate and refractive index. By plotting the layer thickness as a function of the number of AP-SALD oscillations (Figure Yb), the growth per cycle was obtained. ZnO was also deposited as a basis for comparison and study of the Zn-doped alumina thin films. Linear trends are observed for all doping levels, indicating a constant GPC. A growth of 0.62 nm/oscillation is determined for Al_2O_3, which is equivalent to 0.31 nm/cycle. The growth rate of the ZnO film is 0.65 nm/cycle. GPCs of 0.11-0.14 nm/cycle and 0.67 nm/cycle are typically reported in literature for alumina and ZnO films grown using similar process conditions by spatial ALD and SCVD, respectively[107], [149][183]. The higher GPCs observed here suggest that AP-SCVD likely occurred due to some precursor mixing in the gas phase, i.e., the gas flow rates and reactor-substrate spacing were such that the TMA/DEZ and water precursors were not perfectly isolated by the inert N_2 gas shield. AP-SCVD conditions are attractive for device manufacturing, since higher

deposition rates are obtained, while still producing smooth, pinhole-free, conformal films with thicknesses proportional to the number of cycles[88]. The GPC of 0.31 nm/cycle for the undoped Al_2O_3 films indicates that approximately 2 to 3 monolayers were deposited each cycle. By incorporating the Zn into the Al_2O_3 thin films, the GPC was observed to have values between approximately 0.34-0.38 nm/cycle for different Zn-AlO_x compositions, as shown in Figure Yb.

When depositing ternary materials by ALD or SALD, the growth rate should in theory follow the rule of mixtures shown in Equation 5-1, which for Zn-AlO_x is[110]:

$$GPC_{Zn\text{-}AlO_x} = (Zn\%)GPC_{ZnO} + \frac{(100\text{-}Zn\%)}{100} GPC_{Al_2O_3} \qquad \textit{Equation 5-1}$$

where Zn% is the Zn content, and GPC_{ZnO} = 0.66 nm/cycles and $GPC_{Al_2O_3}$= 0.31 nm/cycles, which are the GPCs of ZnO and Al_2O_3 films deposited under identical conditions, respectively.

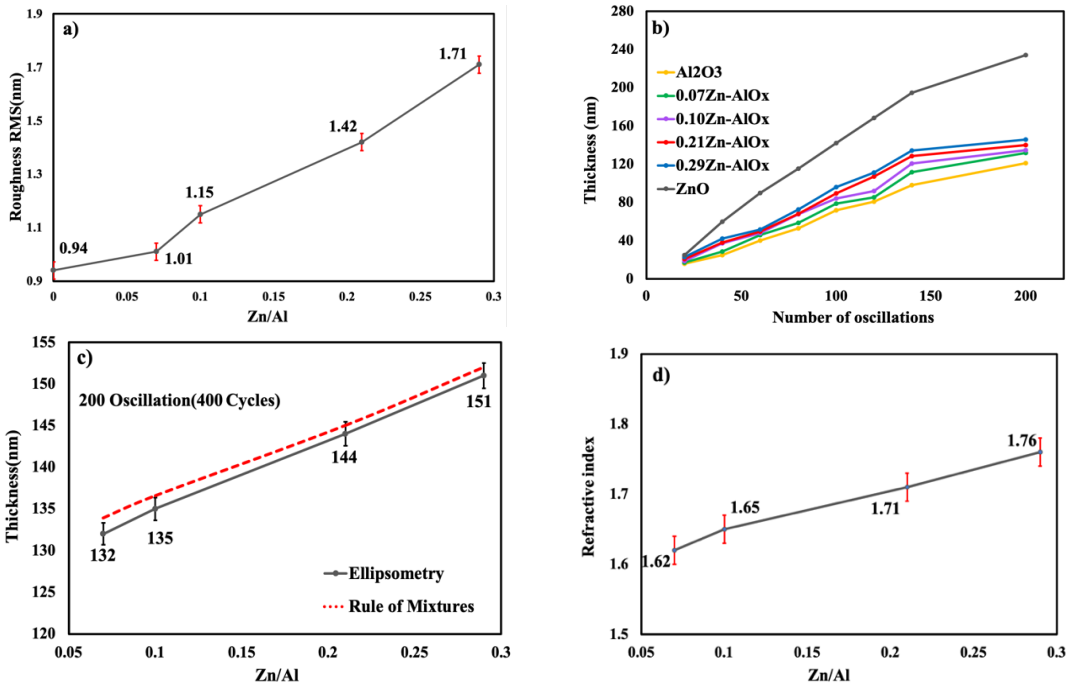

Figure Y. a) Surface roughness, b) Film thickness as a function of the number of AP-SALD oscillations, c) Thickness measured after 200 oscillations with ellipsometry and rule of mixture, and d) Refractive index for different Zn/Al on silicon substrates. (Refractive indices and surface roughness were measured for 60 nm thick films deposited using AP-SALD on silicon substrates.)

Figure Yc shows the thicknesses of the Zn-AlO_x thin films with different Zn/Al ratios deposited using 200 AP-SALD oscillations (solid line), as well as the expected thickness calculated using the rule of mixtures (dashed line). The error bars represent the standard deviation of 3−5 separate ellipsometry measurements at different locations on each of the Zn-AlO_x films. The measured thicknesses show the same trend as the calculated values, indicating that the GPC of the Zn-AlO_x films was consistent with a linear combination of the GPCs of each binary oxide and that the co-injection of the metal precursors allows for good control of the film thickness and composition[116]. Deviation from a linear growth relationship has been reported for multicomponent ALD films deposited by alternating the individual sub-cycles of Al_2O_3 and ZnO layers, which was attributed to reduced adsorption of DEZ on the freshly deposited AlO_x layer[184]. This phenomenon was explained by competitive adsorption of the two precursors[110]. TMA is approximately 25% more reactive to the surface sites than DEZ, causing a lower formation enthalpy for Al_2O_3 than ZnO, which results in etching some of the Zn surface species and poor control of the film thickness[110]. The slight difference in the measured and calculated thicknesses in Figure Yc may be due to some DEZ etching, however, the similar values indicate that this co-injection configuration could potentially address some of the problems that exist within the super-cycle deposition in terms of thickness control.

The AP-SALD Zn-AlO_x co-injection configuration results in an adsorbed monolayer containing two different precursor molecules, which then can be converted into a multicomponent film by exposure to the co-reactant. The overall reaction can be expressed by[115]:

$$2\ \text{S-OH*} + \text{Al}(CH_3)_3 + \text{Zn}(C_2H_5)_2 \rightarrow \text{S-O-Al}\,(CH_3)_2\text{*} + \text{S-O-Zn}(C_2H_5)\text{*} + \text{by-products} \qquad \textit{Equation5-2}$$

$$\text{S-O-Al-}(CH_3)_2\text{*} + \text{S-O-Zn}(C_2H_5)\text{*} + H_2O \rightarrow \text{S-O-Al-OH*} + \text{S-O-Zn-OH*} + \text{by-products} \qquad \textit{Equation 5-3}$$

where S- refers to the surface of the substrate. Thus, although the overall growth rate (GPC) is dominated by the kinetics of the ZnO and Al_2O_3 reactions, the amount of zinc incorporated into the

matrix is determined by the competition between the TMA and DEZ precursors at the surface which could affect the thin films' refractive index values.

The refractive indexes were measured by ellipsometry to be 1.60 and 1.92 at 632.8 nm wavelength for the AP-SCVD Al_2O_3 and ZnO, respectively. These values are in excellent agreement with previous reports[183][26]. Figure Yd demonstrates the refractive index (n) of the thin films with various Zn/Al. Due to the modest Zn concentrations, the refractive indexes of the Zn-AlO_x films are very close to pure Al_2O_3. As expected, with increasing the Zn concentration, the refractive index increases, pushing toward the refractive index of ZnO. In literature, the relationship between refractive index and film density is described as linear; therefore, the higher refractive indexes for Zn-AlO_x indicate an increased film density that is associated with an improved film quality and compactness[151][171]. Moreover, the observed trend of increasing refractive index with increasing Zn concentration is consistent with the XPS results, as the decrease in the amount of hydroxyl groups is expected to result in an increase in density and subsequently refractive index. The obtained results demonstrated the possibility of tuning the refractive index as a function of Zn dopant concentrations by variation of the DEZ flow rate.

5.3.2 Water vapor transmission rate measurements

In this study, we employed an optical Ca test to evaluate the gas diffusion barrier properties of AlO_x and Zn-AlO_x thin films[126]. For this investigation, Al_2O_3 and Zn-AlO_x films with thicknesses of 60 nm were deposited directly on top of thermally evaporated Ca films using the AP-SALD system in approximately 5 minutes. Then, the encapsulated Ca films were exposed to ISOS-D-3 (65°C-85%RH) testing conditions[134] and the oxidation/transparency of the Ca films was monitored by photographic imaging to determine the WVTR values of the TFE layers using a method reported previously[130](see Experimental Methods for full details). All TFE layers displayed similar behavior during this

experiment, therefore, the results described below will concentrate on two samples: Al_2O_3- and 0.21Zn-AlO_x-coated Ca films as representatives of the entire set of samples. Pictures of the Ca films encapsulated with the Al_2O_3 and 0.21Zn-AlO_x layers after different testing durations were converted into high-contrast black-and-white images, as shown in Figure Z, using IMAGEJ, where the white areas correspond to oxidized Ca and the metallic Ca film appears black, which allow the defects in the encapsulation layer to be directly visualized.

The images in Figure Z(a) revealed that there are two types of defects that appear and grow radially with time. The first type are defects that are present initially in the photographic images (30-50 min). SEM and AFM in Figure X confirmed that the Al_2O_3 and Zn-AlO_x films are pinhole and crack free. Therefore, these defects are probably caused by particles on the initial Ca films which either mask the underlying Ca film from Al_2O_3 encapsulation or cause a crack in the Al_2O_3 and lead to a pinhole defect in the barrier which could provide a permeation path for water and affect the permeation performance[156]. The second type of defect is associated with the burst of new circular oxidation areas that appeared suddenly at later times (70 min) and grew radially versus time. We believe that these defects are caused by water corrosion of the Al_2O_3 AP-SALD film, similar to the mechanism discussed in Chapter 4 and described in a recent study of Al_2O_3 ALD TFE[158]. That study proposed that H_2O transmission through Al_2O_3 ALD films occurs by H_2O permeating along percolation paths formed by OH- defect clusters. These percolation paths do not exist initially and form progressively with time resulting from H_2O corrosion of the Al_2O_3 film[158]. A certain fraction of OH- defect clusters exists in the Al_2O_3 AP-SCVD film, as shown in Figure Wc. Figure Z(b) shows that 0.21Zn-AlO_x films enter the blooming phase slower than Al_2O_3 films, indicating a lower WVTR value. In the case of Zn-AlO_x TFE, the WVTR can be affected by several factors, including the amount of surface hydroxyl groups and film compactness. The XPS results in Figure Wc showed that by introducing Zn into Zn-AlO_x, the OH-defect concentration decreased, which can result in a lower WVTR, because the probability of a

percolation path existing will decrease as the OH- defect concentration decreases on the sample surface[76]. Moreover, increasing the Zn/Al in Zn-AlO_x increased the refractive index (Figure Yd). A film with a higher refractive index may have more tightly packed atoms (more compact), which can reduce the number of pathways available for water vapor diffusion, resulting in a lower WVTR. On the other hand, an increase in surface roughness was observed for increasing Zn/Al (Figure Ya), which should increase the number of surface defects, which can act as preferential pathways for water penetration and result in a higher WVTR.

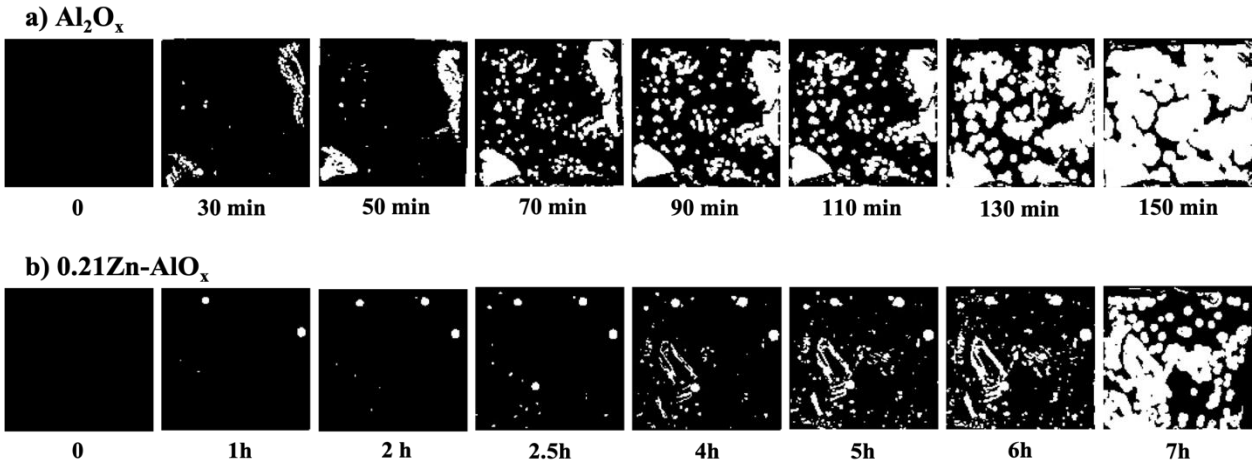

Figure Z. High-contrast black-and-white images of 1.8cm×1.8cm Ca films encapsulated with a) Al_2O_3 and b) 0.21Zn-AlO_x TFE with a thickness of 60 nm after storage in ISOS-D-3 (65˚C-85% RH) conditions for increasing time intervals.

The WVTR values were obtained using Equation 3-1 (see Experimental Methods for full details)[157]. The WVTR values of the TFE layers with different Zn/Al can be seen in Figure AAa. The WVTR values are on the order of 10^{-4} g/m^2/day at 65˚C-85%RH, indicating that all of the films are good barriers to water-vapor permeation. The Zn-AlO_x TFE layers consistently showed lower WVTR values compared to the undoped Al_2O_3. It is also seen in Figure AAa that the WVTR values decrease by increasing the Zn/Al up to 0.21 but that adding more zinc (Zn/Al of 0.29) increased the WVTR slightly, which could be related to the increased OH content (Figure Wc) and possible ZnO segregation

discussed earlier. ZnO is a more hydrophilic material compared to Al_2O_3, and the presence of ZnO islands in the amorphous Al_2O_3 matrix can create preferential paths for water-vapor diffusion through the encapsulation layer. These paths can increase the WVTR value. Additionally, the polycrystalline ZnO islands and grain bounderies can act as defects and further facilitate water vapor diffusion[185].

Therefore, the effect of Zn concentration on the WVTR of Zn-AlO_x is complex and depends on multiple factors, including the amount of surface hydroxyl groups, film density, and surface roughness. Optimizing the Zn concentration in Zn-AlO_x TFE is crucial to achieve the desired WVTR. A balance must be struck between the reduction in surface energy due to the decrease in hydroxyl groups and the increase in film density, and any increase in WVTR due to surface roughness and ZnO formation. By carefully controlling the Zn concentration, it is possible to achieve an optimal balance and minimize the WVTR while maintaining good film properties, which in our case was observed for Zn/Al= 0.21.

5.3.3 Perovskite solar cells characterization and stability test

To assess whether the AP-SALD/SCVD process influences the PSC performance, 60-nm-thick 21Zn-AlO_x TFE layers were deposited on a p-i-n PSC structure consisting of FTO/PTAA/$FA_{0.92}MA_{0.08}PbI_3$/$PC_{61}BM$/BCP/Ag using 80 AP-SALD oscillations in only 4 minutes. The J–V curves measured under simulated solar illumination in air for the PSC before and after deposition of the 0.21Zn-AlO_x TFE layers are shown in Figure AAb. The power conversion efficiencies (PCE) and fill factors (FF) of the PSCs are listed inside Figure AAb. The J-V curves are nearly identical, indicating that the deposition of the TFE layer had no obvious effect on the performance of the solar cells. The $FA_{0.92}MA_{0.08}PbI_3$ perovskite layer used in this study, is expected to be unstable above approximately 150˚C [119]; however, the short AP-SALD times used in this work (i.e., 4 min) facilitate deposition temperatures in this range (e.g., 130°C)[19].

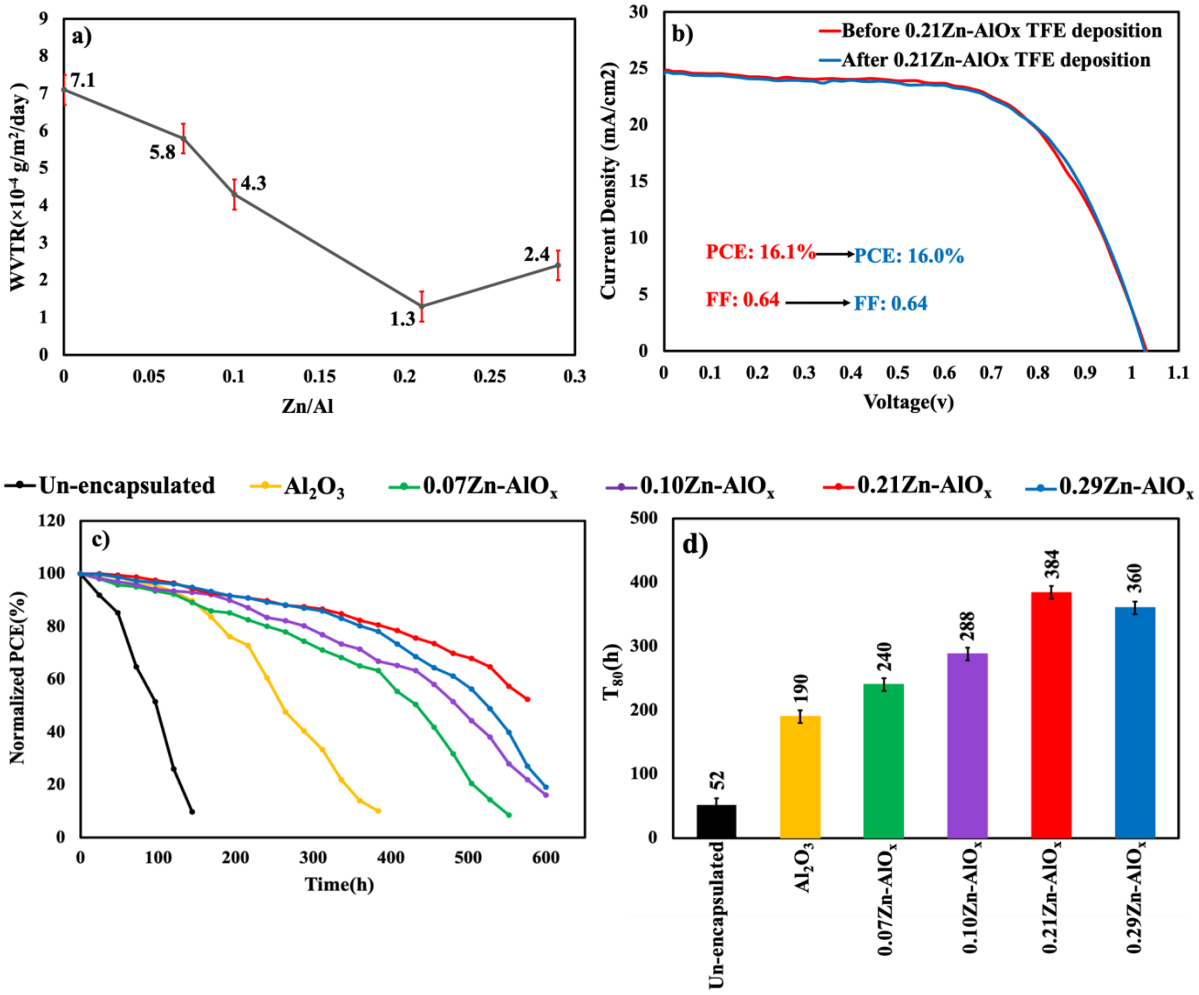

Figure AA. a) *WVTR values for the 60-nm-thick TFE layers deposited with AP-SALD at ISOS-D-3 (65˚C-85% RH). b) J–V characteristics of p-i-n PSCs before and after deposition of 60 nm 21Zn-AlO$_x$ TFE layer via AP-SALD. c) Normalized PCE versus time and d) the T$_{80}$ values of p-i-n PSCs encapsulated with different thin film encapsulation layers kept at ISOS-D-3 (65˚C-85%RH). The PCE values were normalized to their initial PCE value.*

To study the performance of the Zn-doped TFE layers, the PSC performance was then monitored over extended periods under harsh environmental test conditions. p-i-n PSCs were coated with 60 nm of Al_2O_3 or Zn-AlO_x with different Zn/Al, and the encapsulated cells and control cells without an encapsulation layer were exposed to accelerated ISOS-D-3 test conditions (dark, 65˚C-85% RH)[134] and the PCEs of the cells were monitored as shown in Figure AAc. it can be seen that the

stability of the devices increased markedly by applying an encapsulation layer. For example, the PSC without encapsulation degrade to 80% of its original efficiency in 52 h (T_{80}= 52 h)[134], which is attributed due to the rapid permeation of moisture into the device leading to accelerated decomposition of the perovskite layer and degradation of its interface with charge transport layers[69]. In contrast, all encapsulated PSCs in Figure AAc displayed T_{80} values greater than 190 h. Similar to the N-doped TFE in Chapter 4, this can be attributed to the Al_2O_3 and Zn-AlO_x TFE layers slowing down the ingress of H_2O and oxygen from the ambient and the egress of volatile species from the devices.

Figure AAd shows the T_{80} values of the p-i-n PSCs with the various TFE layers kept at ISOS-D-3 conditions. It is observed that the devices with Zn-AlO_x TFE showed better stability than those with Al_2O_3 TFE, consistent with the lower WVTR values. The PSCs with Al_2O_3 TFE showed average T_{80} values of 190 h, whereas the PSCs with the 0.21Zn-AlO_x TFE showed average T_{80} values of 384 h. The optimal Zn/Al in Figure 5d is around 0.21 (corresponding to 5.4 at% Zn in Table 5.1), consistent with the lowest WVTR value reported in Figure AAa.

The Zn-doping improves the film compactness and reduces the fraction of hydroxyl groups on the film surface. However, increasing the Zn/Al beyond the optimal range can result in a decrease in the effectiveness of the encapsulation layer due to an increase in the WVTR. Therefore, the key requirement to produce a better barrier layer is to increase the density and compactness of the coatings as much as possible and reduce the number of water diffusion pathways by optimizing the Zn concentration.

Chapter 6

The Effect of Different Oxidants on Alumina TFE layers

6.1 Introduction

Most often TMA is used as the aluminum source and water as the co-reactant for the deposition of alumina, since H_2O often shows facile ligand exchange reaction during ALD[186], and also because of its low environmental impact and process viability. However, there are several reports that water-based ALD materials suffer from specific failures. For example, oxide films deposited with H_2O often include oxygen vacancies or hydrogen within their bulk[187], which can lead to unwanted permeation pathways for moisture[122]. It has been established that the material properties and process conditions of Al_2O_3 ALD are strongly affected by the type of the oxidant used for deposition[108]. An improvement in film properties when ozone or an oxygen plasma were used as the oxygen source, instead of water, was previously reported[107][108]. This was attributed to a higher film density and/or a lower content of impurities and unreacted OH- groups within the film, due to a high electrochemical potential and high volatility.[108]. The growth of ozone-based metal oxides can also be performed at significantly lower temperatures[188]. However, ozone must be generated in situ, which involves a lot of equipment and it suffers from high cost[103]. Hydrogen peroxide (H_2O_2) can be an ideal alternative to ozone or H_2O as an oxidant, since H_2O_2 has similar oxidation properties to ozone (oxidation potential of O_3 = 2.1V versus 1.8V for H_2O_2) while simultaneously having slightly stronger proton-transfer properties than water (H_2O_2 pKa = 6.5 versus pKa = 7.0 for water)[189].

However, the properties of Al_2O_3 TFE layers deposited by AP-SALD using oxygen sources other than H_2O, especially H_2O_2, have yet to be characterized in detail and incorporated into PSC device studies. Only a limited number of previous studies have considered H_2O_2 as a potential oxidant in ALD

deposition[105][190] and to the best of our knowledge, there are currently no published reports on the use of H_2O_2 in a spatial ALD process, which could be partially due to difficulty in dosing pure H_2O_2, since it is often supplied as a mixture with H_2O, hindering analysis of its own chemical reaction mechanisms, which determine the process conditions such as deposition temperature and amount of reactant exposure required for SALD[189].

In this Chapter, I investigate the deposition rate, microstructure and barrier properties of Al_2O_3 thin films deposited by AP-SALD using H_2O, H_2O_2 and O_3 as the oxidant. The AP-SALD process conditions are optimized to prevent degradation of the perovskite layer and maximize the PSC stability, which is measured under ISOS testing conditions[134]. As a result, we successfully enhance the stability of the PSCs (T_{80}=312 h at 65˚C-85% RH) with a single TFE layer deposited rapidly in open-air. We believe that this study can prompt further improvement in the barrier properties of Al_2O_3 layers deposited with alternative oxidants, resulting in further PSC lifetime enhancements.

6.2 Experimental

We kept all AP-SALD conditions constant and varied only the oxygen source, to gain insights into the effects of different oxygen precursors on the properties of the resulting TFE layers, such as surface roughness, growth rate, and refractive index. Al_2O_3 thin films were deposited in open-air conditions using the AP-SALD/SCVD system described in Chapter 3. TMA as well as water, hydrogen peroxide (30% H_2O_2 in water) and O_3 were used as the metal and oxygen precursors, respectively. During the study, a constant nitrogen flow was maintained at 25 SCCM through the TMA bubbler and 100 SCCM through the water or hydrogen peroxide bubbler. Meanwhile, the gas flow rates were fixed at 105 SCCM and 150 SCCM through the TMA and oxidant carrier lines, respectively, to ensure that the only changing parameter was the oxygen source material. For depositions with O_3, O_2/N_2 gas (7.5% nitrogen balance oxygen) was supplied to an Atlas 30 UHC ozone generator (Absolute Ozone) set to

80% power and subsequently delivered to the reactor head, resulting in a flow rate of 125 SCCM per oxygen precursor channel. The expected ozone concentration for these settings is 221.9 g/Nm^3. The deposition conditions are summarized in Table 6.1. The substrate was placed on the heated substrate stage (set to 130 °C) and positioned underneath the reactor head with a vertical separation distance of 100 μm. The heated stage was oscillated back and forth at the speed of 50 mm/s to expose the substrate to the alternating precursor flows. In this study, experimental conditions were selected such that the inert gas flow and exhaust strength are insufficient to prevent mixing of the reactant vapors in the gas phase during the oscillation of the substrate, directing the system to operate in AP-SCVD mode.

6.3 Results and discussions

6.3.1 Thin film characterization

XPS was performed to clarify the chemical composition of 60-nm-thick H_2O-AlO_x, H_2O_2-AlO_x and O_3-AlO_x thin films deposited using 85 oscillations in 5 minutes (Table 6.1). For the samples prepared with O_3 and H_2O_2, we find O/Al ratios of 1.38 and 1.42, respectively, which are lower than that of the H_2O-AlO_x sample, which is close to the stoichiometric value of 1.5[191]. Replacing water with a more reactive oxidant like H_2O_2 or O_3 can alter the surface chemistry. The amount of oxygen incorporated into the alumina thin film during the deposition process is related to the reactivity of the oxidant and the reaction energy of the oxidant with TMA surface species. Ozone is a highly reactive oxidant, which is capable of oxidizing TMA to produce alumina with high efficiency and reduce the number of oxygen defects and surface hydroxyl groups in the O_3-AlO_x thin film[188][106]. The O1s and Al2p XPS spectra will be investigated shortly hereafter to clarify the O/Al ratios and O-H % contributions.

The C/Al ratio is also reported in Table 6.1 and is seen to decrease when switching from H_2O to H_2O_2 to O_3 as the oxidant. Ozone can produce a large number of oxygen radicals, which can react

with TMA molecules to produce aluminum oxide and volatile carbon-containing species. Moreover, the overall reaction energy of ozone with Al–CH_3 surface species is much greater than that of H_2O_2 or H_2O (shown in Table 6.1), which strongly drives the reaction and makes it more likely to reach completion, resulting in a lower C/Al ratio[106][192]. The higher C/Al observed for H_2O-AlO_x is consistent with the fact that the removal of CH_3 surface species by forming CH_4 molecules via reaction with H_2O is less favored than ligand removal from Al ions via reaction with O_3, due to the higher activation energy for the reaction with H_2O, as shown in Figure J. This results in incomplete surface reactions and a higher amount of carbon when using H_2O as the oxidant[191].

Table 6.1. Deposition conditions, compositions, and overall reaction energy of AP-SCVD Al_2O_3 thin films deposited using different oxidants, as determined by x-ray photoelectron spectroscopy.

Samples	AP-SALD Deposition Conditions				Films Composition		Overall Reaction Energy (Kcal/mol)
	TMA precursor bubbling rate (SCCM)	Metal Carrier gas flow rate (SCCM)	Oxidant precursor bubbling rate (SCCM)	Oxidant Carrier gas flow rate (SCCM)	O/Al	C/Al	
Al_2O_3-H_2O	25	100	100	150	1.50	1.02	-31
Al_2O_3-H_2O_2	25	100	100	150	1.43	0.55	-84
Al_2O_3-O_3	25	100	O_3 power = 80%	150	1.37	0.45	-160

The O1s, Al2p and C1s XPS spectra of the 60-nm-thick AlO_x deposited with different oxygen precursors are shown in Figure BB. Deconvolution of the O1s peaks by Gaussian fitting in Figure BBa-c revealed peaks at 530.6 and 532.2 eV, which correspond to lattice oxygen (i.e., Al-O) and non-lattice and surface oxygen (e.g., O-H, hydroxyl groups), respectively[142]. The Al2p spectra (Figure BBd) showed a single peak with a binding energy of 74.3 eV corresponding to the Al-O bond, consistent with the 530.6 eV peak in the O1s spectra (Figure BBa-c) [90]. The fraction of the O1s signal attributable to Al-O and O-H components was calculated for the H_2O-AlO_x, H_2O_2-AlO_x and O_3-AlO_x thin films based on the area under the corresponding XPS peaks and is listed inside each plot. The Al-O fraction of the O1s spectra is higher for the H_2O_2-AlO_x film (81%) than the H_2O-AlO_x film (71%) (Figure BBa,b) and further increased to 87% when using O_3 as the oxygen precursor (Figure BBc). It is known

that thermal deposition at low temperatures using H_2O as the oxidant usually results in a large amount of O-H groups on the film surface, due to incomplete reaction of the precursors and the high desorption energy of water at low temperatures [143][144]. Stronger oxidants (H_2O_2 or O_3) can more efficiently oxidize the TMA precursor, leading to the formation of a higher proportion of surface Al-O groups and fewer surface O-H hydroxyl groups[193], which is consistent with the observed reduction in O/Al %.

Considering now the C1s spectra (Figure BBe), the presence of several components was noted. The main components of the C1s signals are aligned at 284.4 eV, which is attributed to the presence of hydrocarbons physi-sorbed on the sample surface. The second peak at 286 eV could be assigned to C-O bonds. In addition, a non-negligible third component lies at a binding energy of 289 eV and could be assigned to the presence of carbonate species[194]. These carbon contaminants are explained by the incorporation of residual precursor that it is not completely desorbed during the growth process[108]. Figure BBe shows that the intensity of the C1s peak decreases when replacing water with H_2O_2 and O_3, consistent with the lowest C/Al ratio for O_3-AlO_x reported in Table 6.1. This decrease is due to the effective removal of trimethyl groups from TMA and desorption of by-products[142], as ozone has a higher reactivity and can result in more complete reactions compared to H_2O_2 and H_2O during the deposition process[103].

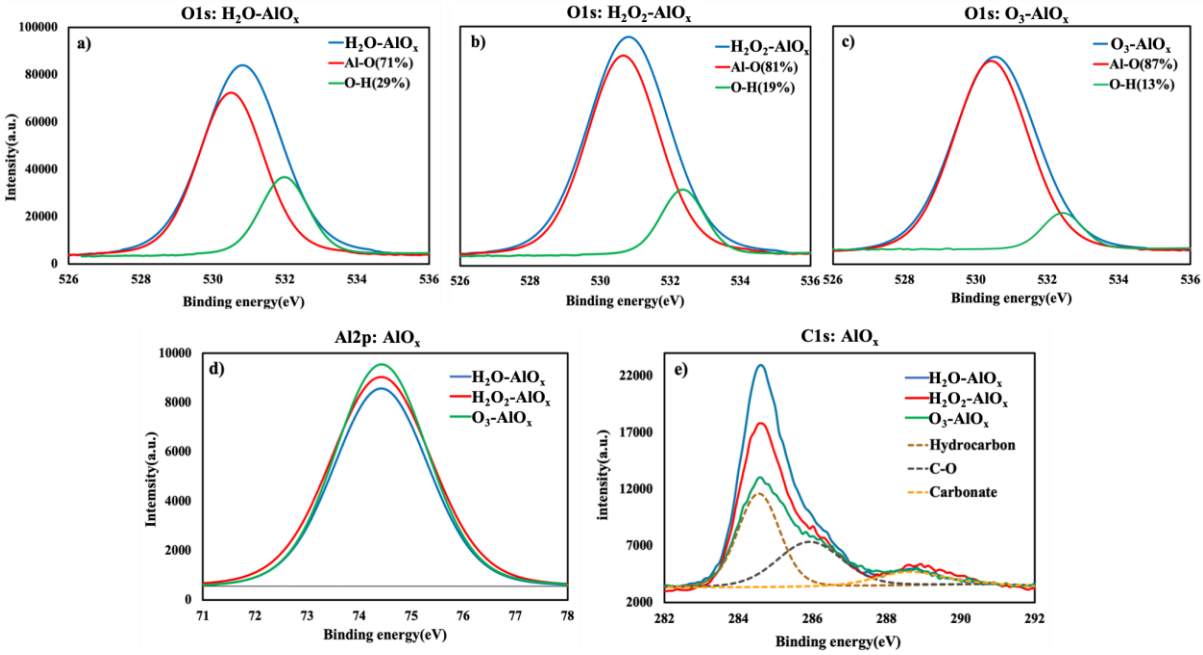

Figure BB. O1s XPS spectra of a) H_2O-AlO_x, b) H_2O_2-AlO_x, and c) O_3-AlO_x thin films. The fraction of the O1s XPS signal attributable to Al-O and O-H components is reported inside the plots. d) Al2p and e) C1s XPS spectra of AlO_x thin films.

In order to study the uniformity, compactness and roughness of the thin films, ellipsometry, SEM and AFM were conducted on the AlO_x thin films deposited on a silicon substrate using 85 substrate oscillations. Figure CCa-f show SEM and AFM images of the H_2O-AlO_x, H_2O_2-AlO_x and O_3-AlO_x films. All films are smooth, pinhole- and crack-free, indicating a high quality well-suited for TFE. Figure CCa and d showed some randomly distributed large particles on the surface of H_2O-AlO_x, which could result from gradual powder formation on the underside of the AP-SALD reactor head, indicating that some mixing of the precursors in the gas phase may have occurred, which is discussed further below.

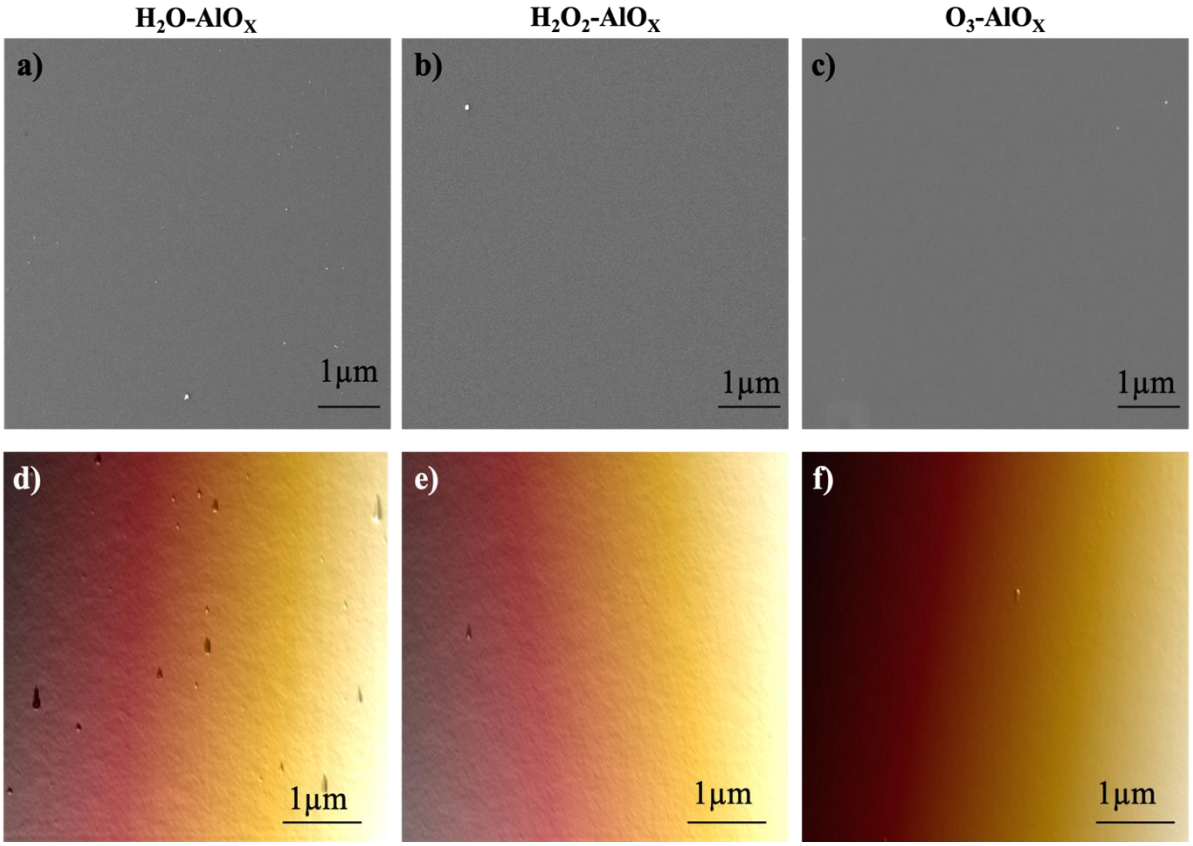

Figure CC. SEM images of a) H_2O-AlO_x, b) H_2O_2-AlO_x, and c) O_3-AlO_x, AFM images of d) H_2O-AlO_x, e) H_2O_2-AlO_x, and f) O_3-AlO_x deposited with AP-SALD using 85 oscillations on Si substrate.

The growth per cycle and the refractive index at a wavelength of 632.8 nm are deduced from the ellipsometry data. By plotting the film thickness as a function of the number of AP-SALD oscillations (Figure DDa), the GPC was obtained for each oxidant. Linear trends are observed for all deposited AlO_x thin films, indicating a constant GPC. According to our observations, the use of different oxidants in AP-SCVD resulted in different growth rates per cycle. H_2O-AlO_x was found to have the highest growth rate per cycle, followed by O_3-AlO_x and H_2O_2-AlO_x which is in a good agreement with previous studies[107][192]. All the deposited films showed higher GPCs compare to the conventional ALD process, confirming that AP-SCVD occurred due to some precursor mixing in the gas phase, i.e., the gas flow rates and reactor-substrate spacing were such that the TMA and oxidant

were not perfectly isolated by the inert N_2 gas. A growth of 0.70 nm/oscillation is determined for H_2O-AlO_x, which is equivalent to 0.35 nm/cycle. This indicates that approximately 2 to 3 monolayers were deposited each cycle.

The growth rate of O_3-AlO_x was higher than that of H_2O_2-AlO_x, which is attributed to the higher reactivity of the ozone. The overall reaction energy can affect the growth rate of thin films deposited with SALD[103]. It was previously reported that the overall reaction energy of two O_3 with one Al–CH_3 surface species is much greater than that observed with H_2O_2[106]. Combined with the smallest activation energy, molecular ozone is expected to exhibit high reactivity toward oxidation of Al–CH_3 surface species. Therefore, the growth rate of the AlO_x thin films at identical deposition conditions may parallel the reactivity of each oxidant, resulting in a higher GPC for AlO_x deposition using O_3[106]. The overall reaction energy of two H_2O_2 with one Al-CH_3 surface species is larger than that of H_2O due to the higher reactivity of H_2O_2. This higher reactivity would drive the TMA/H_2O_2 reaction and result in a higher growth rate[106]. However, our results (Figure DDa) showed that the growth rate of H_2O_2-AlO_x was lower than that of O_3-AlO_x and H_2O-AlO_x, indicating that while reaction energy and reactivity are important factors, other factors such as vapor pressure and surface density of nucleation sites can also play a significant role in determining the growth rate of the deposited thin film[186]. The highest GPC was observed for H_2O-AlO_x rather than the more reactive oxidants H_2O_2 and O_3, which could be due to multilayer water condensation on the substrate surface by physisorption[108]. At low deposition temperatures (below 300°C) water molecules tend to form multilayers instead of monolayer and insufficient purging can lead to an additional superposed CVD-like film growth, resulting in a higher than expected growth rate[108]. The lower growth rate of H_2O_2-AlO_x may also be attributable to the lower vapor pressure of H_2O_2, which produces fewer OH- functional groups[104]. Considering the Langmuir adsorption isotherm, the maximum surface coverage of chemisorbed OH- groups might strongly depend on the vapor pressure of H_2O or H_2O_2[104]. Since the vapor pressure of

H_2O_2 (7.33 Torr) is lower than that of H_2O (9.2 Torr), a lower density of chemisorbed OH- groups is expected to be generated when using H_2O_2 instead of H_2O, which could contribute to the lower growth rate of H_2O_2-AlO_x[104].

The refractive indices were measured by ellipsometry to be 1.56, 1.63 and 1.67 for the H_2O-AlO_x, H_2O_2-AlO_x and O_3-AlO_x, respectively, as shown in Figure DDb. These matched well with the 1.53–1.78 range reported previously for Al_2O_3 [90]. H_2O_2-AlO_x and O_3-AlO_x thin films showed a higher refractive index than H_2O-AlO_x, indicating an increased film density that is associated with an improved film quality[151], which is in a good agreement with the lower O-H and carbon contents of the H_2O_2-AlO_x and O_3-AlO_x films observed by XPS. In general, the refractive index of a film depends on its density, which can be increased by reducing the incorporation of CH_3 by-products and other impurities, such as surface hydroxyl groups[195].

Moreover, the average RMS roughness value was evaluated from 2 to 4 separate AFM images of each film, as shown in Figure DDc, since roughness is a significant factor in determining the barrier properties of thin film encapsulation. A low surface roughness (RMS roughness value between 1.02-0.76 nm) was achieved for all AlO_x films, indicating a good uniformity and smoothness over the whole scanning area. The O_3-AlO_x film is the smoothest film with the lowest RMS value of 0.76 nm, followed by H_2O_2-AlO_x (RMS=0.93 nm), whereas the RMS value for H_2O-AlO_x is 1.02 nm. The increase in surface roughness when using water as the oxygen precursor may be related to multilayered water absorption. The use of water can result in incomplete reactions and impurities on surface, which can accumulate if not effectively removed by a sufficient nitrogen flow rate[103]. In contrast, ozone can provide smoother thin films due to its highly reactive nature and ability to provide more complete surface coverage [196].

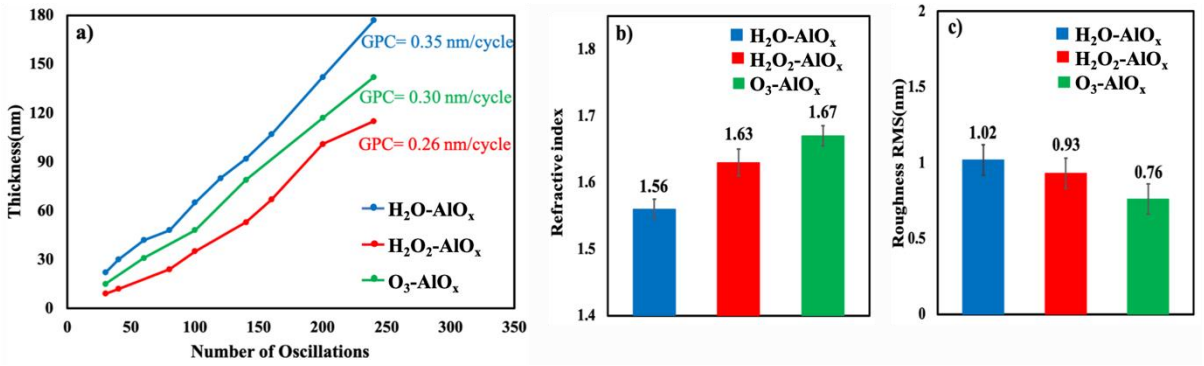

Figure DD. a) Film thickness as a function of the number of AP-SALD oscillations for different oxygen precursors on silicon substrates. Corresponding growth per cycles are listed inside the plot. b) refractive indices, and c) surface roughness for different oxygen precursors. (Refractive indices and surface roughness were measured for 60 nm thick films deposited using AP-SALD on silicon substrates.)

6.3.2 Water vapor transmission rate measurements

High-contrast black-and-white images of the Ca films encapsulated with the AlO_x thin films after different testing durations in ISOS-D-3 conditions (65˚C-55%RH) are shown in Figure EE. The defects observed in Figure EE are likely caused by water corrosion of the AP-SCVD AlO_x thin films, which produced oxidation areas that grew radially versus time. This is similar to the mechanism described in the previous chapters and in recent studies for Al_2O_3 ALD TFE, where H_2O transport through the film occurs by permeation along percolation paths formed by OH- defect clusters[158]. These percolation paths are formed progressively over time due to H_2O corrosion of the film. As can be seen in Figure EE, the O_3-AlO_x thin film encapsulation showed a similar oxidation pattern but at later times, indicating that the permeation rate for water molecules through the O_3-AlO_x TFE was lower than for the H_2O-AlO_x and H_2O_2-AlO_x TFE, indicating a lower WVTR value. This is attributed to the lower concentration of OH- defects in the O_3-AlO_x film as compared to the H_2O_2-AlO_x and H_2O-AlO_x, consistent with the XPS results in Figure BB. A lower concentration of surface hydroxyl groups reduces the probability of percolation paths forming and thus decreases the WVTR[76]. Moreover, replacing water with a more reactive oxidant (O_3 or H_2O_2) increased the refractive index (Figure DDb). A film

with a higher refractive index may have more tightly packed atoms (higher density), which can reduce the number of pathways available for water-vapor diffusion, resulting in a lower WVTR[108]. Clearly, the rate of Ca oxidation for the H_2O-AlO_x film was considerably higher than those of the other films. The Ca films encapsulated with H_2O-AlO_x reached almost complete oxidation at 150 minuets, while the oxidation area of the Ca films encapsulated with H_2O_2-AlO_x and O_3-AlO_x films changed by only 49% and 41% after 6 h, respectively. The WVTR values were obtained by analyzing the oxidized surface area of the Ca films based on Equation 3-1[157]. The calculated WVTR values were 5.8×10^{-4} g/m^2/day for H_2O-AlO_x, 1.7×10^{-4} g/m^2/day for H_2O_2-AlO_x, and 1.5×10^{-4} g/m^2/day for O_3-AlO_x, indicating that all of the films are good barriers to water-vapor permeation. As expected, the WVTR values decreased by using more reactive oxidants. Even though the process in this work was performed at a temperature of 130 °C, which is a relatively low temperature, by carefully controlling the deposition conditions, it is possible to achieve a high-quality TFE and minimize the WVTR.

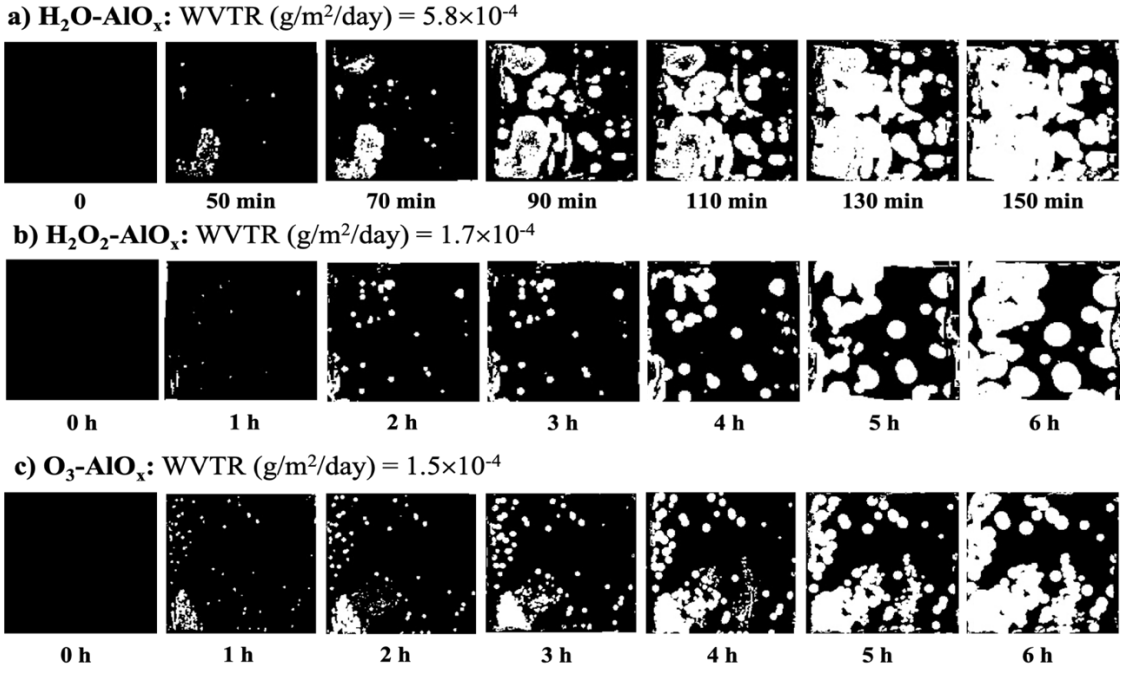

Figure EE. High-contrast black-and-white images of 1.8cm×1.8cm Ca films encapsulated with a) H_2O-AlO_x, b) H_2O_2-AlO_x and c) O_3-AlO_x TFE with a thickness of 60 nm after storage in ISIS-D-3 (65˚C-85% RH) conditions for increasing time intervals.

Having established a relationship between the WVTR and oxidant, which resulted in different quantitates of surface OH- groups, it is now possible to re-consider the role of the OH- groups in the WVTR improvements observed with nitrogen and zinc doping in the previous chapters. Table 6.2 reports the percentage of the O1s XPS signal attributable to OH- groups and the corresponding WVTR for the different doping strategies studied. When the percentage of surface OH- groups is reduced from 29% (H_2O-AlO_x) to 19% (H_2O_2-AlO_x), the WVTR decreases by approximately 71% from 5.8×10^{-4} to 1.7×10^{-4} g/m^2/day. In the N-AlO_x study, a higher fraction of OH- groups in the O1s XPS spectra was observed, which may be attributable to the synthesis conditions at different times (e.g., relative humidity). But it is seen that the addition of 0.28% N into the alumina lattice leads to a relatively small reduction in the fraction of OH- group in the O1s XPS spectra from 41% to 36%, but the WVTR decreases from 7.8×10^{-4} to 5.7×10^{-4} g/m^2/day, a smaller transmission rate than was observed when H_2O was used as the oxidant and the OH- contribution was 29%. This suggests that the WVTR reduction in the 0.28N-AlO_x cannot be attributable solely to the reduction in OH- groups and that the nitrogen energy wells discussed in Chapter 4 may be equally effective in terms of impeding H_2O diffusion through the TFE as the reduction in OH- groups. Similarly, it is seen in Table 6.2 that the 0.21Zn-AlO_x displays a modest 13% reduction in OH- signal but a dramatic 82% reduction in WVTR compared to the undoped sample. This confirms that the WVTR reduction in the 0.21Zn-AlO_x is not solely attributable to the reduction in surface OH- groups and that the zinc plays an active role by reducing water corrosion and/or increasing the refractive index, as discussed in Chapter 5. However, further detailed studies are warranted to validate and confirm the extent of these contributions.

Table 6.2. Contribution of surface hydroxyl groups and nitrogen energy well in decreasing WVTR.

Samples	OH- groups (%)	WVTR g/m^2/day	O-H reduction (%)	WVTR reduction (%)
H_2O-AlO_x	29%	5.8×10^{-4}	-	-
H_2O_2-AlO_x	19%	1.7×10^{-4}	45	71
O_3-AlO_x	13%	1.5×10^{-4}	55	74
AlO_x	41%	7.8×10^{-4}	-	
0.28N-AlO_x	36%	5.7×10^{-4}	12	27
AlOx	31	7.1×10^{-4}	-	
0.21Zn-AlOx	27	1.3×10^{-4}	13	82

Perovskite solar cells characterization and stability test

To examine whether the AP-SALD/SCVD TFE deposition process affects the PSC performance, 60-nm-thick AlO_x TFE layers were deposited on p-i-n PSCs consisting of FTO/PTAA/$FA_{0.92}MA_{0.08}PbI_3$/$PC_{61}BM$/BCP/Ag in approximately 5-7 minutes using the different oxygen precursors. The J–V curves measured under simulated solar illumination in air for PSCs before and after deposition of the 60-nm H_2O-AlO_x, H_2O_2-AlO_x, and O_3-AlO_x TFE are shown in Figure FFa-c. The PCEs and FFs of the PSCs are listed inside Figure FFa-c. The J-V curves are nearly identical for PSCs encapsulated with H_2O-AlO_x and H_2O_2-AlO_x thin films in Figure FFa,b, indicating that the deposition of the TFE layer using H_2O and H_2O_2 at 130˚C had no obvious effect on the performance of the solar cells. The $FA_{0.92}MA_{0.08}PbI_3$ perovskite layer used in this study is expected to be unstable above approximately 150˚C [119]. However, after O_3-AlO_x TFE deposition, the open-circuit voltage (V_{OC}) decreased from 1.03 V to 0.98 V in Figure FFc while there was a minimal change in the FF and short circuit current (J_{SC}). This indicates that there is a possibility that the Ag electrode can be damaged by

the highly reactive ozone[197]. Ozone can react with the Ag electrode, leading to the oxidation of Ag. Previous studies have reported damage resulting from exposure to certain ALD precursors[12], which is more severe compared to SALD. The slow deposition rate of conventional ALD has limited its use for the deposition of TFE layers on PSCs due to the need for prolonged exposure steps. In contrast, the much shorter AP-SALD times used in this work allow higher deposition temperatures (e.g., 130°C) and more reactive precursors to be used without destroying the device stack[19].

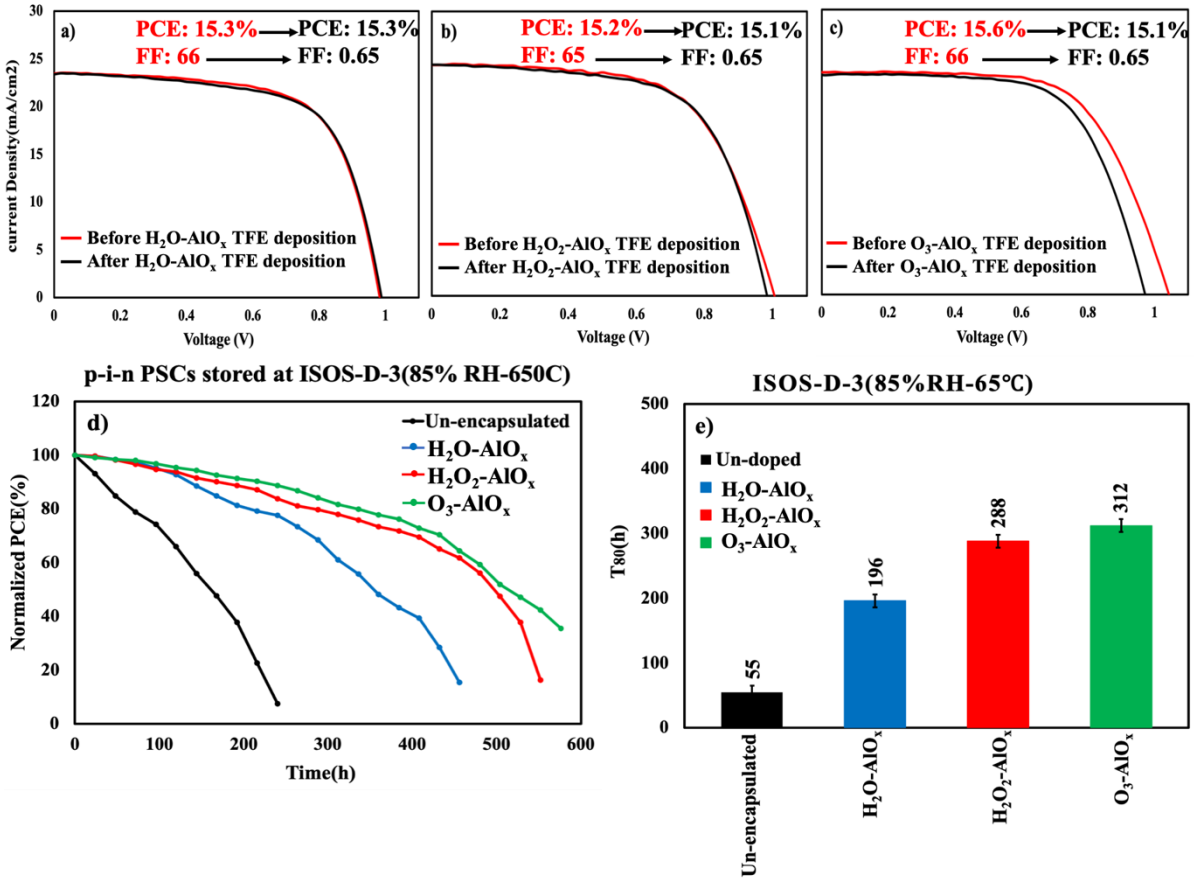

Figure FF. J–V characteristics of p-i-n structure PSCs before and after deposition of 60 nm a) H_2O-AlO_x, b) H_2O_2-AlO_x and c) O_3-AlO_x TFE. d) Normalized PCE versus time and e) T_{80} values of p-i-n PSCs encapsulated with different thin film encapsulation kept at ISOS-D-3 (65°C-85%RH).

To study the performance of the TFE layers developed in this work, p-i-n PSCs were coated with 60 nm of H_2O-AlO_x, H_2O_2-AlO_x, and O_3-AlO_x and then the encapsulated cells and control cells

without an encapsulation layer were exposed to accelerated test conditions ISOS-D-3 (dark, 65°C-85% RH)[134] and the PCEs of the cells were monitored over extended periods. Figure FFd presents the normalized PCEs as a function of time. The stability of the devices increased markedly by applying an encapsulation layer. For example, the PSC without encapsulation in Figure FFd degraded to 80% of its original efficiency in 55 h (T_{80}[134]= 55 h), due to moisture permeating into the device and causing accelerated degradation of the perovskite layer and its interface with charge transport layers[69]. In contrast, all encapsulated PSCs in Figure FFd displayed significantly longer T_{80} values greater than 196 h, as shown in Figure FFe. As in Chapter 4 and 5, the AlO_x TFE layers are expected to slow down the ingress of moisture and oxygen from the ambient and the egress of volatile species from the device. The most effective encapsulation was offered by O_3-AlO_x as the efficiency for that device reduced by just 20% over a period of 312 h. In contrast, the efficiency for the PSC encapsulated with H_2O-AlO_x decreased by 60% in 312 h. The T_{80} value for the PSC encapsulated with H_2O_2-AlO_x is comparable to that of the PSC encapsulated with O_3-AlO_x and significantly better than that of the H_2O-AlO_x-encapsulated device. This indicates that H_2O_2-AlO_x and O_3-AlO_x can effectively block moisture diffusion and provide good protection for PSCs.

Chapter 7

Nanolaminate ZnO/AlO_x TFE layers

7.1 Introduction

Both the external environment and intrinsic factors are known to contribute to PSC degradation[5], such that a combination of intrinsic stabilization and protection from the environment will be necessary to produce stable PSCs[6].

Manipulation of defective grain boundaries in polycrystalline perovskite films is crucial to maximize both the optoelectronic properties and stability of the films and the corresponding devices[198]. The grain boundaries are known to function as trap states and vulnerable spots that trigger the degradation of the materials [198]. Because metal halide perovskite films are deposited via solution processes and crystallize at low temperatures, a lot of structural defects exist along the grain boundaries, which makes them more vulnerable to heat and moisture degradation[31]. Therefore, it is crucial to minimize grain boundaries by increasing the grain size and cross-linking individual crystal grains for high stability against harsh environmental conditions[62]. There have been several attempts to use polymeric additives or cross-linking small molecular agents in the perovskite active layer as a crystal growth template or crystal cross-linker[199].

The preceding chapters have demonstrated how AlO_x TFE layers deposited using an AP-SALD system can be optimized to protect PSCs from external degradation, particularly from water vapor. However, AlO_x single-layer barriers have yet to fulfill industrial requirements due to defects and imperfections that arise during the deposition of TFE films[6]. Recently, several research studies have focused on developing a better moisture-protective film using nanolaminate films of Al_2O_3 and ZnO and/or zirconium oxide (ZrO_2)[200][114][113]. Nanolaminates are comprised of alternating layers of

different materials that have nanometer-scale thickness. A nanolaminates structure consisting of two different oxide layers exhibited superior moisture barrier properties compared with an Al_2O_3 single layer due to suppression of the formation of both microscopic voids and grain boundaries that can exist in single layers[14]. However, to date, most research was based on conventional ALD; the development of nanolaminate TFE layers for PSCs using AP-SALD is needed.

In this chapter, polystyrene (PS) is introduced into the perovskite active layer to form a cross-linked polymer-perovskite network to manipulate the nucleation and growth of the perovskite grains. PS is hydrophobic in nature and the presence of a thin layer of PS on the perovskite crystal surface could protect it from external degradation factors, such as moisture. Also, direct interaction of the PS with the perovskite significantly reduces ion migration effects[201]. Moreover, to provide additional protection, various ZnO/AlO_x nanolaminate TFE layers deposited using an AP-SALD system are investigated. The NL structure and deposition conditions are optimized to minimize the WVTR value and maximize the long-term stability of PSCs. Hence this chapter combines novel strategies to improve both the intrinsic and external stability of PSCs.

7.2 Experimental

7.2.1 AP-SALD of ZnO/AlO_x nanolaminate

Al_2O_3 and ZnO/AlO_x layers were deposited in open-air using the dual AP-SALD/SCVD system. DEZ and TMA were used as the metal precursors and hydrogen peroxide (H_2O_2) was selected as the oxidant, based on the results of Chapter 6. The TMA and DEZ bubbler flow rates were set to 25 and 50 SCCM, with nitrogen carrier flow rates of 100 and 200 SCCM, respectively, to keep a constant flow per channel of 125 SCCM. The hydrogen peroxide bubbler was set to 100 SCCM, with a nitrogen carrier flow rate of 150 SCCM. The flows from the DEZ and TMA bubblers were injected in the deposition zone through two separate channels in the reactor head as shown in Figure GGa. These

channels were controlled via independent pneumatic valves, alternating flows until a nanolaminate of the desired thickness was deposited, as can be seen in Figure GGb. The total barrier thickness was kept constant at 60 nm, while the number of stacks and the thickness of each layer was controlled by varying the number of oscillations when each of the pneumatic valves related to the DEZ and TMA precursor gases were opened. The inert nitrogen gas flow rate was set to 750 SCCM to isolate the flows of the precursors from each other and seal off the reaction zones.

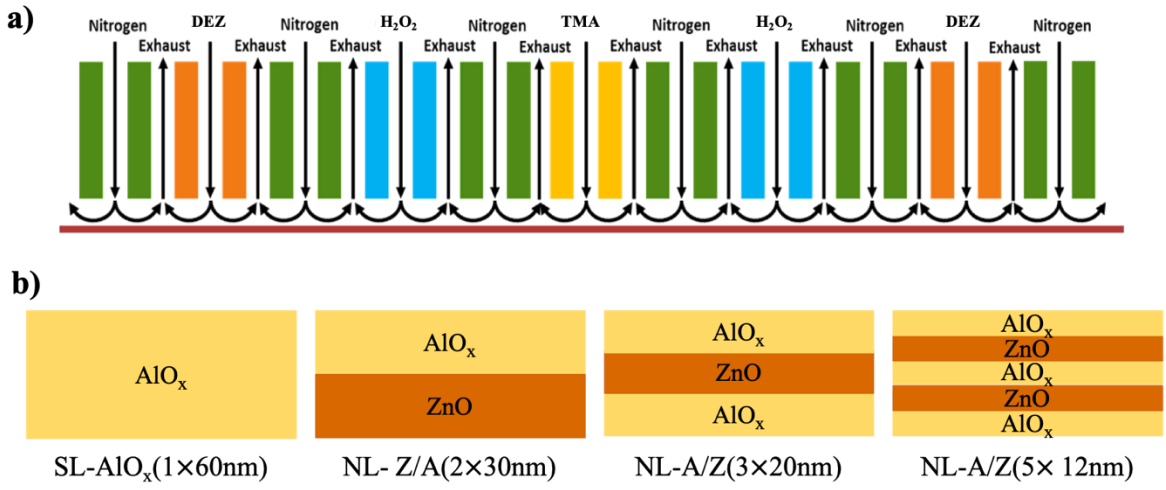

Figure GG. Scheme of a) the distribution of flows into the 21 channels of the reactor head for NL deposition, and b) fabricated ZnO/AlO_x nanolaminates with associated names.

7.2.2 PS-modified perovskite solar cells fabrication

The PS-integrated perovskite thin films were formed by a facile additive engineering approach. Specifically, 1wt% of PS was directly added into the perovskite precursor solution and the solution was spin-coated by a one-step process to form PS-integrated perovskite thin films. The n-i-p PSCs were fabricated with a structure consisting of FTO/PEDOT:PSS/PS-$MAPbI_3$/$PC_{60}BM$/BCP/Ag where PEDOT:PSS, $PC_{60}BM$, and BCP represent poly(3,4-ethylene dioxythiophene)-poly(styrene sulfonate), phenyl-C_{60}-butyric acid methyl ester, and bathocuproine, respectively. The J-V characteristics of both

the PS-modified and plain (without the addition of PS) PSCs are shown in Figure of Appendix D. A discussion of the role of PS in improving the device performance is also included in Appendix D.

7.3 Results and discussions

7.3.1 Thin film characterization

The structure of the NL layers was fixed with AlO_x as the outer layer because of the amorphous and hydrophobic nature of the AlO_x which make it a better TFE than polycrystalline ZnO, since grain boundaries in the polycrystalline structure can play a role as a permeation path in thin films [9]. Naming of the different NL configurations is presented in Figure GGb.

As mentioned, the laminated structures may affect other physical properties such as surface roughness and film density. The RMS roughness obtained from AFM images of these films is given in Figure HHa. The error bars represent the standard deviation obtained from 3 to 5 AFM images acquired from different locations on the samples. The roughness of the ZnO film is higher than that of the AlO_x film due to the ZnO crystallinity[170]. Also, the RMS values in the laminated structures gradually decreased with increasing number of layers, indicating that the NL structure has a substantial influence on the surface roughness. The NL-Z/A(2×30nm) structure has a similar roughness as the ZnO film. This suggests that the surface roughness of the underlying ZnO layer is not mitigated by the AlO_x AP-SCVD over layer, because the amorphous AlO_x thin films are very smooth and conformal to the topography of the underlying substrate, consistent with previous reports that showed that ALD Al_2O_3 could be conformally deposited on a variety of complex structures[202][203]. The RMS roughness is reduced considerably for NL-A/Z(5×12nm), getting close to the RMS roughness of the SL-AlO_x(1×60nm) thin film. The smoothing effect of the multiple AlO_x layers is attributed to the AlO_x thin films interrupting the ZnO crystal growth[204]. By limiting the thickness of the ZnO layers and hence

the size of the ZnO nanocrystals, the interposed AlO_x layers prevent the ZnO/AlO_x nanolaminate from roughening. Each new crystalline ZnO layer is forced to re-nucleate on the underlying amorphous Al_2O_3 layer[205]. The thickness of the Al_2O_3 layer needed to interrupt the ZnO crystal growth and produce the smoothing effect on the ZnO film is not clear from our results, but it was previously reported that even a 1.29 nm layer of AlO_x is effective at interrupting the growth and forcing the re-nucleation of the ZnO crystal growth, which is related to the initial interfacial reactions during AlO_x ALD on ZnO[114]. This behavior may be caused in part by a reaction where Al from the TMA exchanges with Zn on the ZnO surface. This exchange reaction would be expected to significantly disrupt the ZnO crystal growth[206]. These results suggested that surfaces of varying roughness can be fabricated by varying the interfacial density of the ZnO/AlO_x nanolaminates.

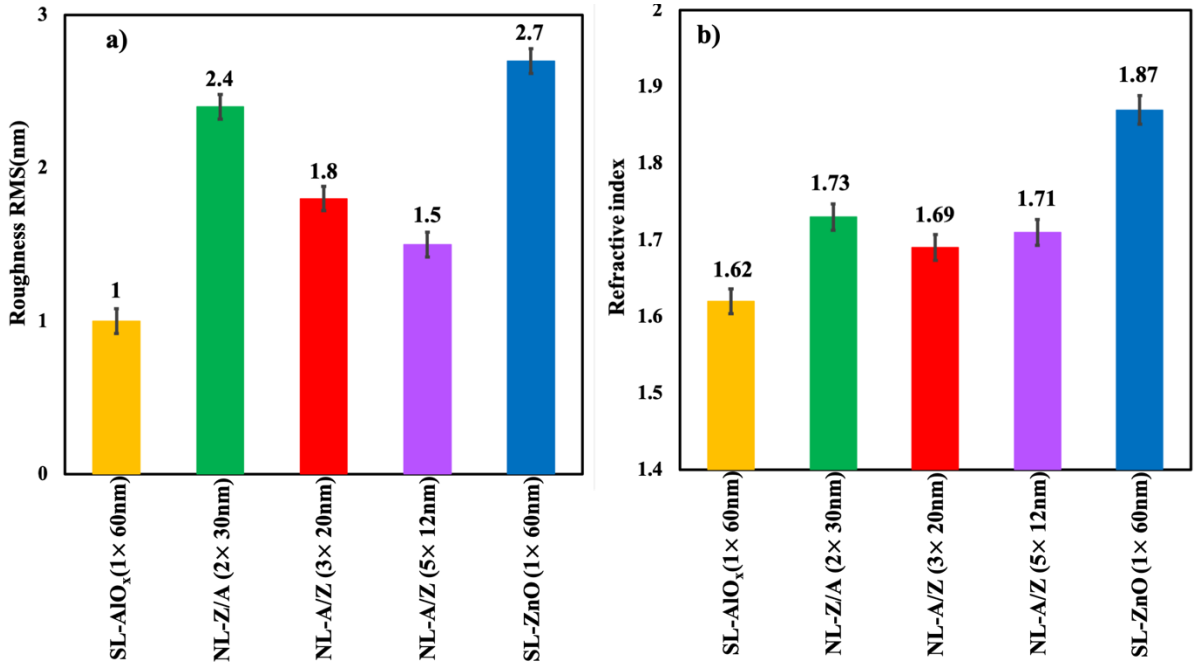

Figure HH. a) Surface roughness, and b) refractive indices of 60-nm single-layer AlO_x and ZnO, as well as different NL configurations deposited on silicon substrates using an AP-SALD system.

Figure HHb shows the refractive indexes of single-layer ZnO, AlO_x and the ZnO/AlO_x nanolaminates. The refractive indexes of single ZnO and AlO_x layers were 1.87 and 1.63, respectively,

which are in a good agreement with the refractive index reported in previous studies[207]. The refractive index of the NL structures was between 1.69 and 1.73. The refractive index of NL-Z/A(2×30nm) is higher than that of NL-A/Z(5×12nm). moreover, the refractive index increased by increasing the number of internal layers from 3 to 5. These results suggested that, the refractive index is influenced by both the number and the thickness of individual internal layers. Although the relationship between the thickness of each layer and the refractive index in ZnO/AlO_x nanolaminate films is complex and depends on various factors[207].

7.3.2 Water vapor transmission rate measurements

To evaluate the water permeability of the NL structures, WVTRs were measured using a Ca test. Single layer ZnO, AlO_x and different stacks of ZnO/AlO_x NL films with total thicknesses of 60 nm (confirmed by ellipsometry) were deposited directly on top of thermally evaporated Ca films. The encapsulated Ca films were exposed to ISOS-D-3 testing conditions[134] (65°C-85%RH) and the oxidation of the Ca films was monitored by photographic imaging during the test time.

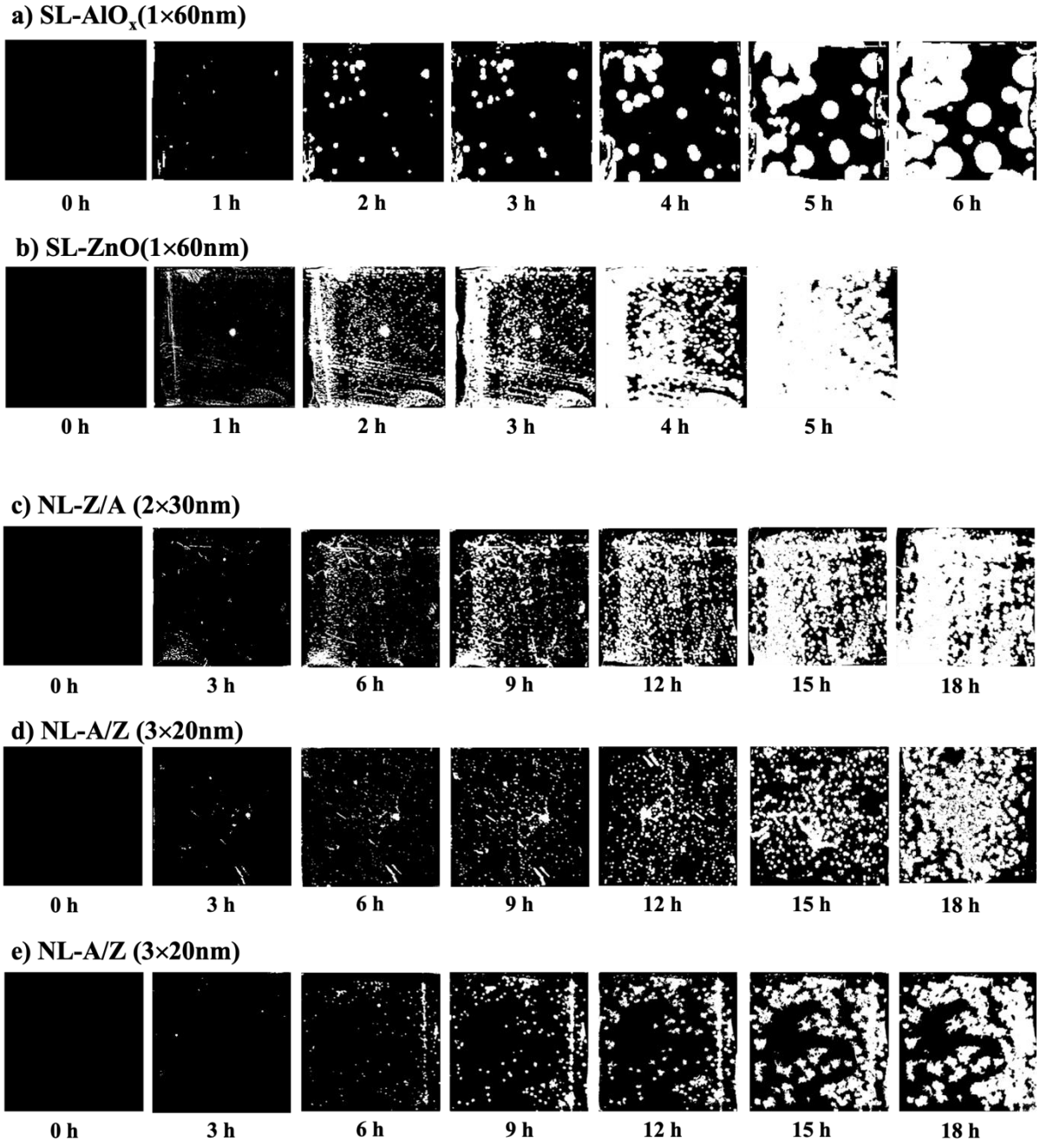

Figure II. High-contrast black-and-white images of 1.8cm×1.8cm Ca films encapsulated with a) SL-AlO_x(1×60nm), b) SL-ZnO(1×60nm), c) NL-Z/A (2×30nm), d) NL-A/Z(3×20nm) and e) NL-A/Z(5×12nm) TFE after storage in ISOS-D-3 (65˚C-85% RH) conditions for increasing time intervals.

Figure II shows the high-contrast black-and-white pictures of the encapsulated Ca films as a function of the water exposure time under acceleration conditions (65˚-85%RH) using IMAGEJ, where the white areas correspond to oxidized Ca and the metallic Ca film appears black. The WVTR values were obtained by analyzing the oxidized surface area of the Ca films[157] and are listed in Table 7.1. The time to complete oxidation of the Ca layer is also listed in Table 7.1.

The photographic images in Figure IIa,b revealed that the AlO_x single layer acted as a better moisture barrier than ZnO, consistent with the WVTR values in Table 7.1. This implies that the film crystallinity might be a more critical factor for gas-diffusion properties than film density because the moisture could diffuse into the layer more easily through grain boundaries[114]. For the 60nm-thick NL layer composed of two 30-nm-thick AlO_x and ZnO layers, the time to complete oxidation of the Ca layer was almost double that for the pure AlO_x layer (Table 7.1).

As shown in Table 7.1, the WVTR values are on the order of 10^{-5} g/m^2/day at 65˚C-85% RH, indicating that all of the ZnO/AlO_x NLs are good barriers to water-vapor permeation. Interestingly, the time to complete oxidation of the Ca layer increased and the WVTR values decreased with increasing number of layers, indicating that the adjustment of the ZnO/AlO_x laminated structure affects the WVTR values and improves the gas diffusion barrier property.

Table 7.1. a) WVTR values and b) time to complete oxidation of the Ca layer for the 60-nm-thick single-layer and nanolaminate TFE deposited using the AP-SALD system and stored at ISOS-D-3 (65˚C-85% RH).

TFE	WVTR (g/m^2/day) ISOS-D-3 (65˚C-85% RH)	Time to complete oxidation(h)
SL-AlO_x (1×60nm)	1.7×10^{-4}	12
SL-ZnO (1×60nm)	4.3×10^{-4}	5
NL-Z/A(2×30nm)	8.7×10^{-5}	23
NL-A/Z(3×20nm)	6.3×10^{-5}	30
NL-A/Z (5×12nm)	5.1×10^{-5}	38

The NL structures likely produced lower WVTR values compared to the single layer AlO_x due to mismatch of permeation paths or channels between the layers. Generally, water-vapor permeation through an encapsulation layer occurs by pinhole-related transport and H_2O permeating along chains of chemical defect clusters like OH- defects[158]. These mechanisms are possible because defects such as pinholes or OH- groups in the layer are connected and form a channel or path that links the outside and inside for moisture[157] [76]. These paths are more likely to be formed in a single layer. Figure JJa illustrates this permeation path in a single-layer encapsulation thin film. Alternatively, in a NL structure, defects in the individual layers are not necessarily connected to form a full path or channel through the TFE, as shown in Figure JJb. The defects located in each layer become mismatched because each layer has different physical properties such as crystallinity, density, and roughness. Hence a full connection from the inner layer to the outside atmosphere is not produced. The lower WVTRs in the NL structure compared with the single layers support the idea that the NL provides unique and improved film properties as a gas diffusion barrier through manipulation of the physical properties of the layers. In terms of permeability mechanisms, the NL structures may also minimize cracks, grain boundaries and pinhole defects in the inorganic films [7].

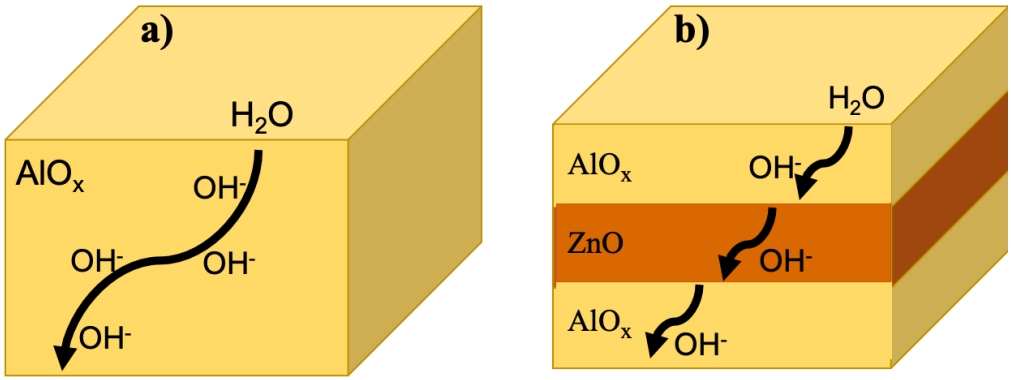

Figure JJ. Water permeation mechanism via channels formed by defects in a a) single-layer, and b) nanolaminate structure.

7.3.3 Perovskite solar cells characterization and stability test

To study the performance of the single and NL encapsulation layers, 60-nm-thick TFE were deposited on a p-i-n PSC structure consisting of FTO/PEDOT:PSS/$MAPbI_3$(or PS-$MAPbI_3$)/$PC_{60}BM$/BCP/Ag. The encapsulated cells and control cells without an encapsulation layer were exposed to accelerated test condition ISOS-D-3 (dark, 65°C-85% RH)[134] and the PCEs of the cells were monitored over extended periods. The normalized PCEs for PSCs without and with PS modification are shown in Figure KKa and b, respectively. It can be seen in Figure KKa,b that the stability of the devices increased markedly by applying an encapsulation layer. For example, the plain PSC without encapsulation in Figure KKa degraded to 80% of its original efficiency in 38 h (T_{80}= 38 h)[134]. In contrast, all encapsulated PSCs in Figure KKa displayed T_{80} values greater than 150 h. The single-layer AlOx TFE was better than the single-layer ZnO, due to the amorphous nature of AlO_x compared to ZnO, consistent with the WVTR values in Table 7.1

It is observed in Figure KKb that the devices with PS-modified perovskite showed better stability than those with a plain perovskite active layer. The un-encapsulated plain PSC showed a T_{80} value of 38 h, whereas for the un-encapsulated PS-modified PSC, the T_{80} value was 77 h. This is attributed to the hydrophobic PS that could be present on the surface of the perovskite layer, which retards the penetration of moisture into the crystal and thus prevents $MAPbI_3$ decomposition[201]. The PS hence has the dual role of both modulating the crystallization process leading to the formation of high-quality crystals (Figure , Appendix D) and at the same time also acting as a thin surface coating that protects against degradation.

Figure KKc shows the T_{80} values of the p-i-n PSCs with the various TFE layers kept at ISOS-D-3 condition. It is observed that the devices with NL-A/Z(5×12nm) TFE showed best stability (T_{80}=536 h), consistent with the lowest WVTR values. Therefore, the ZnO/AlO_x NL TFE significantly

improved the stability of the PSCs by decreasing the WVTR value, which is attributed to the mismatch of permeation paths or channels between the various layers with different physical properties.

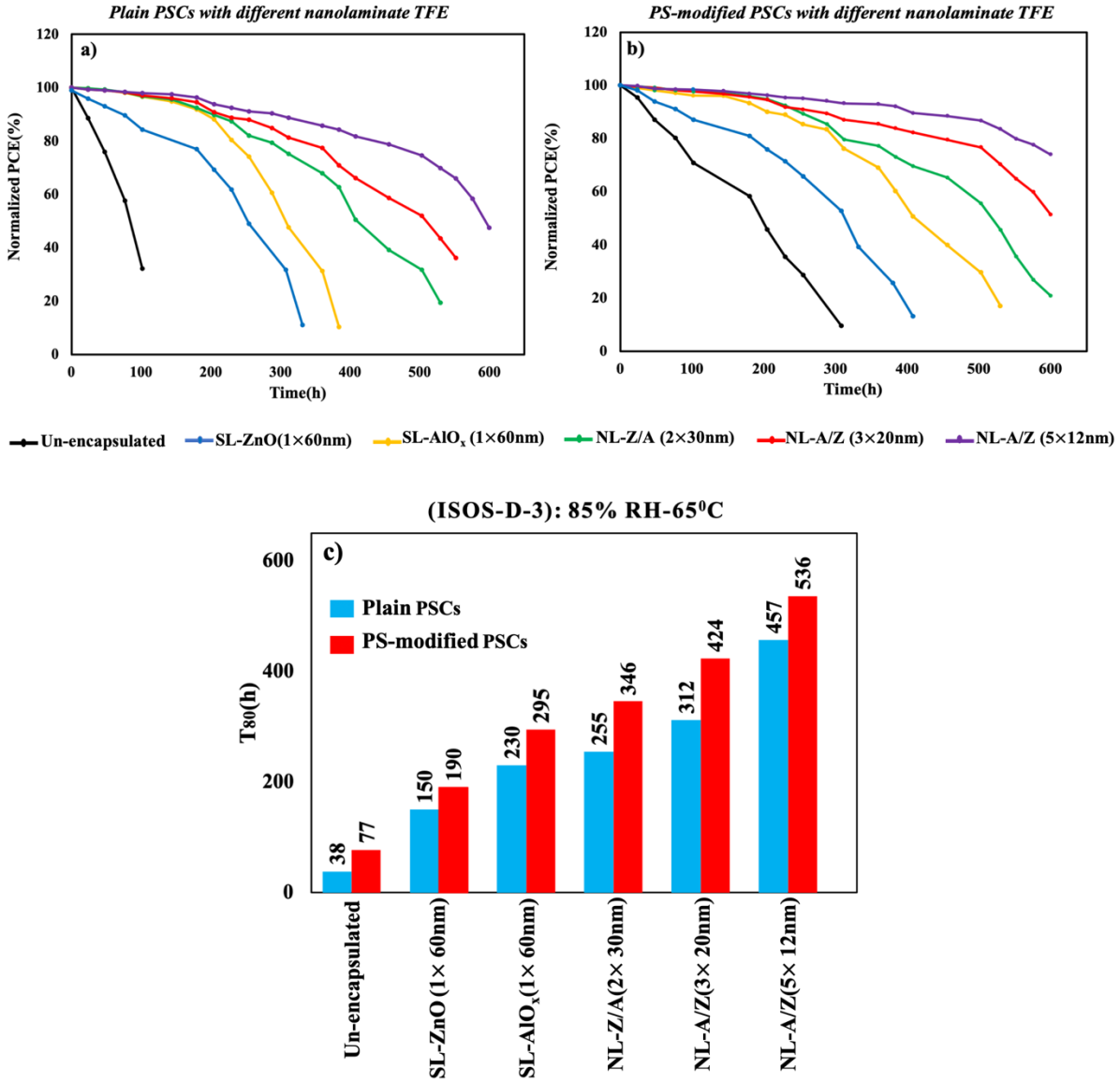

Figure KK. Normalized PCE versus time for a) plain PSCs, b) PS-modified PSCs and c) T_{80} values of the plain and PS-modified PSCs encapsulated with different ZnO/AlO_x NL TFE layers kept at ISOS-D-3 (65˚C-85%RH) conditions.

In the NL TFE layers, increasing the number of AlO_x and ZnO layers makes the encapsulation more effective at preventing moisture from penetrating the surface through the solar cells' active layers. Moreover, we can conclude that the addition of PS leads to improved crystallinity, stability, and larger grain size. Combining the improved internal stability with external encapsulation to protect PSCs from environmental degradation could result in outstanding long-term stability, even at harsh environmental conditions. But further optimization of the NL structure is warranted and more work should be done to increase the efficiency of the PS-modified PSCs and include PS in other perovskite compositions like $FA_{0.92}MA_{0.08}PbI_3$.

Chapter 8

Conclusion

This thesis has presented several novel TFE strategies to improve the stability of PSCs under harsh environmental conditions such as high humidity and elevated temperature.

In Chapter 4, nitrogen-doped AlO_x thin films with different nitrogen concentration were produced by AP-SCVD. The N-AlO_x thin-film growth rate was slightly higher than for AlO_x due to the larger nitrogen ion. The GPCs were observed to be around 0.31 nm/cycle for AlO_x and 0.41 nm/cycle for N-AlO_x, providing precise control over film thickness. The N-AlO_x films also showed higher refractive indexes than AlO_x films, indicating an increased film density that is associated with an improved film quality. Introducing nitrogen also reduced the RMS roughness to below 0.88 nm, compared with 0.96 nm for the AlO_x film. XPS showed that the nitrogen bonded to the aluminum and N-doping suppressed formation of oxygen-related defects, such as residual O-H groups. Both AlO_x and N-AlO_x films showed an outstanding barrier property with a WVTR on the order of 10^{-5} and 10^{-4} g m^{-2} d^{-1} at accelerated conditions of 25°C-55% RH and 65°C-85% RH, respectively. The N-AlO_x showed lower WVTR values due to the lower concentration of OH- defects on the film surfaces, since water vapor transmission through thin films occurs by permeation of H_2O molecules along chains of chemical defect clusters like OH- groups. When the TFE was applied to PSCs, XRD analysis of the perovskite layer before and after encapsulation showed no significant changes in the perovskite structure, indicating that the rapid nature of the AP-SCVD technique enabled deposition of the TFE without causing degradation of the heat-sensitive materials used for PSC fabrication, i.e. perovskite and Spiro-OMeTAD. Thus, we expect that the developed TFE layers will be applicable to other PSC configurations and temperature-sensitive applications. PSCs with n-i-p and p-i-n structures were studied and the p-i-n devices were slightly more stable due to the poor stability of spiro-MeOTAD in

the n-i-p PSC and hydrophobic nature of the PCBM in p-i-n PSCs. A p-i-n PSC encapsulated with a 0.28N-AlO_x TFE maintained 80% of its initial PCE after exposure to 25°C-55% RH for 855 h whereas an un-encapsulated device was only stable for 144 hrs. For testing at 65°C-85% RH, the T_{80} values of the p-i-n PSCs increased from 53 h to 300 h with the addition of the 0.28N-AlO_x TFE. The optimal Zn concentration was approximately 0.28 at%. The N-rich sites can likely trap water molecules and hinder their diffusion, but higher N-content may facilitate multilayer adsorption of water and permeation pathways, driven by a high concentration of trapping sites. Therefore, the key requirement to produce better barrier layers is to increase the density of the coatings and reduce the number of water diffusion pathways by optimizing the concentration of nitrogen.

In Chapter 5, Zn-doped AlO_x TFE were investigated. GPCs were approximately 0.34-0.38 nm/cycle for different Zn-AlO_x compositions, the slight difference between the measured GPC and the linear combination of the GPCs of each binary oxide was likely due to some DEZ etching. However, it was shown that the co-injection of the metal precursors allows for good control of the film thickness and composition. As for the nitrogen-doping, increasing the Zn concentration increased the refractive index and decreased the O-H content. However, as the Zn/Al ratio increased beyond 0.21, excess Zn atoms appeared to segregate, which could interact with adsorbed water molecules to form Zn-OH species, leading to an increase in the number of available hydroxyl groups on the surface of the deposited film.

The formation of ZnO at the higher doping levels was confirmed by XRD and seen as some small bumps in AFM. The roughness increased gradually with zinc concentration; however, the roughness of all Zn-AlO_x films was close to that of the Al_2O_3 (0.94 nm), as the films grown at these low DEZ flow rates are mainly composed of amorphous Al_2O_3. The WVTR decreased by increasing the Zn/Al up to 0.21 but adding more zinc (Zn/Al of 0.29) increased the WVTR slightly, which could

be related to the increased OH content and possible Zn segregation. By carefully controlling the Zn concentration, it was possible to achieve an optimal balance and minimize the WVTR (10^{-4} g/m^2/day at 65°C-85%RH for Zn/Al=0.21). p-i-n PSCs with the 0.21Zn-AlO_x TFE showed an average T_{80} value of 384h at 65°C-85% RH, higher than that obtained with N-doping, which was attributed to the Zn-doping improving the film compactness and reducing the fraction of hydroxyl groups on the film surface.

In Chapter 6, the effect of different oxidants (H_2O, H_2O_2, and O_3) on the AlO_x TFE deposited by AP-SCVD was systematically investigated. At identical process conditions, H_2O-AlO_x thin films showed the highest growth rate (GPC=0.35 nm/cycle) followed by H_2O_2-AlO_x (GPC=0.30 nm/cylce) and O_3-AlO_x (GPC=0.26 nm/cycle). The high GPC observed for H_2O-AlO_x, as compared to more reactive oxidants like H_2O_2 or O_3, could be due to multilayer water condensation on the substrate surface at low deposition temperatures. Replacing water with the more reactive oxidants H_2O_2 and O_3 increased the refractive index, indicating an increased film density, and reduced the RMS roughness to 0.93 and 0.76 nm, respectively, compared with 1.02 nm for the H_2O-AlO_x film. The more reactive oxidants result in completed surface reactions that reduces the number of surface hydroxyl groups and carbon contaminants. WVTR values on the order of 10^{-4} g/m^2/day at 65°C-85% RH were measured and the WVTR values decreased by using the more reactive oxidants, which was attributed to the lower concentration of OH- defects. When applied to p-i-n PSCs, deposition of the TFE layer using H_2O and H_2O_2 at 130°C had no obvious effect on the cell performance of the solar cells. However, the O_3-AlO_x TFE deposition caused a slight decrease in the V_{OC}, indicating that the Ag electrode may be damaged by exposure to the highly reactive ozone. The most effective encapsulation was offered by the O_3-AlO_x as the efficiency for that device reduced by just 20% over a period of 312 h at 65°C-85% RH. However, the T_{80} value for the PSC encapsulated with H_2O_2-AlO_x was comparable (288 h) and significantly better than the H_2O-AlO_x-encapsulated device. This indicates that both H_2O_2-AlO_x and O_3-AlO_x provided

good protection but H_2O_2 did not cause significant damage. Overall, the H_2O_2-AlO_x has an ultralow WVTR value (e.g., 1.7×10^{-4} g/m^2/day in ISOS-D-3 conditions) and may be a more practical and effective choice due to its good barrier performance, compatibility with the perovskite layer, and commercial availability.

In Chapter 7, both the intrinsic and extrinsic stability of a PSC was improved by fabricating PS-modified perovskite films with a facile additive-engineering approach. Also, ZnO/AlO_x nanolaminate TFE were deposited by AP-SCVD to protect the PSCs. The total barrier thickness was kept constant at 60 nm, while the number of stacks and the thickness of each layer was varied. RMS roughness in the laminated structures gradually decreased with the number of layers, which was attributed to the AlO_x thin film interrupting the ZnO crystal growth. The refractive index of the NL structures was between the refractive index of each binary oxide. WVTR tests revealed that single-layer AlO_x was a better moisture barrier than ZnO, suggesting that a critical factor for gas diffusion properties might be the film crystallinity rather than film density. WVTR values were on the order of 10^{-5} g/m^2/day at 65°C-85% RH for the ZnO/AlO_x nanolaminates and decreased with increasing number of layers, which was attributed to mismatch of the permeation paths or channels between the various layers. The defects in each layer that provide moisture permeation pathways become mismatched because each layer has different properties such as crystallinity, density, and roughness. PSCs with PS-modified perovskite showed better stability than those with plain perovskite, which was attributed to hydrophobic PS that is expected to be present on the surface of the perovskite layer. The T_{80} value of PS-modified PSCs with NL-A/Z(5×12nm) kept at ISOS-D-3 condition reached 536h, which is the highest stability reported in this thesis. Combining the improvement in internal stability with external encapsulation resulted in an outstanding long-term stability under harsh environmental conditions.

A summary of previous reports on TFEs can be found in Table 2.2, highlighting the perovskite device structure, encapsulation materials and the stability performance. However, inconsistency in testing conditions and parameters reported in previous studies make direct comparisons challenging. Moreover, a variety of perovskite materials and device architectures have been studied which further complicates the comparison. Nonetheless, it is seen that the WVTR values measured for the TFE layers (e.g., 5.1×10^{-5}g/m^2/day in ISOS-D-3 conditions for the NL-A/Z(5×12nm)) are similar or less than previous reports and the T_{80} values (e.g., 536 h in ISOS-D-3 conditions for the NL-A/Z(5×12nm)) are also very promising. Importantly, these TFE layers were deposited using a roll-to-roll-compatible atmospheric process, which is much faster than previous vacuum ALD methods.

This thesis confirms that the deposition of AlO_x using an AP-SALD system and the incorporation of different dopants and oxidants can produce promising single-layer TFE that is effective in preventing moisture ingress and improving the stability of PSCs. However, the fact that the PV performance still degrades over time indicates that more progress is needed to develop encapsulating materials for commercial application. Further combination of developed strategies in this thesis could be conducted to further enhance TFEs moisture barrier properties and PSCs stability over time. Additionally, the long-term stability and reliability of the PSCs could be evaluated under different environmental conditions to better understand the performance of the encapsulating materials and identify any areas for improvement. Furthermore, the potential for scaling up the manufacturing process of these TFE for both large-scale commercial production and flexible devices could be explored. Overall, there is significant potential for future research to build upon the findings of this thesis and further advance the field of TFEs for PSCs. To this end, the following suggestions are provided:

- Combining nitrogen and zinc doping
- A NL structure that incorporates doped AlO_x

- Investigate different nanolaminate structure
- Organic-inorganic nanolaminates structure can be another interesting TFE for PSCs.
- Different techniques to clean the PSCs before encapsulation could be investigates since the WVTR studies indicates that some contaminants may be present (e.g., on the surface of the Ca film) that prevent complete coverage, providing early permeation pathways

References

[1] R. Wang, M. Mujahid, Y. Duan, Z. K. Wang, J. Xue, and Y. Yang, "A Review of Perovskites Solar Cell Stability," *Adv. Funct. Mater.*, vol. 1808843, pp. 1–25, 2019.

[2] M. Kim *et al.*, "Conformal quantum dot-SnO2 layers as electron transporters for efficient perovskite solar cells," *Science (80-.).*, vol. 375, no. 6578, pp. 302–306, 2022.

[3] L. Duan and A. Uddin, "Defects and stability of perovskite solar cells: A critical analysis," *Mater. Chem. Front.*, vol. 6, no. 4, pp. 400–417, 2022.

[4] H. Wang, H. Liu, W. Li, L. Zhu, and H. Chen, "Inorganic perovskite solar cells based on carbon electrodes," *Nano Energy*, vol. 77, no. May, 2020.

[5] T. A. Berhe *et al.*, "Organometal halide perovskite solar cells: Degradation and stability," *Energy Environ. Sci.*, vol. 9, no. 2, pp. 323–356, 2016.

[6] K. Lochhead, E. Johlin, and D. Yang, "Encapsulation of Perovskite Solar Cells with Thin Barrier Films," in *Thin Film Deposition-Fundamentals, Processes, and Applications*, 2022.

[7] C. C. Boyd, R. Cheacharoen, T. Leijtens, and M. D. McGehee, "Understanding Degradation Mechanisms and Improving Stability of Perovskite Photovoltaics," *Chem. Rev.*, vol. 119, no. 5, pp. 3418–3451, 2019.

[8] M. Kim *et al.*, "Moisture resistance in perovskite solar cells attributed to a water-splitting layer," *Commun. Mater.*, vol. 2, no. 1, pp. 1–12, 2021.

[9] A. Uddin, M. B. Upama, H. Yi, and L. Duan, "Encapsulation of organic and perovskite solar cells: A review," *Coatings*, vol. 9, no. 2, pp. 1–17, 2019.

[10] F. Li and M. Liu, "Recent efficient strategies for improving the moisture stability of perovskite solar cells," *J. Mater. Chem. A*, vol. 5, no. 30, pp. 15447–15459, 2017.

[11] R. K. Raman, S. A. Gurusamy Thangavelu, S. Venkataraj, and A. Krishnamoorthy, "Materials, methods and strategies for encapsulation of perovskite solar cells: From past to present," *Renew. Sustain. Energy Rev.*, vol. 151, no. August, 2021.

[12] Y. Il Lee *et al.*, "A Low-Temperature Thin-Film Encapsulation for Enhanced Stability of a Highly Efficient Perovskite Solar Cell," *Adv. Energy Mater.*, vol. 8, no. 9, pp. 1–8, 2018.

[13] B. J. Kim, D. Han, S. Yoo, and S. G. Im, "Organic/inorganic multilayer thin film encapsulation via initiated chemical vapor deposition and atomic layer deposition for its application to organic solar cells," *Korean J. Chem. Eng.*, vol. 34, no. 3, pp. 892–897, 2017.

[14] M. H. Tseng *et al.*, "Low-temperature gas-barrier films by atomic layer deposition for encapsulating organic light-emitting diodes," *Nanotechnology*, vol. 27, no. 29, 2016.

[15] S. E. Potts, W. Keuning, E. Langereis, G. Dingemans, M. C. M. van de Sanden, and W. M. M. Kessels, "Low Temperature Plasma-Enhanced Atomic Layer Deposition of Metal Oxide Thin Films," *J. Electrochem. Soc.*, vol. 157, no. 7, p. P66, 2010.

[16] D. Muñoz-Rojas, V. H. Nguyen, C. Masse de la Huerta, S. Aghazadehchors, C. Jiménez, and D. Bellet, “Spatial Atomic Layer Deposition (SALD), an emerging tool for energy materials. Application to new-generation photovoltaic devices and transparent conductive materials,” *Comptes Rendus Phys.*, vol. 18, no. 7–8, pp. 391–400, 2017.

[17] R. L. Z. Hoye *et al.*, “Research Update: Atmospheric pressure spatial atomic layer deposition of ZnO thin films: Reactors, doping, and devices,” *APL Mater.*, vol. 3, no. 4, 2015.

[18] D. Muñoz-Rojas and J. Macmanus-Driscoll, “Spatial atmospheric atomic layer deposition: A new laboratory and industrial tool for low-cost photovoltaics,” *Mater. Horizons*, vol. 1, no. 3, pp. 314–320, 2014.

[19] P. Poodt *et al.*, “Spatial atomic layer deposition: A route towards further industrialization of atomic layer deposition,” *J. Vac. Sci. Technol. A Vacuum, Surfaces, Film.*, vol. 30, no. 1, p. 010802, 2012.

[20] V. Zardetto *et al.*, “Atomic layer deposition for perovskite solar cells: Research status, opportunities and challenges,” *Sustain. Energy Fuels*, vol. 1, no. 1, pp. 30–55, 2017.

[21] R. D. Raninga *et al.*, “Strong performance enhancement in lead-halide perovskite solar cells through rapid, atmospheric deposition of n-type buffer layer oxides,” *Nano Energy*, vol. 75, no. January, 2020.

[22] R. L. Z. Hoye *et al.*, “Enhanced performance in fluorene-free organometal halide perovskite light-emitting diodes using tunable, low electron affinity oxide electron injectors,” *Adv. Mater.*, vol. 27, no. 8, pp. 1414–1419, 2015.

[23] L. Hoffmann *et al.*, “Spatial Atmospheric Pressure Atomic Layer Deposition of Tin Oxide as an Impermeable Electron Extraction Layer for Perovskite Solar Cells with Enhanced Thermal Stability,” *ACS Appl. Mater. Interfaces*, vol. 10, no. 6, pp. 6006–6013, 2018.

[24] X. Dong *et al.*, “Improvement of the humidity stability of organic-inorganic perovskite solar cells using ultrathin Al_2O_3 layers prepared by atomic layer deposition,” *J. Mater. Chem. A*, vol. 3, no. 10, pp. 5360–5367, 2015.

[25] V. Vandalon and W. M. M. Kessels, “What is limiting low-temperature atomic layer deposition of Al_2O_3? A vibrational sum-frequency generation study,” *Appl. Phys. Lett.*, vol. 108, no. 1, pp. 1–6, 2016.

[26] A. H. Alshehri *et al.*, “Nanoscale Film Thickness Gradients Printed in Open Air by Spatially Varying Chemical Vapor Deposition,” *Adv. Funct. Mater.*, vol. 31, no. 31, pp. 1–14, 2021.

[27] D. B. A Mitzi, “Synthesis, Structure, and Properties of Organic-Inorganic Perovskites and Related Materials,” in *Progress in Inorganic Chemistry*, 2007, pp. 1–121.

[28] T. Leijtens, G. E. Eperon, S. Pathak, A. Abate, M. M. Lee, and H. J. Snaith, “Overcoming ultraviolet light instability of sensitized TiO_2 with meso-superstructured organometal tri-halide perovskite solar cells,” *Nat. Commun.*, vol. 4, pp. 1–8, 2013.

[29] T. Leijtens, G. E. Eperon, N. K. Noel, S. N. Habisreutinger, A. Petrozza, and H. J. Snaith, "Stability of metal halide perovskite solar cells," *Adv. Energy Mater.*, vol. 5, no. 20, pp. 1–23, 2015.

[30] Y. Yuan, R. Xu, H. T. Xu, F. Hong, F. Xu, and L. J. Wang, "Nature of the band gap of halide perovskites ABX_3 (A = CH_3NH_3, Cs; B = Sn, Pb; X = Cl, Br, I): First-principles calculations," *Chinese Phys. B*, vol. 24, no. 11, pp. 0–5, 2015.

[31] R. Sharma, A. Sharma, S. Agarwal, and M. S. Dhaka, "Stability and efficiency issues, solutions and advancements in perovskite solar cells: A review," *Sol. Energy*, vol. 244, no. April, pp. 516–535, 2022.

[32] Z. Shi and A. H. Jayatissa, "Perovskites-based solar cells: A review of recent progress, materials and processing methods," *Materials (Basel).*, vol. 11, no. 5, 2018.

[33] A. Kojima, K. Teshima, Y. Shirai, and T. Miyasaka, "Organometal Halide Perovskites as Visible-Light Sensitizers for Photovoltaic Cells," *J. Am. Chem. Soc.*, vol. 131, no. 17, pp. 6050–6051, Apr. 2009.

[34] Michael M. Lee, J. Teuscher, T. Miyasaka, T. N. Murakami, and H. J. Snaith, "Efficient Hybrid Solar Cells Based on Meso-superstructured organometal halide perovskite ," *Science (80-.).*, vol. 338, no. November, pp. 643–647, 2012.

[35] B. J. Kim, S. Lee, and H. S. Jung, "Recent progressive efforts in perovskite solar cells toward commercialization," *J. Mater. Chem. A*, vol. 6, no. 26, pp. 12215–12236, 2018.

[36] H. J. Snaith *et al.*, "Hysteresis in perovskite solar cells," *J Phys Chem Lett*, vol. 5, pp. 1511–1515, 2014.

[37] D. Wang, M. Wright, N. K. Elumalai, and A. Uddin, "Stability of perovskite solar cells," *Sol. Energy Mater. Sol. Cells*, vol. 147, pp. 255–275, 2016.

[38] L. K. Ono, Y. Qi, and S. (Frank) Liu, "Progress toward Stable Lead Halide Perovskite Solar Cells," *Joule*, vol. 2, no. 10, pp. 1961–1990, 2018.

[39] Z. Yu and L. Sun, "Recent Progress on Hole-Transporting Materials for Emerging Organometal Halide Perovskite Solar Cells," *Adv. Energy Mater.*, vol. 5, no. 12, 2015.

[40] Z. Song, S. C. Watthage, A. B. Phillips, and M. J. Heben, "Pathways toward high-performance perovskite solar cells: review of recent advances in organo-metal halide perovskites for photovoltaic applications," *J. Photonics Energy*, vol. 6, no. 2, p. 022001, 2016.

[41] M. Lee, Y. Jo, D. S. Kim, and Y. Jun, "Flexible organo-metal halide perovskite solar cells on a Ti metal substrate," *J. Mater. Chem. A*, vol. 3, no. 8, pp. 4129–4133, 2015.

[42] D. Zhou, T. Zhou, Y. Tian, X. Zhu, and Y. Tu, "Perovskite-Based Solar Cells: Materials, Methods, and Future Perspectives," *J. Nanomater.*, vol. 2018, 2018.

[43] S. D. Stranks *et al.*, "Electron-Hole Diffusion Lengths Exceeding," vol. 342, no. October, pp.

341–345, 2013.

[44] N. G. Park, “Organometal perovskite light absorbers toward a 20% efficiency low-cost solid-state mesoscopic solar cell,” *J. Phys. Chem. Lett.*, vol. 4, no. 15, pp. 2423–2429, 2013.

[45] N. H. Tiep, Z. Ku, and H. J. Fan, “Recent Advances in Improving the Stability of Perovskite Solar Cells,” *Adv. Energy Mater.*, vol. 6, no. 3, pp. 1–19, 2016.

[46] S. N. Habisreutinger, T. Leijtens, G. E. Eperon, S. D. Stranks, R. J. Nicholas, and H. J. Snaith, “Carbon Nanotube/Polymer Composites as a Highly Stable Hole Collection Layer in Perovskite Solar Cells,” *Nano Lett.*, vol. 14, no. 10, pp. 5561–5568, Sep. 2014.

[47] J. M. Frost, K. T. Butler, F. Brivio, C. H. Hendon, M. Van Schilfgaarde, and A. Walsh, “Atomistic origins of high-performance in hybrid halide perovskite solar cells,” *Nano Lett.*, vol. 14, no. 5, pp. 2584–2590, 2014.

[48] N. J. Jeon *et al.*, “Compositional engineering of perovskite materials for high-performance solar cells,” *Nature*, vol. 517, no. 7535, pp. 476–480, 2015.

[49] J. Troughton, N. Gasparini, and D. Baran, “$Cs_{0.15}FA_{0.85}PbI_3$ perovskite solar cells for concentrator photovoltaic applications,” *J. Mater. Chem. A*, vol. 6, no. 44, pp. 21913–21917, 2018.

[50] G. Niu, X. Guo, and L. Wang, “Review of recent progress in chemical stability of perovskite solar cells,” *J. Mater. Chem. A*, vol. 3, no. 17, pp. 8970–8980, 2015.

[51] S. Ito, S. Tanaka, K. Manabe, and H. Nishino, “Effects of Surface Blocking Layer of Sb_2S_3 on Nanocrystalline TiO_2 for $CH_3NH_3PbI_3$ Perovskite Solar Cells,” *J. Phys. Chem. C*, vol. 118, no. 30, pp. 16995–17000, May 2014.

[52] T. T. Ava, A. Al Mamun, S. Marsillac, and G. Namkoong, “A review: Thermal stability of methylammonium lead halide based perovskite solar cells,” *Appl. Sci.*, vol. 9, no. 1, 2019.

[53] H. Choi *et al.*, “Cesium-doped methylammonium lead iodide perovskite light absorber for hybrid solar cells,” *Nano Energy*, 2014.

[54] J. W. Lee, D. H. Kim, H. S. Kim, S. W. Seo, S. M. Cho, and N. G. Park, “Formamidinium and cesium hybridization for photo- and moisture-stable perovskite solar cell,” *Adv. Energy Mater.*, vol. 5, no. 20, 2015.

[55] Z. Hawash, L. K. Ono, and Y. Qi, “Moisture and Oxygen Enhance Conductivity of LiTFSI-Doped Spiro-MeOTAD Hole Transport Layer in Perovskite Solar Cells,” *Adv. Mater. Interfaces*, vol. 3, no. 13, pp. 1–6, 2016.

[56] Y. Kato, L. K. Ono, M. V. Lee, S. Wang, S. R. Raga, and Y. Qi, “Silver Iodide Formation in Methyl Ammonium Lead Iodide Perovskite Solar Cells with Silver Top Electrodes,” *Adv. Mater. Interfaces*, vol. 2, no. 13, pp. 2–7, 2015.

[57] L. Zhang *et al.*, “The effect of carbon counter electrodes on fully printable mesoscopic

perovskite solar cells," *J. Mater. Chem. A*, vol. 3, no. 17, pp. 9165–9170, 2015.

[58] G. E. Eperon, S. D. Stranks, C. Menelaou, M. B. Johnston, L. M. Herz, and H. J. Snaith, "Formamidinium lead trihalide: A broadly tunable perovskite for efficient planar heterojunction solar cells," *Energy Environ. Sci.*, vol. 7, no. 3, pp. 982–988, 2014.

[59] X. Li *et al.*, "Improved performance and stability of perovskite solar cells by crystal crosslinking with alkylphosphonic acid ω -ammonium chlorides," *Nat. Chem.*, vol. 7, no. 9, pp. 703–711, 2015.

[60] S. Yang, Y. Wang, P. Liu, Y. B. Cheng, H. J. Zhao, and H. G. Yang, "Functionalization of perovskite thin films with moisture-tolerant molecules," *Nat. Energy*, vol. 1, no. 2, pp. 1–7, 2016.

[61] J. W. Rumer and I. McCulloch, "Organic photovoltaics: Crosslinking for optimal morphology and stability," *Mater. Today*, vol. 18, no. 8, pp. 425–435, 2015.

[62] R. Saraf and V. Maheshwari, "PbI_2 Initiated Cross-Linking and Integration of a Polymer Matrix with Perovskite Films: 1000 h Operational Devices under Ambient Humidity and Atmosphere and with Direct Solar Illumination," *ACS Appl. Energy Mater.*, vol. 2, no. 3, pp. 2214–2222, 2019.

[63] G. Grancini *et al.*, "One-Year stable perovskite solar cells by 2D/3D interface engineering," *Nat. Commun.*, vol. 8, pp. 1–8, 2017.

[64] S. H. K. Park, J. Oh, C. S. Hwang, Y. S. Yang, J. I. Lee, and H. Y. Chu, "Ultra thin film encapsulation of OLED on plastic substrate," *J. Inf. Disp.*, vol. 5, no. 3, pp. 30–34, 2004.

[65] J. Ahmad, K. Bazaka, L. J. Anderson, R. D. White, and M. V. Jacob, "Materials and methods for encapsulation of OPV: A review," *Renew. Sustain. Energy Rev.*, vol. 27, pp. 104–117, 2013.

[66] kue tradisional khas Aceh, "Silicones for photovoltaic encapsulation," in *European Photovoltaic Solar Energy Conference*, 2008, vol. 1, no. 23rd European Photovoltaic Solar Energy Conference, pp. 153–164.

[67] M. Lipiński, "Silicon nitride for photovoltaic application," *Arch. Mater. Sci. Eng.*, vol. 46, no. 2, pp. 69–87, 2010.

[68] V. V. Iyengar, B. K. Nayak, and M. C. Gupta, "Optical properties of silicon light trapping structures for photovoltaics," *Sol. Energy Mater. Sol. Cells*, vol. 94, no. 12, pp. 2251–2257, 2010.

[69] Y. Han *et al.*, "Degradation observations of encapsulated planar $CH_3NH_3PbI_3$ perovskite solar cells at high temperatures and humidity," *J. Mater. Chem. A*, vol. 3, no. 15, pp. 8139–8147, 2015.

[70] I. Hwang, I. Jeong, J. Lee, M. Jae Ko, and K. Yong, "Enhancing Stability of Perovskite Solar Cells to Moisture by the Facile Hydrophobic Passivation," *ACS Appl. Mater. & Interfaces*, vol. 7, no. 31, pp. 17330–17336, Jul. 2015.

[71] K. H. Yoon, H. Kim, Y. E. Koo Lee, N. K. Shrestha, and M. M. Sung, "UV-enhanced atomic layer deposition of Al_2O_3 thin films at low temperature for gas-diffusion barriers," *RSC Adv.*, vol. 7, no. 10, pp. 5601–5609, 2017.

[72] H. Choi *et al.*, " Fast spatial atomic layer deposition of Al_2O_3 at low temperature (<100 °C) as a gas permeation barrier for flexible organic light-emitting diode displays ," *J. Vac. Sci. Technol. A Vacuum, Surfaces, Film.*, vol. 34, no. 1, p. 01A121, 2016.

[73] E. Y. Choi, J. Kim, S. Lim, E. Han, A. W. Y. Ho-Baillie, and N. Park, "Enhancing stability for organic-inorganic perovskite solar cells by atomic layer deposited Al_2O_3 encapsulation," *Sol. Energy Mater. Sol. Cells*, vol. 188, no. June, pp. 37–45, 2018.

[74] C. Y. Chang, K. T. Lee, W. K. Huang, H. Y. Siao, and Y. C. Chang, "High-Performance, Air-Stable, Low-Temperature Processed Semitransparent Perovskite Solar Cells Enabled by Atomic Layer Deposition," *Chem. Mater.*, vol. 27, no. 14, pp. 5122–5130, 2015.

[75] F. J. Ramos *et al.*, "Versatile perovskite solar cell encapsulation by low-temperature ALD-Al_2O_3 with long-term stability improvement," *Sustain. Energy Fuels*, vol. 2, no. 11, pp. 2468–2479, 2018.

[76] Y. Lv *et al.*, "Low-Temperature Atomic Layer Deposition of Metal Oxide Layers for Perovskite Solar Cells with High Efficiency and Stability under Harsh Environmental Conditions," *ACS Appl. Mater. Interfaces*, vol. 10, no. 28, pp. 23928–23937, 2018.

[77] H. Wang *et al.*, "Hermetic seal for perovskite solar cells: An improved plasma enhanced atomic layer deposition encapsulation," *Nano Energy*, vol. 69, no. November 2019, 2020.

[78] Q. Dong *et al.*, "Encapsulation of Perovskite Solar Cells for High Humidity Conditions," *ChemSusChem*, vol. 9, no. 18, pp. 2597–2603, 2016.

[79] K. A. Bush *et al.*, "23.6%-Efficient Monolithic Perovskite/Silicon Tandem Solar Cells With Improved Stability," *Nat. Energy*, vol. 2, no. 4, pp. 1–7, 2017.

[80] S. Guarnera *et al.*, "Improving the long-term stability of perovskite solar cells with a porous Al_2O_3 buffer layer," *J. Phys. Chem. Lett.*, vol. 6, no. 3, pp. 432–437, 2015.

[81] N. Rolston *et al.*, "Improved stability and efficiency of perovskite solar cells with submicron flexible barrier films deposited in air," *J. Mater. Chem. A*, vol. 5, no. 44, pp. 22975–22983, 2017.

[82] H. C. Weerasinghe, Y. Dkhissi, A. D. Scully, R. A. Caruso, and Y. B. Cheng, "Encapsulation for improving the lifetime of flexible perovskite solar cells," *Nano Energy*, vol. 18, pp. 118–125, 2015.

[83] K. J. Kanarik *et al.*, "Overview of atomic layer etching in the semiconductor industry," *J. Vac. Sci. Technol. A Vacuum, Surfaces, Film.*, vol. 33, no. 2, p. 020802, 2015.

[84] H. Kim, H. B. R. Lee, and W. J. Maeng, "Applications of atomic layer deposition to nanofabrication and emerging nanodevices," *Thin Solid Films*, vol. 517, no. 8, pp. 2563–2580,

2009.

[85] Q. Peng, X. Y. Sun, J. C. Spagnola, G. K. Hyde, R. J. Spontak, and G. N. Parsons, “Atomic layer deposition on electrospun polymer fibers as a direct route to Al_2O_3 microtubes with precise wall thickness control,” *Nano Lett.*, vol. 7, no. 3, pp. 719–722, 2007.

[86] Y. Yang *et al.*, “Research progress of atomic layer deposition technology to improve the long-term stability of perovskite solar cells,” *J. Mater. Chem. C*, vol. 10, no. 3, pp. 819–839, 2022.

[87] P. O. Oviroh, R. Akbarzadeh, D. Pan, R. A. M. Coetzee, and T.-C. Jen, “New development of atomic layer deposition: processes, methods and applications,” *Sci. Technol. Adv. Mater.*, vol. 20, no. 1, pp. 465–496, 2019.

[88] K. P. Musselman *et al.*, “Rapid open-air deposition of uniform, nanoscale, functional coatings on nanorod arrays,” *Nanoscale Horizons*, vol. 2, no. 2, pp. 110–117, 2017.

[89] D. H. Levy, S. F. Nelson, and D. Freeman, “Deposition,” vol. 5, no. 12, pp. 484–494, 2009.

[90] A. H. Alshehri *et al.*, “Quantum-Tunneling Metal-Insulator-Metal Diodes Made by Rapid Atmospheric Pressure Chemical Vapor Deposition,” *Adv. Funct. Mater.*, vol. 29, no. 7, 2019.

[91] S. Wack, P. Lunca Popa, N. Adjeroud, J. Guillot, B. R. Pistillo, and R. Leturcq, “Large-Scale Deposition and Growth Mechanism of Silver Nanoparticles by Plasma-Enhanced Atomic Layer Deposition,” *J. Phys. Chem. C*, vol. 123, no. 44, pp. 27196–27206, 2019.

[92] I. Nasution, A. Velasco, and H. joon Kim, “Atmospheric pressure chemical vapor deposition mechanism of Al_2O_3 film from $AlCl_3$ and O_2,” *J. Cryst. Growth*, vol. 311, no. 2, pp. 429–434, 2009.

[93] T. W.-K. Yeow, K. Mistry, A. Shahin, M. Yavuz, and K. P. Musselman, “Atmospheric-pressure spatial chemical vapor deposition of tungsten oxide,” *J. Vac. Sci. Technol. A*, vol. 38, no. 5, p. 052411, 2020.

[94] D. H. Levy, D. Freeman, and S. F. Nelson, “Oxide Electronics by Spatial Atomic Layer Deposition,” *J. Disp. Technol. Vol. 5, Issue 12, pp. 484-494*, vol. 5, no. 12, pp. 484–494, Dec. 2009.

[95] A. Illiberi, F. Roozeboom, and P. Poodt, “Spatial atomic layer deposition of zinc oxide thin films,” *ACS Appl. Mater. Interfaces*, vol. 4, no. 1, pp. 268–272, 2012.

[96] Y. Li *et al.*, “Enhanced Performance in Al-Doped ZnO Based Transparent Flexible Transparent Thin-Film Transistors Due to Oxygen Vacancy in ZnO Film with Zn-Al-O Interfaces Fabricated by Atomic Layer Deposition,” *ACS Appl. Mater. Interfaces*, vol. 9, no. 13, pp. 11711–11720, 2017.

[97] Z. Gao and P. Banerjee, “Review Article: Atomic layer deposition of doped ZnO films,” *J. Vac. Sci. Technol. A*, vol. 37, no. 5, p. 050802, 2019.

[98] E. Dickey, K. Niiranen, B. Danforth, and W. A. Barrow, “Macro-conformality of coatings

deposited using high-speed spatial plasma-enhanced atomic layer deposition," *Appl. Opt.*, vol. 59, no. 5, p. A16, 2020.

[99] W. Niu *et al.*, "Applications of atomic layer deposition in solar cells," *Nanotechnology*, vol. 26, no. 6, p. 64001, 2015.

[100] R. L. Z. Hoye, D. Muñoz-Rojas, K. P. Musselman, Y. Vaynzof, and J. L. MacManus-Driscoll, "Synthesis and Modeling of Uniform Complex Metal Oxides by Close-Proximity Atmospheric Pressure Chemical Vapor Deposition," *ACS Appl. Mater. Interfaces*, vol. 7, no. 20, pp. 10684–10694, 2015.

[101] J.-H. Woo *et al.*, "Amorphous Alumina Film Robust under Cyclic Deformation: a Highly Impermeable and a Highly Flexible Encapsulation Material," *ACS Appl. Mater. & Interfaces*, vol. 13, no. 39, pp. 46894–46901, Sep. 2021.

[102] P. Poodt, A. Lankhorst, F. Roozeboom, K. Spee, D. Maas, and A. Vermeer, "High-speed spatial atomic-layer deposition of aluminum oxide layers for solar cell passivation," *Adv. Mater.*, vol. 22, no. 32, pp. 3564–3567, 2010.

[103] S. D. Elliott, G. Scarel, C. Wiemer, M. Fanciulli, and G. Pavia, "Ozone-based atomic layer deposition of alumina from TMA: Growth, morphology, and reaction mechanism," *Chem. Mater.*, vol. 18, no. 16, pp. 3764–3773, 2006.

[104] W. J. Lee *et al.*, "Comparative study of the electrical characteristics of ALD-ZnO thin films using H_2O and H_2O_2 as the oxidants," *J. Am. Ceram. Soc.*, vol. 102, no. 10, pp. 5881–5889, 2019.

[105] S. U. Lee, H. Park, H. Shin, and N. G. Park, "Atomic layer deposition of SnO_2 using hydrogen peroxide improves the efficiency and stability of perovskite solar cells," *Nanoscale*, pp. 5044–5052, 2023.

[106] S. Seo, T. Nam, H. B. R. Lee, H. Kim, and B. Shong, "Molecular oxidation of surface $–CH_3$ during atomic layer deposition of Al_2O_3 with H_2O, H_2O_2 , and O_3 : A theoretical study," *Appl. Surf. Sci.*, vol. 457, no. June, pp. 376–380, 2018.

[107] P. S. Maydannik, A. Plyushch, M. Sillanpää, and D. C. Cameron, " Spatial atomic layer deposition: Performance of low temperature H_2O and O_3 oxidant chemistry for flexible electronics encapsulation ," *J. Vac. Sci. Technol. A Vacuum, Surfaces, Film.*, vol. 33, no. 3, p. 031603, 2015.

[108] S. Franke *et al.*, "Alumina films as gas barrier layers grown by spatial atomic layer deposition with trimethylaluminum and different oxygen sources," *J. Vac. Sci. Technol. A Vacuum, Surfaces, Film.*, vol. 35, no. 1, p. 01B117, 2017.

[109] M. Coll and M. Napari, "Atomic layer deposition of functional multicomponent oxides," *APL Mater.*, vol. 7, no. 11, 2019.

[110] A. J. M. Mackus, J. R. Schneider, C. Macisaac, J. G. Baker, and S. F. Bent, "Synthesis of Doped, Ternary, and Quaternary Materials by Atomic Layer Deposition: A Review," *Chem. Mater.*,

vol. 31, no. 4, pp. 1142–1183, 2019.

[111] W. Yang *et al.*, "Optical properties and bandgap evolution of ALD $HfSiO_x$ films," *Nanoscale Res. Lett.*, vol. 10, no. 1, 2015.

[112] A. Colon, L. Stan, R. Divan, and J. Shi, "Investigating compositional effects of atomic layer deposition ternary dielectric Ti-Al-O on metal-insulator-semiconductor heterojunction capacitor structure for gate insulation of InAlN/GaN and AlGaN/GaN," *J. Vac. Sci. Technol. B, Nanotechnol. Microelectron. Mater. Process. Meas. Phenom.*, vol. 34, no. 6, p. 06K901, 2016.

[113] J. Meyer *et al.*, "Al_2O_3/ZrO_2 Nanolaminates as ultrahigh gas-diffusion barriersa strategy for reliable encapsulation of organic electronics," *Adv. Mater.*, vol. 21, no. 18, pp. 1845–1849, 2009.

[114] J. W. Elam, Z. A. Sechrist, and S. M. George, "ZnO/Al_2O_3 nanolaminates fabricated by atomic layer deposition: Growth and surface roughness measurements," *Thin Solid Films*, vol. 414, no. 1, pp. 43–55, 2002.

[115] C. H. Hsu *et al.*, "High doping efficiency Al-doped ZnO films prepared by co-injection spatial atomic layer deposition," *J. Alloys Compd.*, vol. 884, 2021.

[116] A. Illiberi, R. Scherpenborg, Y. Wu, F. Roozeboom, and P. Poodt, "Spatial atmospheric atomic layer deposition of alxzn1-xo," *ACS Appl. Mater. Interfaces*, vol. 5, no. 24, pp. 13124–13128, 2013.

[117] M. Kao, "An Intelligent Neural Network Controlled Atmospheric Pressure Spatial Atomic Layer Deposition System for Tunable Metal Oxide Thin Films by," 2018.

[118] C. M. de la Huerta, V. H. Nguyen, J. M. Dedulle, D. Bellet, C. Jiménez, and D. Muñoz-Rojas, "Influence of the geometric parameters on the deposition mode in Spatial Atomic Layer Deposition: A novel approach to area-selective deposition," *Coatings*, vol. 9, no. 1, 2019.

[119] Q. Jiang *et al.*, "Surface passivation of perovskite film for efficient solar cells," *Nat. Photonics*, vol. 13, no. 7, pp. 460–466, 2019.

[120] X. Zhao, H.-S. Kim, J.-Y. Seo, and N.-G. Park, "Effect of Selective Contacts on the Thermal Stability of Perovskite Solar Cells," *ACS Appl. Mater. & Interfaces*, vol. 9, no. 8, pp. 7148–7153, Feb. 2017.

[121] R. Wang, M. Mujahid, Y. Duan, Z. K. Wang, J. Xue, and Y. Yang, "A Review of Perovskites Solar Cell Stability," *Adv. Funct. Mater.*, vol. 29, no. 47, pp. 1–25, 2019.

[122] J. A. Bertrand and S. M. George, "Evaluating Al_2O_3 gas diffusion barriers grown directly on Ca films using atomic layer deposition techniques," *J. Vac. Sci. Technol. A Vacuum, Surfaces, Film.*, vol. 31, no. 1, p. 01A122, Jan. 2013.

[123] M. O. Reese, A. A. Dameron, and M. D. Kempe, "Quantitative calcium resistivity based method for accurate and scalable water vapor transmission rate measurement," *Rev. Sci. Instrum.*, vol. 82, no. 8, 2011.

[124] G. Nisato *et al.*, "Experimental comparison of high-performance water vapor permeation measurement methods," *Org. Electron.*, vol. 15, no. 12, pp. 3746–3755, 2014.

[125] D. J. Higgs, M. J. Young, J. A. Bertrand, and S. M. George, "Oxidation kinetics of calcium films by water vapor and their effect on water vapor transmission rate measurements," *J. Phys. Chem. C*, vol. 118, no. 50, pp. 29322–29332, 2014.

[126] K. L. Jarvis *et al.*, "Comparing three techniques to determine the water vapour transmission rates of polymers and barrier films," *Surfaces and Interfaces*, vol. 9, no. April, pp. 182–188, 2017.

[127] S. Schubert, H. Klumbies, L. Müller-Meskamp, and K. Leo, "Electrical calcium test for moisture barrier evaluation for organic devices," *Rev. Sci. Instrum.*, vol. 82, no. 9, p. 094101, Sep. 2011.

[128] P. F. Carcia, R. S. McLean, M. D. Groner, A. A. Dameron, and S. M. George, "Gas diffusion ultrabarriers on polymer substrates using Al_2O_3 atomic layer deposition and SiN plasma-enhanced chemical vapor deposition," *J. Appl. Phys.*, vol. 106, no. 2, 2009.

[129] H. Klumbies, L. Müller-Meskamp, T. Mönch, S. Schubert, and K. Leo, "The influence of laterally inhomogeneous corrosion on electrical and optical calcium moisture barrier characterization," *Rev. Sci. Instrum.*, vol. 84, no. 2, 2013.

[130] R. S. Kumar, M. Auch, E. Ou, G. Ewald, and C. S. Jin, "Low moisture permeation measurement through polymer substrates for organic light emitting devices," *Thin Solid Films*, vol. 417, no. 1–2, pp. 120–126, 2002.

[131] M. D. Kempe, M. O. Reese, and A. A. Dameron, "Evaluation of the sensitivity limits of water vapor transmission rate measurements using electrical calcium test," *Rev. Sci. Instrum.*, vol. 84, no. 2, 2013.

[132] H. Klumbies *et al.*, "Thickness dependent barrier performance of permeation barriers made from atomic layer deposited alumina for organic devices," *Org. Electron.*, vol. 17, pp. 138–143, 2015.

[133] J. Lu, B. Liu, N. P. Guisinger, P. C. Stair, J. P. Greeley, and J. W. Elam, "First-Principles Predictions and in Situ Experimental Validation of Alumina Atomic Layer Deposition on Metal Surfaces," *Chem. Mater.*, vol. 26, no. 23, pp. 6752–6761, Nov. 2014.

[134] M. V. Khenkin *et al.*, "Consensus statement for stability assessment and reporting for perovskite photovoltaics based on ISOS procedures," *Nat. Energy*, vol. 5, no. 1, pp. 35–49, 2020.

[135] A. G. Erlat *et al.*, "Characterisation of aluminium oxynitride gas barrier films," *Thin Solid Films*, vol. 388, no. 1–2, pp. 78–86, 2001.

[136] A. I. Abdulagatov, R. R. Amashaev, K. N. Ashurbekova, K. N. Ashurbekova, M. K. Rabadanov, and I. M. Abdulagatov, "Atomic Layer Deposition of Aluminum Nitride and Oxynitride on Silicon Using Tris(dimethylamido)aluminum, Ammonia, and Water," *Russ. J. Gen. Chem.*, vol. 88, no. 8, pp. 1699–1706, 2018.

[137] W. Xiao and X. Jiang, "Optical and mechanical properties of nanocrystalline aluminum

oxynitride films prepared by electron cyclotron resonance plasma enhanced chemical vapor deposition," *J. Cryst. Growth*, vol. 264, no. 1–3, pp. 165–171, 2004.

[138] J. Borges *et al.*, "Influence of composition, bonding characteristics and microstructure on the electrochemical and optical stability of AlO_xN_y thin films," *Electrochim. Acta*, vol. 106, pp. 23–34, 2013.

[139] M. Kim, K. M. Kang, Y. Wang, and H. H. Park, "N-doped Al_2O_3 thin films deposited by atomic layer deposition," *Thin Solid Films*, vol. 660, no. December 2017, pp. 657–662, 2018.

[140] H. Zhu, M. H. A. Shiraz, L. Liu, Y. Zhang, and J. Liu, "Atomic layer deposited aluminum oxynitride coating for high-performance Si anode in lithium-ion batteries," *Appl. Surf. Sci.*, vol. 578, no. November 2021, 2022.

[141] P. K. Parashar, S. A. Kinnunen, T. Sajavaara, J. J. Toppari, and V. K. Komarala, "Thermal atomic layer deposition of AlO_xN_y thin films for surface passivation of nano-textured flexible silicon," *Sol. Energy Mater. Sol. Cells*, vol. 193, no. November 2018, pp. 231–236, 2019.

[142] A. H. Alshehri, A. Shahin, K. Mistry, K. H. Ibrahim, M. Yavuz, and K. P. Musselman, "Metal-Insulator-Insulator-Metal Diodes with Responsivities Greater Than 30 A W^{-1} Based on Nitrogen-Doped TiO_x and AlO_x Insulator Layers," *Adv. Electron. Mater.*, vol. 7, no. 11, pp. 1–15, 2021.

[143] D. Muñoz-Rojas, T. Maindron, A. Esteve, F. Piallat, J. C. S. Kools, and J. M. Decams, "Speeding up the unique assets of atomic layer deposition," *Mater. Today Chem.*, vol. 12, pp. 96–120, 2019.

[144] M. A. Mione, V. Vandalon, W. M. M. Kessels, and F. Roozeboom, " Temperature study of atmospheric-pressure plasma-enhanced spatial ALD of Al_2O_3 using infrared and optical emission spectroscopy ," *J. Vac. Sci. Technol. A*, vol. 40, no. 6, p. 062407, 2022.

[145] B. Díaz *et al.*, "Low-temperature atomic layer deposition of Al_2O_3 thin coatings for corrosion protection of steel: Surface and electrochemical analysis," *Corros. Sci.*, vol. 53, no. 6, pp. 2168–2175, 2011.

[146] R. Z. Waldman, D. J. Mandia, A. Yanguas-Gil, A. B. F. Martinson, J. W. Elam, and S. B. Darling, "The chemical physics of sequential infiltration synthesis - A thermodynamic and kinetic perspective," *J. Chem. Phys.*, vol. 151, no. 19, 2019.

[147] H. M. T. Nguyen, H. Y. Tang, W. F. Huang, and M. C. Lin, "Mechanisms for reactions of trimethylaluminum with molecular oxygen and water," *Comput. Theor. Chem.*, vol. 1035, pp. 39–43, 2014.

[148] K. Arts *et al.*, "Foundations of atomic-level plasma processing in nanoelectronics," *Plasma Sources Sci. Technol.*, vol. 31, no. 10, p. 103002, 2022.

[149] A. S. Yersak, Y. C. Lee, J. A. Spencer, and M. D. Groner, " Atmospheric pressure spatial atomic layer deposition web coating with in situ monitoring of film thickness ," *J. Vac. Sci. Technol. A Vacuum, Surfaces, Film.*, vol. 32, no. 1, p. 01A130, 2014.

[150] T. Hanada, M. Kobayashi, S. Tanabe, and N. Soga, “Preparation and physical properties of rf-sputtered amorphous films in the Al_2O_3-AlN system,” *J. Non. Cryst. Solids*, vol. 135, no. 2–3, pp. 227–235, 1991.

[151] D. M. Dieter Mergel and and M. J. Martin Jerman, “Density and refractive index of thin evaporated films,” *Chinese Opt. Lett.*, vol. 8, no. S1, pp. 67–72, 2010.

[152] A. Yanguas-Gil, K. E. Peterson, and J. W. Elam, “Controlled dopant distribution and higher doping efficiencies by surface-functionalized atomic layer deposition,” *Chem. Mater.*, vol. 23, no. 19, pp. 4295–4297, 2011.

[153] X. Ding, J. Yang, C. Qin, X. Yang, T. Ding, and J. Zhang, “Nitrogen-doped ZnO film fabricated via rapid low-temperature atomic layer deposition for high-performance ZnO-N transistors,” *IEEE Trans. Electron Devices*, vol. 65, no. 8, pp. 3283–3290, 2018.

[154] S. Castro-Hermosa, M. Top, J. Dagar, J. Fahlteich, and T. M. Brown, “Quantifying Performance of Permeation Barrier—Encapsulation Systems for Flexible and Glass-Based Electronics and Their Application to Perovskite Solar Cells,” *Adv. Electron. Mater.*, vol. 5, no. 10, pp. 1–11, 2019.

[155] A. S. da Silva Sobrinho, G. Czeremuszkin, M. Latrèche, and M. R. Wertheimer, “Defect-permeation correlation for ultrathin transparent barrier coatings on polymers,” *J. Vac. Sci. Technol. A Vacuum, Surfaces, Film.*, vol. 18, no. 1, pp. 149–157, 2000.

[156] A. S. da Silva Sobrinho, M. Latrèche, G. Czeremuszkin, J. E. Klemberg-Sapieha, and M. R. Wertheimer, “Transparent barrier coatings on polyethylene terephthalate by single- and dual-frequency plasma-enhanced chemical vapor deposition,” *J. Vac. Sci. Technol. A Vacuum, Surfaces, Film.*, vol. 16, no. 6, pp. 3190–3198, 1998.

[157] J. H. Choi *et al.*, “Evaluation of gas permeation barrier properties using electrical measurements of calcium degradation,” *Rev. Sci. Instrum.*, vol. 78, no. 6, p. 064701, Jun. 2007.

[158] P. F. Carcia, R. S. McLean, and M. H. Reilly, “Permeation measurements and modeling of highly defective Al_2O_3 thin films grown by atomic layer deposition on polymers,” *Appl. Phys. Lett.*, vol. 97, no. 22, pp. 1–4, 2010.

[159] A. G. Erlat, B. M. Henry, C. R. M. Grovenor, A. G. D. Briggs, R. J. Chater, and Y. Tsukahara, “Mechanism of water vapor transport through PET/AlO_xN_y gas barrier films,” *J. Phys. Chem. B*, vol. 108, no. 3, pp. 883–890, 2004.

[160] S. S. Mali and C. K. Hong, “P-i-n/n-i-p type planar hybrid structure of highly efficient perovskite solar cells towards improved air stability: Synthetic strategies and the role of p-type hole transport layer (HTL) and n-type electron transport layer (ETL) metal oxides,” *Nanoscale*, vol. 8, no. 20, pp. 10528–10540, 2016.

[161] Z. Hawash, L. K. Ono, S. R. Raga, M. V. Lee, and Y. Qi, “Air-Exposure Induced Dopant Redistribution and Energy Level Shifts in Spin-Coated Spiro-MeOTAD Films,” *Chem. Mater.*, vol. 27, no. 2, pp. 562–569, Jan. 2015.

[162] L. Xiang *et al.*, “Progress on the stability and encapsulation techniques of perovskite solar cells,” *Org. Electron.*, vol. 106, no. December 2021, 2022.

[163] J. M. Jensen, A. B. Oelkers, R. Toivola, D. C. Johnson, J. W. Elam, and S. M. George, “X-ray Reflectivity Characterization of ZnO/Al_2O_3 Multilayers Prepared by Atomic Layer Deposition,” *Chem. Mater.*, vol. 14, no. 5, pp. 2276–2282, Apr. 2002.

[164] Y. Wu *et al.*, “Dopant Distribution in Atomic Layer Deposited ZnO:Al Films Visualized by Transmission Electron Microscopy and Atom Probe Tomography,” *Chem. Mater.*, vol. 30, no. 4, pp. 1209–1217, Feb. 2018.

[165] D. W. Choi, S. J. Kim, J. H. Lee, K. B. Chung, and J. S. Park, “A study of thin film encapsulation on polymer substrate using low temperature hybrid ZnO/Al_2O_3 layers atomic layer deposition,” *Curr. Appl. Phys.*, vol. 12, no. SUPPL. 2, pp. S19–S23, 2012.

[166] J. S. Na, G. Scarel, and G. N. Parsons, “In situ analysis of dopant incorporation, activation, and film growth during thin film ZnO:Al Atomic layer deposition,” *J. Phys. Chem. C*, vol. 114, no. 1, pp. 383–388, 2010.

[167] Z. Xing *et al.*, “Atomic Layer Deposition of Metal Oxides in Perovskite Solar Cells : Present and Future,” vol. 2000588, pp. 1–9, 2020.

[168] H. H. Park, “Inorganic Materials by Atomic Layer Deposition for Perovskite Solar Cells,” 2021.

[169] K. O. Brinkmann, T. Gahlmann, and T. Riedl, “Atomic Layer Deposition of Functional Layers in Planar Perovskite Solar Cells,” vol. 1900332, 2020.

[170] J. W. Elam and S. M. George, “Growth of Zno/Al_2O_3 alloy films using atomic layer deposition techniques,” *Chem. Mater.*, vol. 15, no. 4, pp. 1020–1028, 2003.

[171] J. W. Elam and S. M. George, “Growth of ZnO/Al_2O_3 Alloy Films Using Atomic Layer Deposition Techniques,” *Chem. Mater.*, vol. 15, no. 4, pp. 1020–1028, Feb. 2003.

[172] C.-Y. Su, L.-C. Wang, W.-S. Liu, C.-C. Wang, and T.-P. Perng, “Photocatalysis and Hydrogen Evolution of Al- and Zn-Doped TiO_2 Nanotubes Fabricated by Atomic Layer Deposition,” *ACS Appl. Mater. & Interfaces*, vol. 10, no. 39, pp. 33287–33295, Sep. 2018.

[173] A. Abidli, S. Hamoudi, and K. Belkacemi, “Synthesis, characterization and insights into stable and well organized hexagonal mesoporous zinc-doped alumina as promising metathesis catalysts carrier,” *Dalt. Trans.*, vol. 44, no. 21, pp. 9823–9838, 2015.

[174] A. Joi *et al.*, “Editors’ Choice—Interface Engineering Strategy Utilizing Electrochemical ALD of Cu-Zn for Enabling Metallization of Sub-10 nm Semiconductor Device Nodes,” *ECS J. Solid State Sci. Technol.*, vol. 8, no. 9, pp. P516–P521, 2019.

[175] H. Serier, M. Gaudon, and M. Ménétrier, “Al-doped ZnO powdered materials: Al solubility limit and IR absorption properties,” *Solid State Sci.*, vol. 11, no. 7, pp. 1192–1197, 2009.

[176] M. Chen *et al.*, “X-ray photoelectron spectroscopy and auger electron spectroscopy studies of

Al-doped ZnO films," *Appl. Surf. Sci.*, vol. 158, no. 1, pp. 134–140, 2000.

[177] C. Tong, J. Yun, Y.-J. Chen, D. Ji, Q. Gan, and W. A. Anderson, "Thermally Diffused Al:ZnO Thin Films for Broadband Transparent Conductor," *ACS Appl. Mater. & Interfaces*, vol. 8, no. 6, pp. 3985–3991, Feb. 2016.

[178] R. G. Jordan, D. M. Zehner, N. M. Harrison, P. J. Durham, and W. M. Temmerman, "An XPS investigation of the electronic structure in AgZn," *Zeitschrift für Phys. B Condens. Matter*, vol. 75, no. 3, pp. 291–295, 1989.

[179] A. Philip, "Deposition and Characterization of Aluminum Oxide Thin Films Prepared by Atomic Layer Deposition," *31*, p. 202, 2012.

[180] B. R. Kumar and T. S. Rao, "Investigations on opto-electronical properties of DC reactive magnetron sputtered zinc aluminum oxide thin films annealed at different temperatures," *Appl. Surf. Sci.*, vol. 265, pp. 169–175, 2013.

[181] C. Zhai *et al.*, "Effects of Al Doping on the Properties of ZnO Thin Films Deposited by Atomic Layer Deposition," 2016.

[182] F. Khan *et al.*, "Correlation between reflectance and photoluminescent properties of al-rich ZnO nano-structures," *Met. Mater. Int.*, vol. 21, no. 3, pp. 561–568, 2015.

[183] K. Mistry *et al.*, "Highly Sensitive Self-Actuated Zinc Oxide Resonant Microcantilever Humidity Sensor," *Nano Lett.*, vol. 22, no. 8, pp. 3196–3203, Apr. 2022.

[184] P. Banerjee, W. J. Lee, K. R. Bae, S. B. Lee, and G. W. Rubloff, "Structural, electrical, and optical properties of atomic layer deposition Al-doped ZnO films," *J. Appl. Phys.*, vol. 108, no. 4, 2010.

[185] K. Wang *et al.*, "High-performance water vapor barriers via amorphous alumina-polycrystalline zinc oxide hybrids with a self-wrinkling morphology," *Surf. Coatings Technol.*, vol. 447, no. May, 2022.

[186] R. L. Puurunen, "Surface chemistry of atomic layer deposition: A case study for the trimethylaluminum/water process," *J. Appl. Phys.*, vol. 97, no. 12, 2005.

[187] C. Guerra-Nuñez, M. Döbeli, J. Michler, and I. Utke, "Reaction and Growth Mechanisms in Al_2O_3 deposited via Atomic Layer Deposition: Elucidating the Hydrogen Source," *Chem. Mater.*, vol. 29, no. 20, pp. 8690–8703, Oct. 2017.

[188] A. Seweryn, K. Lawniczak-Jablonska, P. Kuzmiuk, S. Gieraltowska, M. Godlewski, and R. Mroczynski, "Investigations of structural and electrical properties of ALD films formed with the ozone precursor," *Materials (Basel).*, vol. 14, no. 18, 2021.

[189] and Z. S. Spiegelman, Jeff, Dan Alvarez, Russell J. Holmes, Ed Heinlein, "Advantages of Hydrogen Peroxide as an Oxidant for Atomic Layer Deposition and Related Novel Delivery System," *MRS Online Proc. Libr.*, pp. 12–26, 2013.

[190] Y. Wang, K.-M. Kang, M. Kim, and H.-H. Park, " Oxygen vacancy-passivated ZnO thin film formed by atomic layer deposition using H_2O_2 ," *J. Vac. Sci. Technol. A Vacuum, Surfaces, Film.*, vol. 36, no. 3, p. 031504, 2018.

[191] S. K. Kim, S. W. Lee, C. S. Hwang, Y.-S. Min, J. Y. Won, and J. Jeong, "Low Temperature (<100°C) Deposition of Aluminum Oxide Thin Films by ALD with O_3 as Oxidant," *J. Electrochem. Soc.*, vol. 153, no. 5, p. F69, 2006.

[192] P. S. Maydannik, A. Plyushch, M. Sillanpää, and D. C. Cameron, " Spatial atomic layer deposition: Performance of low temperature H_2O and O_3 oxidant chemistry for flexible electronics encapsulation ," *J. Vac. Sci. Technol. A Vacuum, Surfaces, Film.*, vol. 33, no. 3, p. 031603, 2015.

[193] S. Franke *et al.*, "Alumina films as gas barrier layers grown by spatial atomic layer deposition with trimethylaluminum and different oxygen sources," *J. Vac. Sci. Technol. A Vacuum, Surfaces, Film.*, vol. 35, no. 1, p. 01B117, 2017.

[194] R. Edy, X. Huang, Y. Guo, J. Zhang, and J. Shi, "Influence of argon plasma on the deposition of Al_2O_3 film onto the pet surfaces by atomic layer deposition," *Nanoscale Res. Lett.*, vol. 8, no. 1, 2013.

[195] J. G. Lee, H. G. Kim, and S. S. Kim, "Enhancement of barrier properties of aluminum oxide layer by optimization of plasma-enhanced atomic layer deposition process," *Thin Solid Films*, vol. 534, pp. 515–519, 2013.

[196] A. Azcatl, Q. Wang, M. J. Kim, and R. M. Wallace, "Al_2O_3 on WSe_2 by ozone based atomic layer deposition: Nucleation and interface study," *APL Mater.*, vol. 5, no. 8, pp. 1–7, 2017.

[197] A. Guerrero *et al.*, "Interfacial Degradation of Planar Lead Halide Perovskite Solar Cells," *ACS Nano*, vol. 10, no. 1, pp. 218–224, Dec. 2015.

[198] L. Zuo *et al.*, "Polymer-modified halide perovskite films for efficient and stable planar heterojunction solar cells," *Sci. Adv.*, vol. 3, no. 8, pp. 1–12, 2017.

[199] C.-Y. Chang *et al.*, "Tuning Perovskite Morphology by Polymer Additive for High Efficiency Solar Cell," *ACS Appl. Mater. & Interfaces*, vol. 7, no. 8, pp. 4955–4961, Feb. 2015.

[200] S. W. Seo, E. Jung, H. Chae, and S. M. Cho, "Optimization of Al_2O_3/ZrO_2 nanolaminate structure for thin-film encapsulation of OLEDs," *Org. Electron.*, vol. 13, no. 11, pp. 2436–2441, 2012.

[201] R. Saraf, A. Mathur, and V. Maheshwari, "Polymer-Controlled Growth and Wrapping of Perovskite Single Crystals Leading to Better Device Stability and Performance," *ACS Appl. Mater. & Interfaces*, vol. 12, no. 22, pp. 25011–25019, May 2020.

[202] M. L. Grilli *et al.*, "A Comparative Study of the Mechanical and Tribological Properties of Thin Al_2O_3 Coatings Fabricated by Atomic Layer Deposition and Radio Frequency Sputtering," *Phys. Status Solidi Appl. Mater. Sci.*, vol. 219, no. 1, pp. 1–7, 2022.

[203] M. Knez, K. Nielsch, and L. Niinistö, “Synthesis and surface engineering of complex nanostructures by atomic layer deposition,” *Adv. Mater.*, vol. 19, no. 21, pp. 3425–3438, 2007.

[204] D. W. Choi, S. J. Kim, J. H. Lee, K. B. Chung, and J. S. Park, “A study of thin film encapsulation on polymer substrate using low temperature hybrid ZnO/Al_2O_3 layers atomic layer deposition,” *Curr. Appl. Phys.*, vol. 12, no. SUPPL. 2, pp. 19–23, 2012.

[205] S. J. Lloyd and J. M. Molina-Aldareguia, “Multilayered materials: A palette for the materials artist,” *Philos. Trans. R. Soc. A Math. Phys. Eng. Sci.*, vol. 361, no. 1813, pp. 2931–2949, 2003.

[206] G. Jáger, J. J. Tomán, L. Juhász, G. Vecsei, Z. Erdélyi, and C. Cserháti, “Nucleation and growth kinetics of $ZnAl_2O_4$ spinel in crystalline ZnO – amorphous Al_2O_3 bilayers prepared by atomic layer deposition,” *Scr. Mater.*, vol. 219, no. February, 2022.

[207] J. López *et al.*, “Refractive index and bandgap variation in Al_2O_3-ZnO ultrathin multilayers prepared by atomic layer deposition,” *J. Alloys Compd.*, vol. 691, pp. 308–315, 2017.

Appendix A- Supplementary material for chapter 3; WVTR and PSCs' J-V curve.

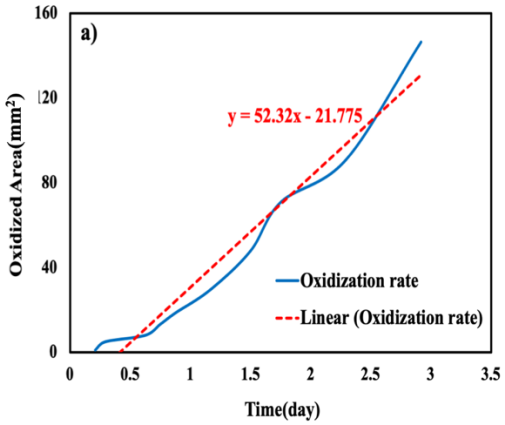

$$P = n\frac{M(H_2O)}{M(Ca)}\delta.h.\frac{\Delta A}{\Delta t}$$

$n = 2$

$\delta Ca = 1.55\ g{\cdot}cm^{-3} = 1.55\times10^{6}\ g.m^{-3}$

$M(H_2O) = 18\ g.mol^{-1}$

$M(Ca) = 40\ g.mol^{-1}$

$h = 200\ nm = 200\times10^{-9}\ m$

$\Delta A/\Delta t$ for 0.28N-Al_2O_3 TFE stored at ISOS-D-1= $0.52(mm^2/day)$

$WVTR = 1.4\times10^{-5}\ g/m^2/day$

Figure A-1. The oxidized surface area as a function of time for a Ca film with TFE stored at ISOS-D-1 condition. The slope of the plot corresponds to the oxidization rate of the Ca (ΔA/Δt) needed to calculate WVTR value. A sample WVTR calculation is also provided.

Example J-V curves of p-i-n and n-i-p PSCS under standard solar illumination are shown Figure A-2 and the performance parameters are summarized in Table . It is worth noting that the efficiency of n-i-p PSCs manufactured by our research group have recently been significantly improved; an efficiency of 21% has been achieved through the optimization of a new recipe.

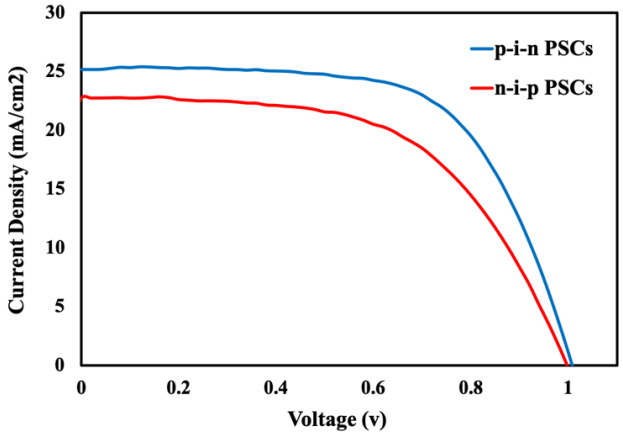

Figure A-2. J–V characteristics of n-i-p structure and p-i-n structure perovskite solar cells.

Table A-1. PCEs of p-i-n and n-i-p perovskite solar cells measured under the global AM1.5 spectrum (1000 W/m^2) in air.

Samples	J_{sc} (mA/cm^2)	V_{oc} (V)	FF	Efficiency (%)
p-i-n PSC	25.1	1.01	0.64	16.29
n-i-p PSC	22.7	0.99	0.58	12.96

Appendix B- Supplementary materials for chapter 4; N-AlO$_x$ TFE.

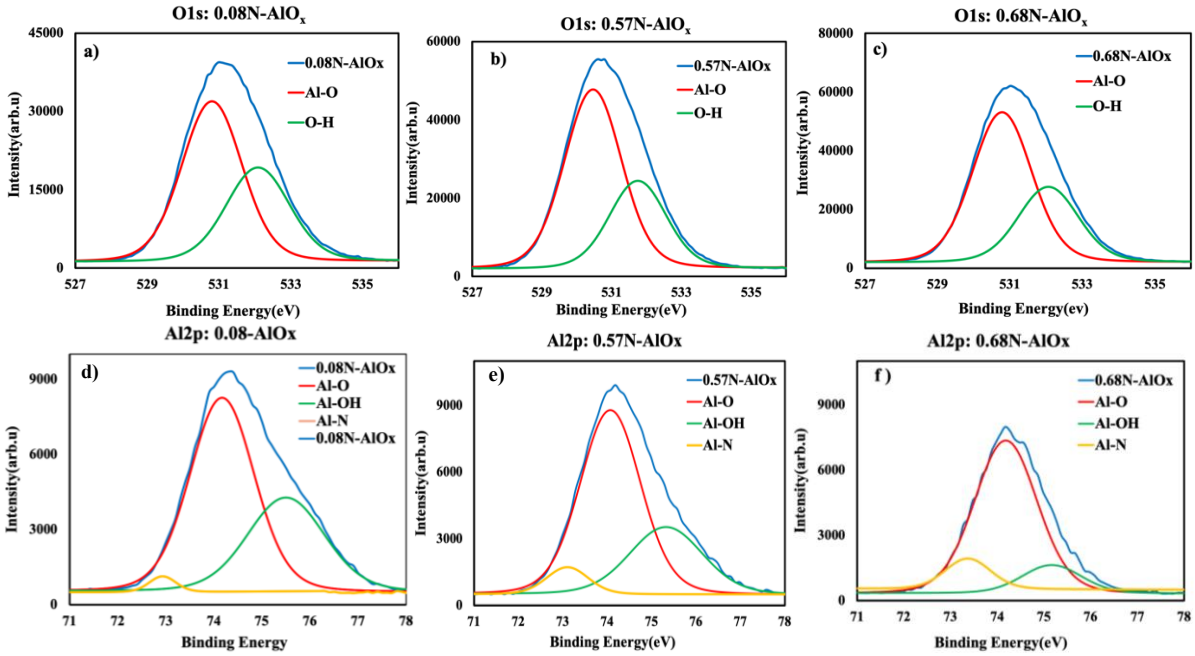

Figure B-1. O1s XPS spectra of a) 0.08N-AlO$_x$, b) 0.57N-AlO$_x$, and c) 0.68N-AlO$_x$ thin films. Al2p XPS spectra of d) 0.08N-AlO$_x$, e) 0.57N-AlO$_x$, and f) 0.68N-AlO$_x$ thin films.

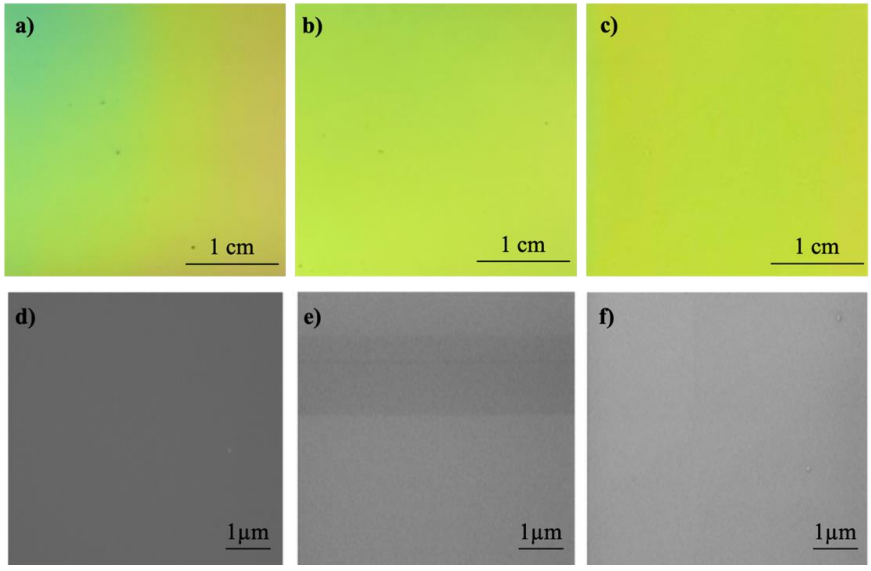

Figure B-2. Photographic images of a) 0.08N-AlO$_x$, b)0.57N-AlO$_x$, and c) 0.68N-AlO$_x$. SEM images of d) 0.08N-AlO$_x$, e) 0.57N-AlO$_x$, and f) 0.68N-AlO$_x$ films deposited using 120 oscillations.

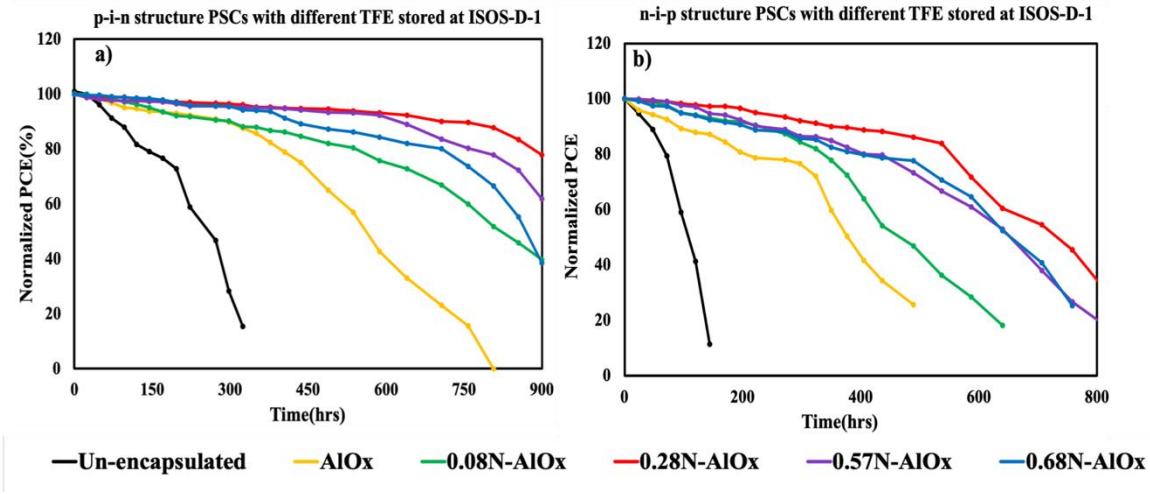

Figure B-3. Normalized PCE versus time for a) p-i-n structure and b) n-i-p structure perovskite solar cells encapsulated with different thin film encapsulation layers kept at ISOS-D-1 (25˚C-55%RH). The PCE values were normalized to their initial PCE value.

Appendix C: Supplementary materials for chapter 5; Zn-AlO_x TFE

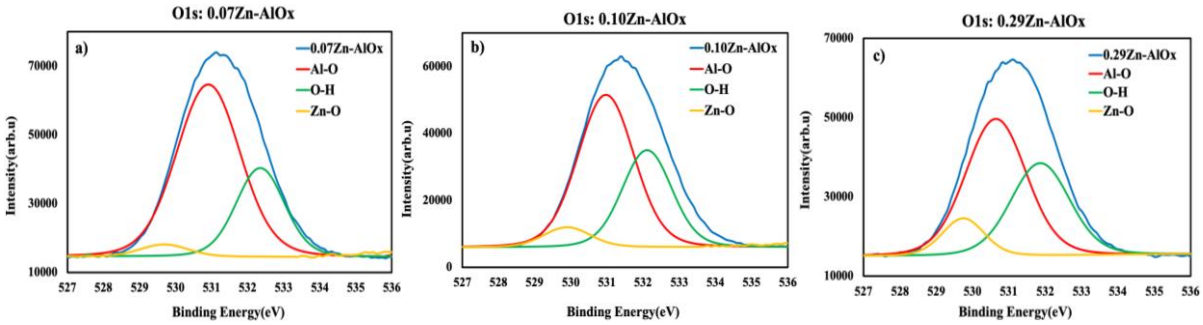

Figure C-1. O1s XPS spectra of a) 0.07Zn-AlO_x, b) 0.10Zn-AlO_x, and c) 0.29Zn-AlO_x thin films.

Appendix D- Supplementary material for chapter 7; PS-modified PSCs' characterizations.

It can be seen in Figure a that PS-modified devices achieve higher efficiency than plain (without the addition of PS) $MAPbI_3$ devices. The higher efficiency is mainly due to their higher J_{sc} and FF. To understand the role of PS in improving the device performance further characterization was done.

Figure b shows the XRD patterns of the PS-modified and plain $MAPbI_3$ devices. Peaks of the typical tetragonal phase are observed and there is no change in the crystalline phase of the perovskite film with the addition of PS. The PS-modified film shows slightly more intense and sharper peaks, indicating a higher film crystallinity and larger crystallite size. These results indicate that the addition of PS into the perovskite thin modulates the crystallization behavior and as a result, larger crystal grains are obtained[201][62]. To further confirm the improvement in grain size by the addition of PS, field emission SEM was done for both PS-modified and plain perovskite films. The SEM images of the plain (Figure c) and PS-modified perovskite (Figure d) show a multi-crystalline thin film with different grain sizes. The PS-modified films show a larger average grain size (~260 nm) compared to the plain films (~130 nm). The larger grains of PS-modified $MAPbI_3$ films lead to a decrease in structural defects and effective grain boundary area, which has been reported to result in suppressed charge recombination and hence improved performance[201][62].

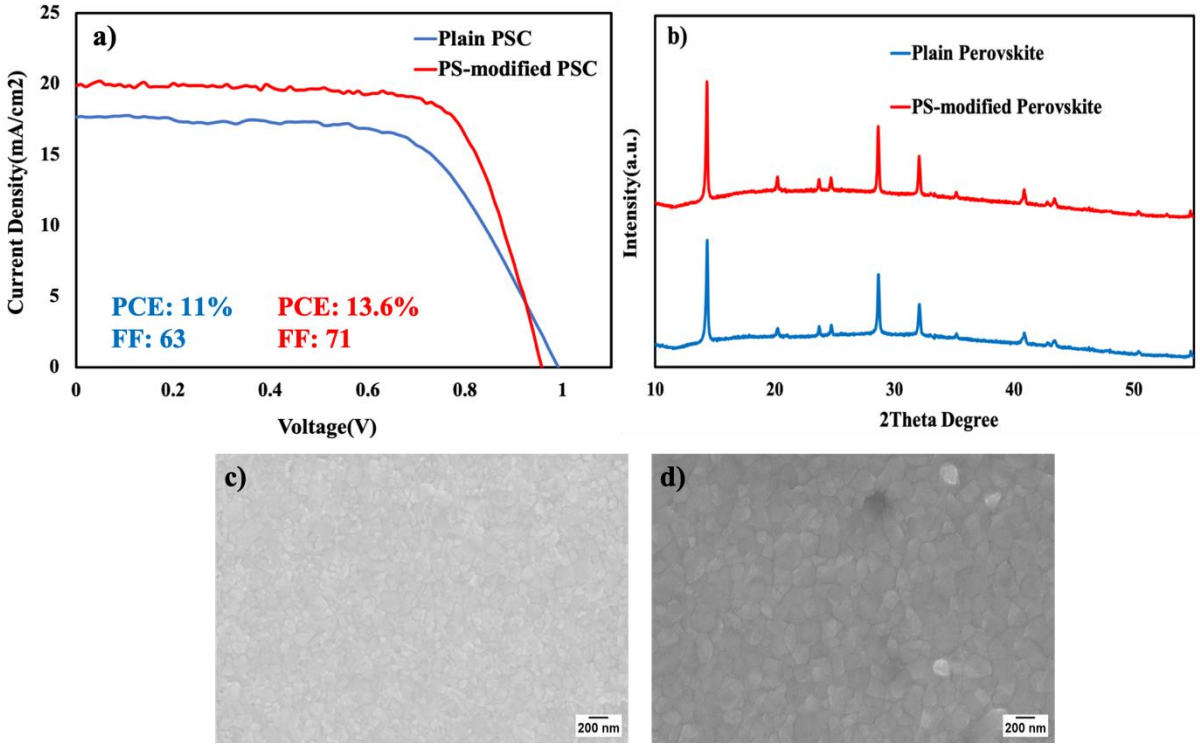

Figure D-1. a) J–V characteristics of plain and PS-modified perovskite solar cells, b) XRD pattern of PS-$MAPbI_3$ and plain $MAPbI_3$ devices, SEM images of c) plain $MAPbI_3$ and d) PS-$MAPbI_3$.